Spring 2-17-2014

Elucidation of Emergent Regional Mechanisms of Heart Muscle Dysfunction in the Mouse Model of Duchenne Muscular Dystrophy

Ya-Jian Cheng
Washington University in St. Louis

WASHINGTON UNIVERSITY IN ST. LOUIS

School of Engineering & Applied Science

Department of Biomedical Engineering

Dissertation Examination Committee:
Samuel Wickline, Chair
Igor Efimov
Paul Golumbek
Sándor Kovács
Larry Taber
Frank Yin
Jie Zheng

Elucidation of Emergent Regional Mechanisms of Heart Muscle Dysfunction in the Mouse Model of Duchenne Muscular Dystrophy

by

Ya-Jian Cheng

A dissertation presented to the
Graduate School of Arts and Sciences
of Washington University in
partial fulfillment of the
requirements for the degree
of Doctor of Philosophy

May 2014

Saint Louis, Missouri

Table of Contents

List of Figures

List of Tables

Acknowledgements

I send my most sincere thanks to Dr. Samuel A. Wickline and Dsc. Junjie Chen for their scientific guidance, constant inspiration and generous support in my doctoral research. I appreciate the opportunity to collaborate with Dr. Igor Efimov's and Dr. Lihong Wang's lab at Washington University for calcium transient imaging and photoacoustic imaging, respectively. I would like to acknowledge Dr. Gregory M. Lanza, Dr. Shelton Caruthers, for their valuable discussions and suggestions. I am very grateful to Mr. John S. Allen, Ms. Sharon Yang and Ms. Cordelia Caradine for their help in animal care and surgery. I thank Dr. Jon Marsh, Dr. Kirk Wallace, and Dr. Mike Hughes for their help on small animal ultrasound imaging. I would like to acknowledge Huiying Zhang and Noriko Yanaba for their dedicated help on histology. I thank all members of Cardiovascular MR Laboratories for their support and sharing the experiences in my doctoral research. Special thanks to Washington University staff members Karen Teasdale, Lillian Westfall and Jessica Runiewicz for the critical assistance on my payroll, graduation, and health insurance.

I thank lab staff members Sheila Crowder, Mike Scott, Grace Hu, and Frank Hockett for their help on reimbursement, purchase, chemistry, and instrumental electronics, respectively. I am very thankful to have a world-class, super-friendly and helpful Office of International Students and Scholars (OISS). The OISS staff cared and supported my life in the U.S. Without them, my graduate experience would not have be as safe, efficient and fun. The OISS definitely is critical to us international students. I met my host family, the Sue and Ron Williams family, through the OISS. Sue and Ron gave me warmth in the coldest and busiest years of my life. I know the future might be busier, but let's pretend the worst has passed. Thanks to my friends here who made my life in St. Louis less lonely: Jan, Jacob, Matt, Lance, Lei, the Dr. K., the renaissance man Wei-Hsiang Lin, the philanthropic Ching-yao Ko, and the lovely Jia Wei. I thank the American Heart Association for funding two years of my research. I specially thank the National Science Council and the Academia Sinica of Taiwan for their educational support for me since high school. Without Dr. Pung-Pung Hwang's guide and generous resources given since my high school

period, I could not have developed my scientific career as smoothly and fully. Lastly, thanks to my parents in Taiwan, who send me photos and paintings of their lively farm animals and warm regards toward my life here. I have had so much luck and too many people to thank. Let me thank God.

Ya-Jian Cheng

Washington University in St. Louis
January 2014

ABSTRACT OF THE DISSERTATION

Elucidation of Emergent Regional Mechanisms of Heart Muscle Dysfunction in the Mouse Model of Duchenne Muscular Dystrophy

By

Ya-Jian Cheng

Doctor of Philosophy in Biomedical Engineering

Washington University in St. Louis, 2014

Professor Samuel Wickline, Chair

Cardiac dysfunction is a primary cause of mortality in Duchenne Muscular Dystrophy (DMD), potentially related to elevated cytosolic calcium. However, the regional versus global functional consequences of cellular calcium mishandling have not been defined in the whole heart. Here, we elucidate, for the first time, loci- and age-dependencies between calcium mishandling and myocardial sheet function as a manifestation of dystrophin-deficient cardiomyopathy. We also map calcium transients to illustrate the regional dependence of ion flux disturbances in the dystrophin-deficient (*mdx*) mouse heart. Furthermore, we elucidate abnormalities in autophagic processes that can be corrected with nanoparticle therapeutics delivering rapamycin to heart tissues to improve ventricular function in affected older mice with incipient cardiomyopathy. We conclude that the rapid reversibility of functional defects by reducing cytosolic calcium or by impacting impaired autophagy points to the significance of regional mechanical factors in the progression of the disease.

Chapter 1: Introduction

1.1. Duchenne Muscular Dystrophy

1.1.1. The Gene

Duchenne muscular dystrophy (DMD) is a fatal X-linked genetic disease that affects 1:3500 of newborn boys who manifest unremitting deterioration of all muscle groups over time. The symptoms appear at the age of 2–6 years. By the age of 10, untreated patients are usually wheelchair-bound, and in their 20s they typically succumb (Fairclough, Wood *et al*. 2013).

The cause of DMD is the near or complete absence of dystrophin protein. The dytrophin gene is located on chromosome X and is 2.3 million base pair (bp) long (Altamirano, Lopez *et al*. 2012), occupying ~0.08% of the human genome of 2.9 billion bp (Alloatti, Gallo *et al*. 1995). It is the longest known human gene (Table 1). The 79 dystrophin exons are spliced into a 14 kbp mRNA[1], which requires 16 hours for processing in cultured myogenic cells (Altamirano, Lopez *et al*. 2012). Although gene therapy has been suggested as a possible cure for the disease, the large size of dystrophin gene exceeds the packaging capacity of currently available viral vectors. Although micro-dystrophin (~30% of original dystrophin cDNA sequence) and Dp71 isoform (~16% length or full dystrophin) were used to tackle the transfection capacity limitation, the effectiveness for this particularly large gene is yet not proven (Nicolas-Metral, Raddatz *et al*. 2001; Hecht, Adams *et al*. 2011; Spurney 2011). Moreover, immune reactions against the transfected gene challenge the clinical application of gene therapy (Berry, Andruszkiewicz et al. 2013).

[1] A gene contains exon(s) and usually intron(s). Exons are encoded into mRNA while introns are removed by RNA splicing.

	Histone H1a	Dystrophin	Titin
DNA length	781 bp	2 M bp	293 k bp[2]
mRNA length	781 bp	14 k bp	80 k bp[2]
Protein M.W.	22 k Da[3]	427 k Da[4]	3 M Da[5]

Table 1. Example of sizes of genes and proteins in the human genome. Histone H1a is small and contains no intron. In the human genome, dystrophin is the largest gene, most of which comprises introns. The titin gene produces the largest single protein in human genome.

Interestingly, both titin, the largest mammalian protein (Han, Grounds *et al*. 2006), and dystrophin, the longest gene in humans, exert a significant mechanical role in the heart. Titin is considered a mechanical spring responsible for diastolic recoil. The size might reflect the mechanical load it bears. Dystrophin is an adaptor between extracellular matrix and cytoskeleton. Its gene length reflects the fact that it produces many isoforms, which require alternative splicing and regulatory functioning of introns. When promoter defects or nonsense mutations, duplications, and deletions lead to *complete absence* of dystrophin, the resultant disease is DMD. When in-frame deletions or other mutations lead to *low expression or low function* of dystrophin protein, the resultant disease is Becker muscular dystrophy (BMD), a milder form of DMD (Bowles, McPhee *et al*. 2012). Figure 1 illustrates the spectrum of mutations and phenotypes for the dystrophin gene.

[2] Franco-Obregon, A. and J. B. Lansman (2002). "Changes in mechanosensitive channel gating following mechanical stimulation in skeletal muscle myotubes from the mdx mouse." The Journal of physiology **539**(Pt 2): 391-407.
[3] http://www.ncbi.nlm.nih.gov/protein/NP_005316.1
[4] Monaco, A.P., Neve, R.L., Colletti-Feener, C., Bertelson, C.J., Kurnit, D.M., and Kunkel, L.M. (1986). Isolation of candidate cDNAs for portions of the Duchenne muscular dystrophy gene. Nature 323:646-650. http://www.dmd.nl/isoforms.html
[5] "ProtParam for human titin". ExPASy Proteomics Server. Swiss Institute of Bioinformatics. http://web.expasy.org/cgi-bin/protparam/protparam1?Q8WZ42@1-34350@

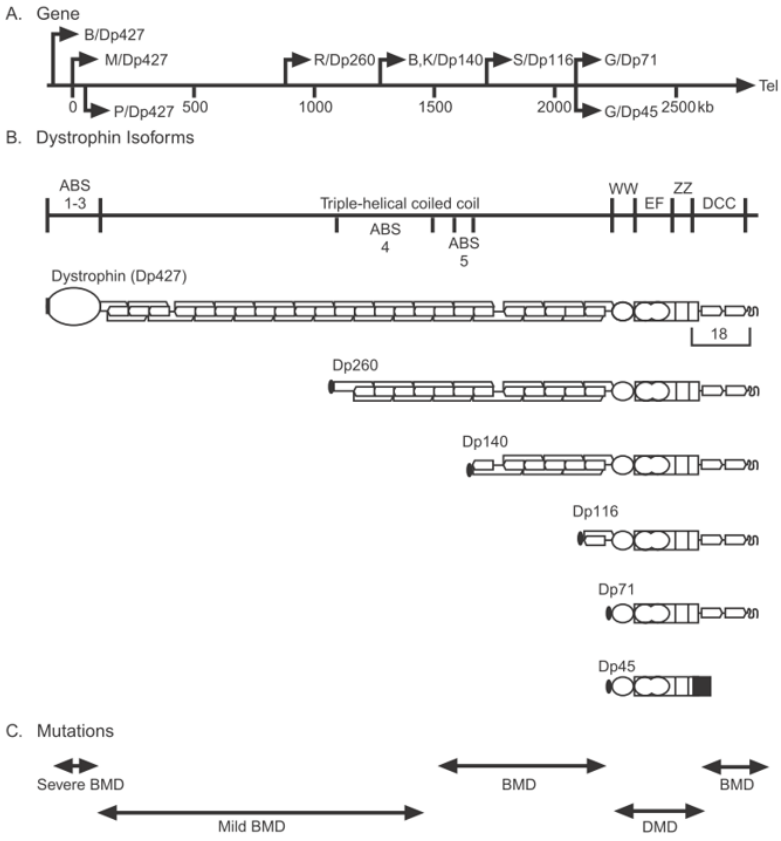

Figure 1. Schematic representation of dystrophin gene taken from He *et al* (He, Yi *et al*. 2013) (A), protein isoforms (B), dystrophin mutational spectrum (C). (A) The dystrophin gene is depicted as a 2500 kb arrow pointing from the centromere to the telomere, promoters are shown as right-angled arrows coming off the main arrow with a letter depicting promoter name and dystrophin protein (Dp) in kDa as a number. B, brain promoter (Nudel*et al*., 1989); M, muscle promoter (Klamut *et al*., 1990); P, purkinje promoter (Gorecki *et al*., 1992); R, retina promoter (D'Souza *et al*., 1995); B=K, brain and kidney (Lidov *et al*., 1995); S, Schwann cell (Byers *et al*., 1993); G, general giving rise to both Dp71 (Bar *et al*., 1990) and Dp45 (Tinsley *et al*., 1993). (B) Key followed by schematic representations of the various translated products from the dystrophin gene. Key: ABS, actin-binding sites 1±3, 4 and 5, WW, WW domain; EF, EF hand calcium-binding domain; ZZ, ZZ zinc finger domain; DCC, predicted dimeric coiled coil. Protein schematics are shown aligned under the key with different shaped regions depicting the different domains. Alternatively spliced exons are shown in black and as a square-bracketed 18 below the C terminus of full-length dystrophin, indicating the 18 alternative splice variants in this region (see Fabbrizio *et al*., 1994, for review).

1.1.2. The Protein

Dystrophin is expressed in muscle, kidney, brain and other human tissues (Chelly, Kaplan et al. 1988). In muscle, the dystrophin protein is a physical adapter between extracellular matrix (ECM) and intracellular cytoskeleton (Figure 2). Based on stoichiometry, Ghate et al have shown that one dystrophin binds directly to 24 actin monomers (Ghate, Baker *et al*. 2011). Dystrophin binds to ECM indirectly through dystroglycans and sarcroglycans. Mutations on

dystroglycans and sarcroglycans both lead to distinct forms of muscular dystrophies (Medvedev, Murro *et al*. 2011). Baron et al have shown that the sarcolemma of the dystrophin-deficient (*mdx*) mouse muscles is four time less stiff than that of control mice (Baron, Hecht *et al*. 2011), indicating a mechanical role for dystrophin.

The absence of dystrophin results in alteration in membrane structure, which is related to the dystrophin-associated proteins. The dystrophin-associated protein complex is part of a riblike lattice structure called the costamere.(Olamaei, Cheriet *et al*. 2010). These anchor the cytoskeleton to the ECM (Rybakova, Patel *et al*. 2000), and distribute contractile forces generated in the muscle fiber laterally through the sarcolemma to the basal lamina in ECM and thereby maintain uniform sarcomere length along the fiber (Danowski, Imanaka-Yoshida *et al*. 1992). Absence of dystrophin protein leads to complete loss of the dystrophin-associated protein complex and disruption of costamere lattice, resulting in excessive membrane fragility (Rybakova, Patel *et al*. 2000). In addition to these mechanical functions, signaling functions of dystrophin have been theorized as discussed in Chapter 4.

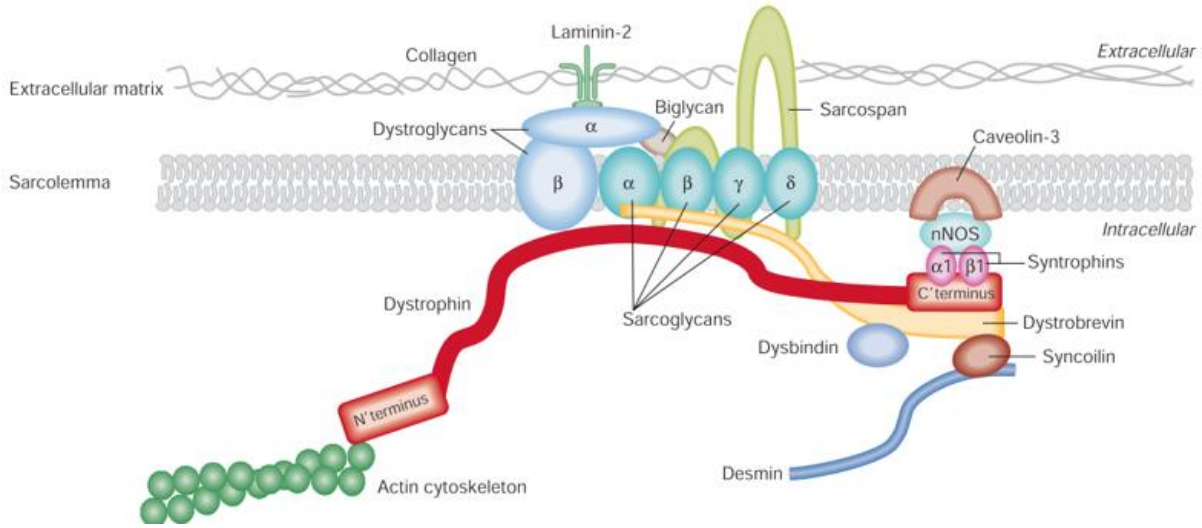

Figure 2. The dystrophin protein in muscle linking the internal cytoskeleton to the extracellular matrix. From (Morelli, Runge *et al*. 2011)

1.1.3. The Disease Phenotype

DMD patients manifest skeletal muscle weakness and fat/fibrosis infiltration in their first decade and succumb to *respiratory* or *cardiac failure* before the third decade (He, Yi *et al*. 2013). DMD skeletal muscle biopsy characteristically reveals necrotic and degenerating muscle fibers, surrounded by macrophages and CD4+ lymphocytes. Smaller immature centrally nucleated fibers reflect ongoing muscle cell regeneration (Deconinck and Dan 2007). Raised levels of muscle enzymes (CK) in DMD patients offer evidence of sarcolemma fragility that occurs after exercise (Stepkowski 2003; O'Brien, Stinson et al. 2008). Subsequent skeletal muscle necrosis and fibrosis result in loss of contractility, eventually in respiratory failure, and ultimately death from muscle weakness. Monitoring of the disease progression with MRI (Magnetic Resonance Imaging) can define regional heterogeneity among various muscle groups, and assess treatment efficacy for limiting fatty infiltration and fibrosis (Kim, Laor *et al*. 2010; Kim, Laor *et al*. 2010).

Histological analysis of DMD hearts demonstrates replacement of myocardium by connective tissue or fat (Schmidt, Burmeister *et al*. 2003). Fibrosis and diastolic dysfunction precede overt dilated cardiomyopathy (DCM), which is subsequently complicated by heart failure and arrhythmia (Judge, Kass *et al*. 2011). In DMD patients, the basal posterior-lateral wall is mostly affected by fibrosis, sparing the apex, RV, and atrium. However, even under these circumstances, heart failure may be induced by stress testing in the face of normal cardiac function at rest (Sethna, Rockoff *et al*. 1988; Schmidt, Burmeister *et al*. 2003).

Cardiac dysfunction accounts for 10~20% mortality in DMD, making it the second leading cause of patient death after respiratory failure (Gulati, Saxena *et al*. 2005). Cardiac dysfunction develops later than does respiratory dysfunction, but advances in respiratory support and patient care have allowed patients to survive into their late 20s and 30s or ordler. (Ishikawa, Bach *et al*. 1999; Ahuja, Kalra *et al*. 2000; Wagner, Lechtzin *et al*. 2007) Accordingly, cardiac complications now are commanding closer scrutiny in the management of advanced disease in DMD patients (Finsterer and Stollberger 2007; McNally 2008; Hermans, Pinto *et al*. 2010; Romfh and McNally 2010).

The early manifestations and functional consequences of DMD cardiomyopathy have been summarized recently by Judge *et al* in (Judge, Kass *et al*. 2011):

> The cardiomyopathy that develops in DMD is characterized by normal or thinned left ventricular (LV) wall thickness and progressive decline in ejection fraction or fractional shortening. Variable degrees of LV dilation occur. Abnormal LV *relaxation*[6] has also been identified as an early manifestation in DMD.

[6] This abnormal relaxation presages the experimental results in section 2.5 showing that cardiac sheet function is normal in systole but abnormal in diastole.

Notably in DMD, cardiac diastolic dysfunction precedes systolic dysfunction, as observed by Doppler ultrasound (Markham, Michelfelder *et al*. 2006) and tissue Doppler ultrasound (Bahler, Mohyuddin *et al*. 2005). DMD cardiomyopathy also exhibits regional abnormalities: MRI scar imaging detects early onset of fibrosis at the epicardium of the more basal segments (Toyota, Fujimoto *et al*. 2002; Yilmaz, Gdynia *et al*. 2010). MRI tagging methods have revealed abnormal strain at the base but not the apex in patients with normal ventricular function (Ashford, Liu *et al*. 2005) as a manifestation of occult cardiac dysfunction. Mertens *et al*. reported significantly decreased early diastolic myocardial velocities in the anterolateral and inferolateral left ventricular walls with normal global systolic function (Mertens, Ganame *et al*. 2008). The previous work by Dr. Wickline's group using MR tagging uncovered occult abnormal wall strains occurring regionally at the base of heart in DMD patients (Ashford, Liu *et al*. 2005) has been supported by subsequent reports by Li *et al* suggesting that cardiac mechanical strain abnormalities are more prominent in the basal segments of hearts in *mdx* mice (Li, Liu *et al*. 2009). These studies indicate that *regional* myocardial dysfunction precedes global systolic dysfunction and validates the importance of advanced imaging techniques as tools for early delineation of DMD cardiomyopathy.

The observed *regional* dependencies for DMD cardiac mechanical dysfunction remain to be explained, as the mutation is present in *all* cardiomyocytes (Bulfield, Siller *et al*. 1984; van Deutekom, Bremmer-Bout *et al*. 2001; Banks and Chamberlain 2008).

1.1.4. Treatment Options

Unfortunately, there is no effective curative treatment, but palliative therapy has advanced in clinical trials over the last 20 years. To date, the only active pharmacologic interventions proven beneficial for the altering the natural history of the underlying dystrophic process have been the corticosteroids: prednisone and deflazacort (Rinaldi, Mayer *et al*. 2013). Both medications have been shown in clinical trials to lead to modest improvements in muscle strength and function, although the duration of these benefits typically lasts less than 2 years and the mechanism remains undefined (Araujo, Bonuccelli et al. 2013; Hollinger, Gardan-Salmon et al. 2013). Importantly, azathioprine (an immunosuppressant) and prednisone both decrease DMD muscle inflammatory infiltrates equally, but only prednisone improves strength (Griggs, Moxley *et al*. 1991; Kissel, Lynn *et al*. 1993). Animal studies have shown that prednisone enhances strength in dystrophin deficient transgenic mice that lack T-cells and B-cells, indicating prednisone's therapeutic effect does not operate through T-cell/B-cell immune suppressive pathways (Golumbek, Keeling *et al*. 2007).

β-adrenergic receptor blockers, angiotensin-converting enzyme inhibitors (ACEi) and angiotensin II-type 1 receptor blockers (ARBs) are also used for treating DMD cardiomyopathy (Duboc, Meune *et al*. 2007; Ogata, Ishikawa *et al*. 2009; Fayssoil, Nardi *et al*. 2010). Our group has demonstrated a beneficial effect of ACEi on reducing fibrosis and calcium content in Syrian hamster with cardiomyopathy, which harbors a related sarcoglycan deficiency. Although the precise mechanism is unclear, a 10 year long clinical study showed that ACEi reduces DMD mortality (Duboc, Meune *et al*. 2007). A large body of work on ACEi for scar tissue reduction has demonstrated utility for inhibiting focal and global cardiac remodeling after myocardial infarction by interrupting angiotensin signaling in the heart (Iwata, Cowling et al. 2011).

1.1.5. The *mdx* mouse model

Animal models are valuable tools for studying the pathogenesis of disease and for pre-clinical trials. The *mdx* mouse is the most widely utilized animal model for DMD (Williams and Allen 2007; Banks and Chamberlain 2008). It carries a point mutation leading to complete absence of dystrophin in myocytes. Similar to the later onset of cardiomyopathy in human patients, young *mdx* mice (< 3 months old) develop only a mild phenotype of cardiac disease and exhibit normal resting $[Ca^{2+}]_I$ (Williams and Allen 2007; Van Erp, Loch *et al*. 2010). However, both dilated cardiomyopathy and elevated resting $[Ca^{2+}]_i$ begin to be observed by about 10 months of age (Quinlan, Hahn *et al*. 2004; Williams and Allen 2007). Since *mdx* mice share the same genetic defect as DMD patients, they represent a standard model for assessing cardiac dysfunction and therapeutics.

1.1.6. Calcium Overload Hypothesis

With respect to pathophysiological features of dystrophin deficiency potentially responsible for mechanical dysfunction, several recent studies in isolated cardiomyocytes of *mdx* mouse have suggested that intracellular calcium ($[Ca^{2+}]$i) mishandling is a key causative factor (Williams and Allen 2007; Fanchaouy, Polakova *et al*. 2009; Allen, Gervasio *et al*. 2010). Data acquired from *mdx* mice showed elevated resting $[Ca^{2+}]$i in dystrophin-deficient cardiomyocyte (Pressmar, Brinkmeier *et al*. 1994; Williams and Allen 2007). The calcium overload activates calpains to promote proteolysis leading to cardiomyocyte degeneration (Spencer, Croall *et al*. 1995; Spencer and Tidball 1996; Gailly, De Backer *et al*. 2007). The calcium mishandling might

also affect the cardiac contraction that is controlled by calcium induced calcium release (Bellinger, Reiken *et al*. 2009).

Specifically, (Sapp, Bobet *et al*. 1996) reported that under 1 Hz pulse stimulation, peak force and time-to-peak force were similar in both *mdx* and wildtype cardiac fibers, but half-relaxation time was significantly prolonged in *mdx*, indicating normal contraction but abnormal relaxation. However, (Alloatti, Gallo *et al*. 1995; Janssen, Hiranandani *et al*. 2005) both reported depressed contractile force in *mdx* cardiac fiber, as compared to wildtype. This reported disparity in normal versus abnormal contractile force might be a consequence of a higher stimulation frequency used by Alloatti (4 Hz) and Janssen (2.8Hz). Nicolas et al reported abnormally prolonged relaxation in *mdx* skeletal muscles, while the active contraction metrics were normal (Nicolas-Metral, Raddatz *et al*. 2001), suggesting a decreased capacity for calcium removal in *mdx* cells leading to alterations of muscle relaxation that accords with the observation that diastolic dysfunction precedes systolic dysfunction in DMD patients and *mdx* mice (section 1.1.3).

Several mechanisms for elevated resting $[Ca^{2+}]i$ have been proposed, offering opportunities for developing new therapies. One promising therapeutic approach is to inhibit the calcium influx that occurs through SAC (stretch activated channels) or through transient microruptures of the sarcolemma. It is well recognized that *mdx* cardiomyocytes are sensitive to stretch induced injury that is correlated with increased resting $[Ca^{2+}]i$ (Lynch 2004; Yeung and Allen 2004). Inhibition of SAC or the application of the membrane sealant poloxamer 188 reduces resting $[Ca^{2+}]i$ and prevents injury (Yasuda, Townsend *et al*. 2005; Whitehead, Streamer *et al*. 2006; Ward, Williams *et al*. 2008). In vivo application of poloxamer 188 also protects *mdx* mice from heart failure during dobutamine mediated cardiac challenge (Yasuda, Townsend *et al*.

2005). Inhibiting the leakage of ryanodine receptor (RyR2), a calcium release channel located on the sarcoplasmic reticulum, is another emerging therapeutic approach (Bellinger, Reiken *et al*. 2008; Shannon 2009). Notably, the RyR2 of *mdx* cardiomyocytes appears to be hypernitrosylated, which prevents RyR2 from fully close at resting state (Bellinger, Reiken *et al*. 2009). The resulting sarcoplasmic reticulum calcium leakage through RyR2 is indicated by the presence of calcium sparks (Ward, Schneider *et al*. 2000). Several 1-4-benzothiazepine derivatives, such as S107 and KD201, can stabilize RyR2 to reduce calcium leakage and improve cardiac function (Wehrens, Lehnart *et al*. 2004; Lehnart, Terrenoire *et al*. 2006).

Besides pharmaceutical approaches, transgenic approaches provide potential remediation of calcium mishandling. The root cause of DMD is the lack of dystrophin, making transgene therapy for correction of the dystrophin gene preferable to altering calcium handling genes. However, clinical studies suggest that immunity to transgenic micro-dystrophin in DMD patients represents a significant challenge, because patients that are dystrophin-null recognize transgenic micro-dystrophin as an exogenous antigen (Mendell, Campbell *et al*. 2010). Therefore, transgenic strategies based on endogenous genes, such as sarco/endoplasmic reticulum Ca^{2+}-ATPase (SERCA), may offer an immune advantage as compared to dystrophin gene therapies. Indeed, cardiac SERCA2a gene transfection has been shown to correct ECG abnormalities in heart (Shin, Bostick *et al*. 2011); and skeletal SERCA1 gene transfection corrected skeletal muscle calcium reuptake in dystrophic mice (Goonasekera, Lam *et al*. 2011).

The previously reported lack of efficacy of L-type calcium channel blockers against DMD associated muscular dystrophy should not negate the potential value of calcium channel targeted therapy (Phillips and Quinlivan 2008). L-type calcium channels regulate calcium inflow upon depolarization and are closed in the resting state. Since calcium leakage through these

channels has not been reported, L-type calcium channels' effect on regulating resting $[Ca^{2+}]i$ should not be expected to be significant.

In summary, calcium targeted therapy holds potential for treating DMD. Because calcium influx cannot be measured in vivo in heart tissue, we propose that development of a surrogate cardiac phenotype that reflected $[Ca^{2+}]i$ would be useful for evaluating the efficacy of treatment. We have previously shown that left ventricular myocardial architecture changes dynamically in cardiac cycle due to calcium regulated contraction-relaxation (Chen, Liu *et al*. 2005).

1.1.7. Hypothesis

How calcium mishandling influences cardiac mechanical dysfunction in whole heart preparations has not been clarified, especially taking into account cellular and mechanical events that are spatio-temporally distributed and regionally heterogeneous (DeAnda, Komeda *et al*. 1998; Balzer, Furber *et al*. 1999). Given the recognized abnormal and regionally heterogeneous wall strains (Figure 3) and fibrosis (Ashford, Liu *et al*. 2005; Yilmaz, Gdynia *et al*. 2008; Yilmaz, Gdynia *et al*. 2010) in DMD hearts of both human patients and *mdx* mice, we hypothesize that the sheet functional consequences of dystrophin deficiency plays out *regionally* in *DMD* hearts over time despite the ubiquitous lack of dystrophin protein in all cardiomyocytes. We hypothesize that elevated resting $[Ca^{2+}]i$ directly affects myofiber and sheet kinetics in *mdx* mouse hearts which can be quantified by diffusion tensor MRI (DTI, Chapter 2).

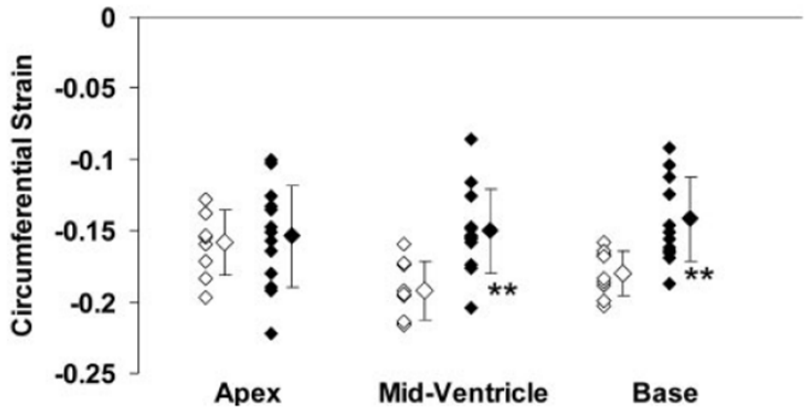

Figure 3. Cardiac MRI detected abnormal strain at base but not apex of DMD patient hearts, indicating base exhibits more myocardial dysfunction than apex. Figure from (Ashford, Liu *et al*. 2005)

The heart comprises a syncytium of cardiomyocytes that are organized in unique 3D fiber-sheet architecture that is critical for optimizing a coordinated sequence of excitation, contraction, and relaxation (Streeter and Hanna 1973; Costa, Takayama *et al*. 1999). Many reports have shown that sheet function produces a sliding motion that is accompanied by dynamic reorientation in systole, contributing to approximately 50% of focal wall thickening (LeGrice, Smaill *et al*. 1995; LeGrice, Takayama *et al*. 1995; Costa, Takayama *et al*. 1999; Dou, Tseng *et al*. 2003; Chen, Liu *et al*. 2005). Significant sheet-fiber deformation was also found in early diastole (Ashikaga, Criscione *et al*. 2004). Because one role of dystrophin is to anchor cardiomyocytes to the extracellular matrix to coordinate contraction-relaxation coupling, we propose that dystrophin deficiency could adversely affect sheet function. Given that ventricular wall strain vary regionally from base to apex, and in light of the expected vulnerability of dystrophin deficient cardiomyocytes to stretch-induced membrane injury, we sought to examine the role of sheet function in the regional mechanical defects reported in the DMD cardiomyopathy (Ashford, Liu *et al*. 2005; Li, Liu *et al*. 2009). We investigated the heart sheet structure defect in regions of heart with ultra high-field MRI, because MRI is non-destructive and provides functional assessment according to the methodology described in Chapter 2.

Examination of this regional structural functionality may add to the fundamental understanding of the nature of the heart dysfunction in DMD and lead to improved early monitoring of interventions designed to salvage cardiac structure and function.

Chapter 2: MRI for Cardiac Sheet Function

2.1. Cardiac muscle structure

The normal architecture of the heart muscle remains elusive despite recent advance in high resolution images offered by MRI and photoacoustic imaging (Gilbert, Benson *et al*. 2007). Several models have been proposed to explain cardiac structure without reaching a consensus. Therefore, accurate knowledge about the architecture of heart muscles is critical in understanding normal heart and cardiomyopathy. A comprehensive understanding of myocardial architecture would help us to (1.) explain cardiac electric and mechanical mechanics; (2.) simulate cardiac physiology; (3.) design intervention/monitoring strategy; and (4) understand structure-function relationship of the heart. In the future, we could compare myocardial architecture among fish, amphibian, reptile, bird, and mammal, to understand the evolution of the heart, in which lies the natural history of how the heart adapts the gravity and land environments with high pressurizing ability. A comprehensive review of cardiac architecture during 17^{th} century and year 2002 can be found in a MIT doctorate dissertation (Dou 2002). Below is my review of recent update.

2.1.1. Fiber

Myocardial fibers are cardiac muscle cells, which include sarcolemma and bundles of parallel or sometimes branching myofibrils. *Cell and fiber are terms that may be used interchangeably* (Pollack 1990). The 3D myocardial architecture is critical for optimizing a

coordinated sequence of excitation, contraction, and relaxation (Streeter and Hanna 1973; Costa, Takayama *et al*. 1999). The earliest study of fiber helical path was a reprint in Latin by Stensen in 1664. An English review can be found in (Dou 2002).

Based on laborious histology work, Streeter reported a smooth transition of fiber helix angle (α, angle between fibers and local circumferential axis) in the transmural direction (Figure 4) Streeter proposed a wicker basket model to explain how α might reflect the ventricular volume (Figure 4 B). However, the basket model represents the LV incorrectly, because recent studies have found that helix angle *decreases* during longitudinal extension (i.e., diastole) (Chen, Liu *et al*. 2005). In contrast, the wicker basket model predicts *increased* α during longitudinal extension (Figure 4 B). Nevertheless, a smooth transmural transition of α is observed in many mammalian species (Scollan, Holmes *et al*. 1998; Tseng, Wedeen *et al*. 2003; Chen, Liu *et al*. 2005; Helm, Beg *et al*. 2005). Chen 2005 found that Δα is decreased by ~7 degree in diastole compared to systole. This small change was not detected by Streeter with his histology method (Streeter and Hanna 1973), probably due to the unavoidable dehydration/deformation artifacts of histology specimen preparation.

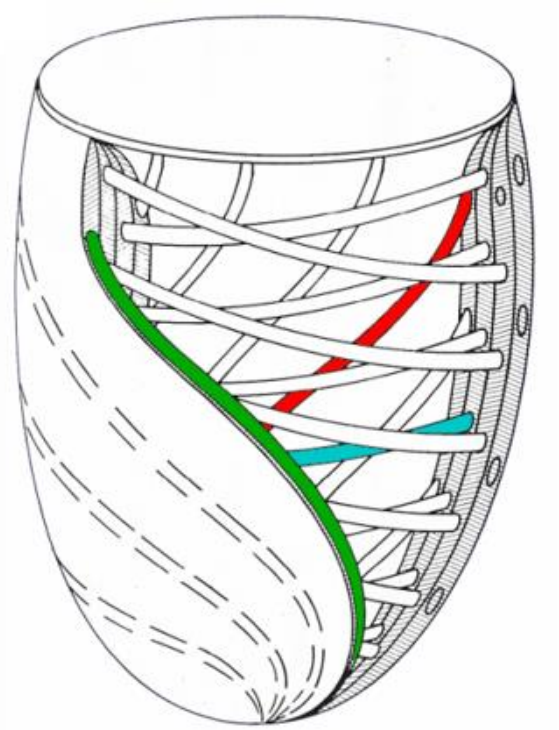

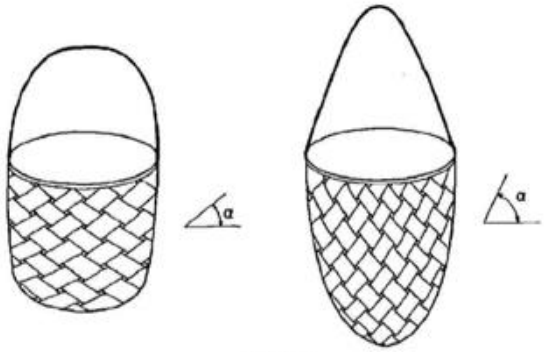

FIGURE 1

Wicker basket made of soft fibers. **Left:** *Unloaded.* **Right:** *Loaded heavily. Note that fiber angle, α, steepens and that fibers lengthen.*

Figure 4. **A.** Cartoon of LV fiber orientation from (Streeter and Hanna 1973). Green: epicardial fiber, left handed helix. Blue: midcardial fiber, circumferential. Red: endocardial fiber, right handed helix. **B.** Streeter's proposed wicker basket model of helix angle change between diastole and systole.

2.1.2. Sheet

Robert Grant conceived and illustrated how fibers might aggregate into a laminar sheet structure (Grant 1965) (Figure 5). But the laminar sheet structure was not actually visualized until 1995 by LeGrice using the histology method (LeGrice, Smaill *et al*. 1995). The discovery of the myocardial sheet exemplified how an obvious structure eluded scientists for a long time. All of the popular experimental mammalian hearts exhibit laminar structures, similar to layers of muscle found in a fish fillet (Figure 6). Myocardial sheet is about four layers of fibers aggregating into a laminar structure (simply called a "sheet" in this thesis). Figure 7 shows the sheet architecture in a fresh, unfixed and unstained mouse left ventricle (Zhang, Cheng *et al*. 2012). Figure 7 is acquired with advanced photoacoustic microscopy (PAM) system. The

significances of the PAM image of myocardial sheet are (1) it is the highest resolution of unfixed sheet to the best of my knowledge; (2) the heart is unfixed, meaning there's minimal dehydration artifacts compared to formalin fixed hearts; (3.) it requires no staining nor contrast agent, saving time and artifacts of doing so; (4) it is a three dimensional imaging modality, suitable for investigating the 3D structure like the heart muscle. For technical details, please refer to (Zhang, Cheng *et al*. 2012).

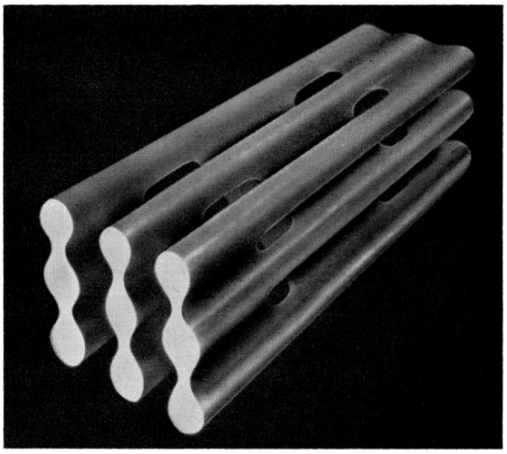

Figure 5. Robert Grant proposed that "planes" can be formed by fibers. "*Schema of fiber to fiber relationship which appears to obtain typically in the left ventricle. While fibers are parallel, by their branchings they form 'planes' which appear to rotate.*" (Grant 1965)

Figure 6. Cooked fish fillet shows sheet structure of skeletal muscle of fish, indicating muscle fibers aggregate into secondary structure in a form of sheets. Cooking helps the separation of sheets, indicating the connective tissues between sheets are more vulnerable to thermal denaturation. The major difference between fish sheet and mammal myocardial sheet is in the fish, fiber is parallel to sheet normal direction. In contrast, in myocardial sheet, fiber is perpendicular to the sheet normal direction.

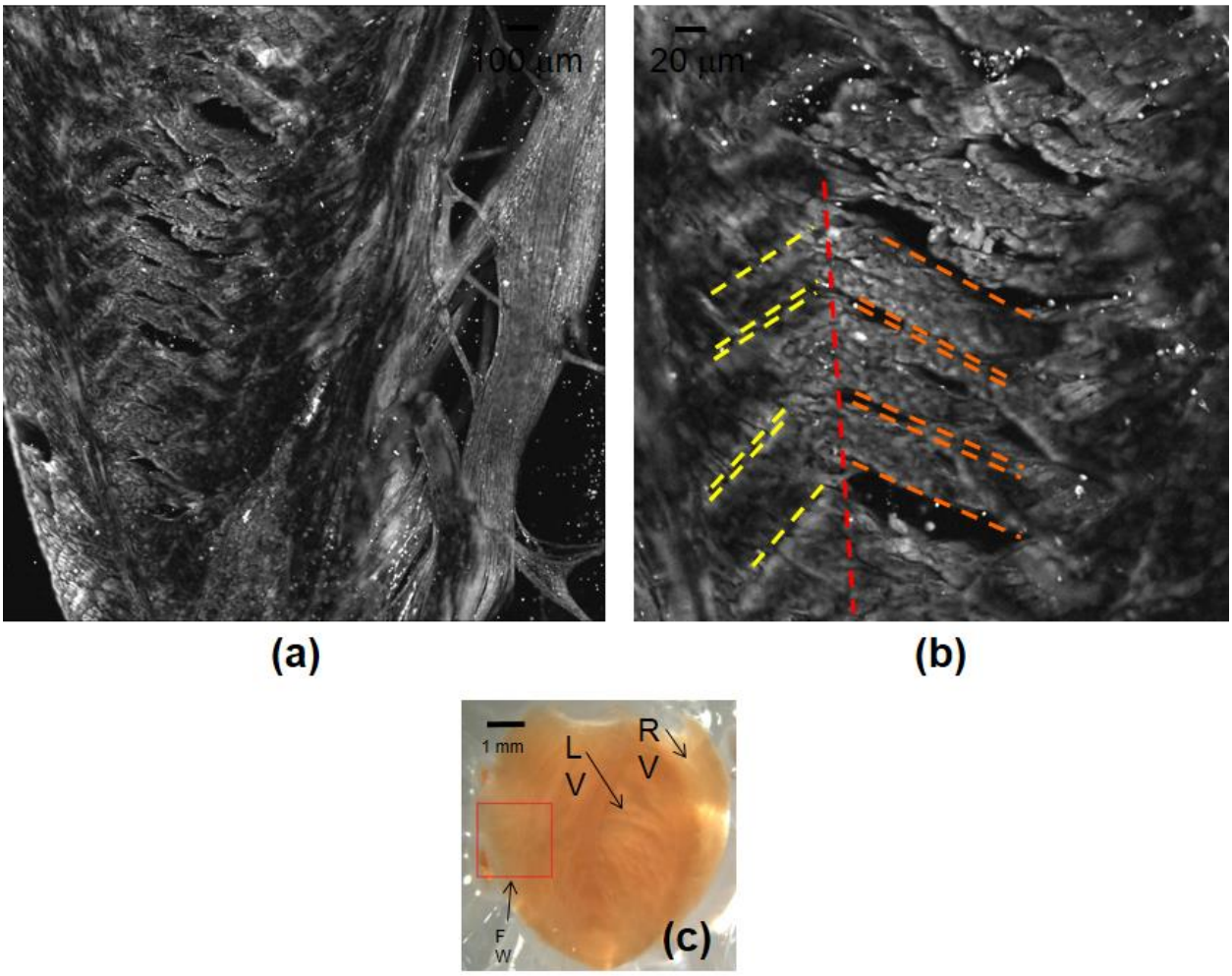

Figure 7. Photoacoustic microscopic (PAM) image of a unfixed, unstained, and un-dehydrated myocardium, showing sheet structure of a mouse left ventricle. (a), PAM image of the left ventricle free wall (FW) marked in (c) acquired at 532-nm wavelength. (b), Close-up PAM image. The boundaries of the branching sheets are apparent. Red dashed line: long axis. Yellow dashed-dot line: sheet boundary. (c), Photograph of the heart specimen. LV, left ventricle; RV, right ventricle. (Zhang, Cheng et al. 2012).

Here is a chronicle summary of important discovery on sheet. After LeGrice visualized the sheets with histology (LeGrice, Takayama *et al*. 1995), Costa and Chen inferred that sheet shearing contributes dominantly to heart wall thickening using radiocinegraphy and DTI, respectively (Costa, Takayama *et al*. 1999; Chen, Liu *et al*. 2005). Using diffusion tensor MRI on alive human subjects, Dou reported that sheets change orientation in cardiac cycle (Dou,

Tseng *et al*. 2003). Specifically, sheets align closer to short axis in systole than diastole. Using confocal histology, Pope reported that sheet presents dominantly at mid- and endocardium but not at epicardium (Pope, Sands *et al*. 2008). Using 9.4T MRI with 3 day long scan time, Gilbert confirmed Pope's finding whith the field of view of a whole heart, revealing more mysterious helical nature of sheets in high resolution (25μm) (Gilbert, Benoist *et al*. 2012). Readers are directed to view the spplemental movie in Gilbert's paper for the 3D whole heart sheet structure.

2.1.3. Nomenclature of the heart segments

Figure 8 illustrates the terminology used to describe the various regions of the heart. This terminology follows AHA consensus (Cerqueira, Weissman *et al*. 2002).

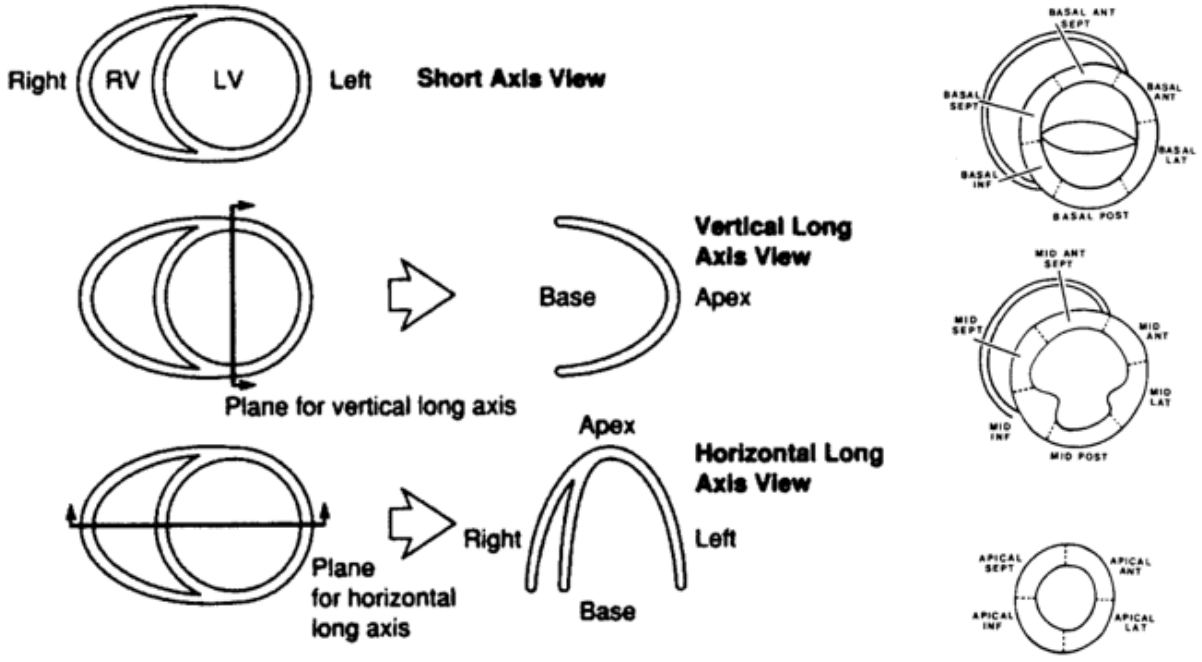

Figure 8. Left ventricle (LV) is rounded in shape in short axis view. Right ventricle (RV) has a semilunar shape. Aorta and vena cava are closer to the heart *base* than the *apex*. Apex is pointing to the left in normal human chest. Heart base is physically closer to the head and has larger diameter than apex.

2.2. Diffusion Tensor MRI

2.2.1. Background

MRI modulates magnetic field to affect nuclear spins to form images (Appendix). Under magnetic gradient, the diffusion of molecules *dephases* the nuclear spins and thus *decreases* MR signal. DTI (Diffusion Tensor MRI) quantifies the ADC (apparent diffusion coefficient) from the signal decay. Specifically, the DTI signal predominantly comes from nuclear spins of water protons. In spin echo imaging, the signal intensity is governed by eq1.

$$S = PD(1 - e^{-TR/T1})\, e^{-TE/T2}\, e^{-bD} \qquad \text{(eq1)}$$

S is signal intensity, **PD** is proton density, **T1** and **T2** are relaxation (decay) times of protons within the samples under given $\mathbf{B_0}$. **D** is the ADC, which represents the observed Brownian motion of water molecules in tissue. **TR** and **TE** are repetition time and echo time. **b** is the diffusion-weighing factor with units of s/mm^2. From eq1, one can see higher **b** value decreases **S** (Basser 1995).

TR, **TE** and **b** can be adjusted on the scanner. Longer **TR** and shorter **TE** generate better signal to contrast ratio (SNR) but require longer scan time and faster responding electronics, which are both more expensive. Tradeoff was made between SNR and scan time. We want D for the diffusion information in it, but it is impossible to calculate the D with just one **S** in eq1. Therefore Stejskal and Tanner devised the two-**S** method to calculate the D (Stejskal 1965). See equations below:

$$S_1 = PD\left(1 - e^{-\frac{TR}{T1}}\right) e^{-\frac{TE}{T2}}\, e^{-b_1 D} = S_0\, e^{-b_1 D} \qquad \text{…….measurement 1}$$

$$S_2 = PD\left(1 - e^{-\frac{TR}{T1}}\right) e^{-\frac{TE}{T2}} e^{-b_1 D} = S_0\, e^{-b_2 D} \quad \text{.....measurement 2}$$

$$\frac{S_2}{S_1} = e^{-(b_2 - b_1) D} \quad \text{(eq2)}$$

Rearranging eq2, we obtain:

$$D = -\ln\left(\frac{S_2}{S_1}\right) / (b_2 - b_1) \quad \text{(eq3)}$$

That is, we can derive a scalar D by attenuating the signal with two different b values. For example, I have used b_1= 0, and b_2=800 (s mm^{-1}) in my work.

2.2.2. Restricted Diffusion

Brownian motion of water molecule in an *isotropic* diffusion environment is characterized by a *single* parameter, the diffusion coefficient, D. For example, in three-dimensional space, random walkers spread with time t according to a Gaussian distribution would have a mean square displacement, $E(x^2) = 6Dt$. That is, in isotropic diffusion environment, D is the same in all direction. However, complexity in the microscopic structure of myocardium restricts water molecular motion anisotropically and results in non-Gaussian diffusion and hence different values of D in different directions. Therefore, instead of a single scalar D, multiple Ds are required to describe the diffusion anisotropy.

To detect anisotropic diffusion, one could repeat Stejskal's two measurements method (eq3) in 6 non-collinear directions to fill in the following matrix **D**:

$$\boldsymbol{D} = \begin{matrix} Dxx & Dxy & Dxz \\ Dyx & Dyy & Dyz \\ Dzx & Dzy & Dzz \end{matrix} \quad \text{(eq4)}$$

The D in eq4 is a 3 x 3 matrix, which is also a rank 2 tensor. For example, Dxx is the ADC in x direction. Dxy is ADC in xy direction, which is in the same direction of the vector (x,y,z)=(1,1,0). From the diffusion tensor, **D**, we can assess magnitude of ADC in different directions. Specifically, the ADC is found to be the greatest in fiber direction and smaller in perpendicular directions. Therefore, the tensor not only provides the orientation information (e.g, which direction has the largest ADC) but also relative ratios of ADCs in different directions (i.e., anisotropy of the diffusion environment, Chapter 3). The fact that water diffusion is restricted by the underlying tissue microstructure provides a unique method of assessing myocardium architecture (Safford, Bassingthwaighte *et al*. 1978; Garrido, Wedeen *et al*. 1994; Ennis and Kindlmann 2006).

In summary, DTI is an established method for 3D reconstruction of myocardial microarchitecture that can depict structural changes across the heart cycle in the intact heart (Chen, Liu *et al*. 2005; Sosnovik, Wang *et al*. 2009). The value of DTI is it is non-invasive, non-destructive, 3-dimensional and rapid, compared to traditional histology (Mori and Zhang 2006; Roberts and Schwartz 2007).

2.1. Method: DTI for *mdx* mice cardiac structure

In the heart, the primary eigenvector is considered to be aligned with the local orientation of cardiac myofibers, and thus defines the fiber angle (α) (Hsu, Muzikant *et al*. 1998; Scollan, Holmes *et al*. 1998; Holmes, Scollan *et al*. 2000; Geerts, Bovendeerd *et al*. 2002). The secondary eigenvector is aligned parallel to sheet surfaces (Tseng, Wedeen *et al*. 2003) and thus defines the sheet angle (β, Figure 9 A). This definition system is based on the fact that eigenvalues of a

diffusion tensor are also the apparent diffusion coefficients describing microscopic diffusion movements, which are the largest in the fiber direction and second largest in the sheet direction (Scollan, Holmes *et al*. 1998; Chen, Suzuki *et al*. 2005).

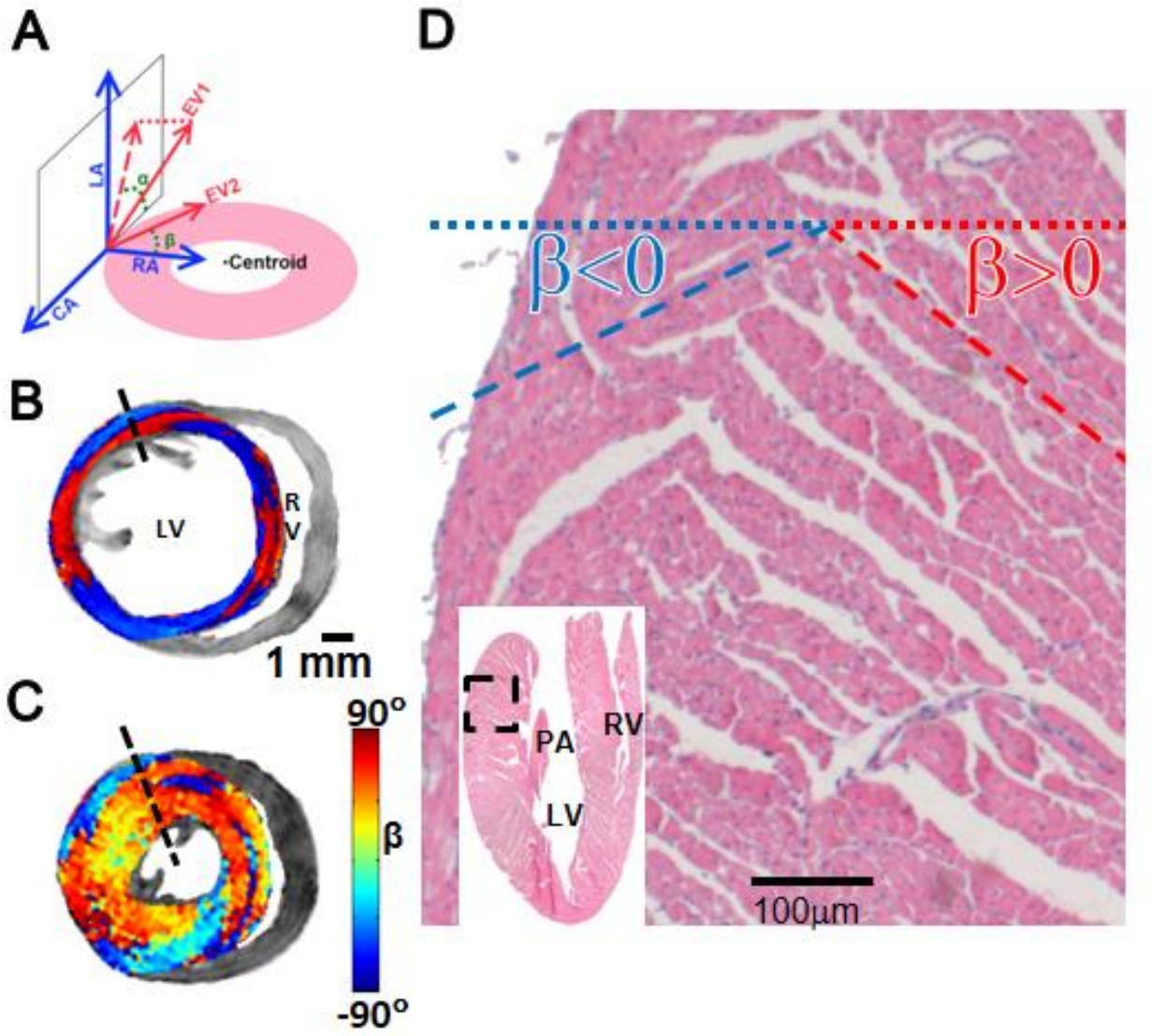

Figure 9. Representative DTI and histology images of sheet architecture in WT mouse hearts. **A**, A local cylindrical coordinate system was used to describe LV myocardial structures. The primary eigenvector (EV1) of the diffusion tensor is characterized by helix angle (α), which is the angle between the circumferential axis and the projection of the first eigenvector onto the circumferential-longitudinal plane; the α shown in A is set as negative. The secondary eigenvector (EV2) is characterized by sheet angle (β), which is the angle between the secondary eigenvector and the radial axis; the β shown in A, toward base and toward endocardium, is set as negative. **B & C**, short-axis views of DTI determined sheet angle (β) in a basal slice of WT heart that was sequentially arrested in diastole (B) and systole (C). The posterior-lateral wall of LV

manifested two populations of β, exhibiting positive (red) and negative (blue) values. D, Histology of sheet organization in a WT heart. Images were acquired from the basal-lateral wall, which is highlighted on the H&E stained image (insert). Two populations of β were observed.(LV, left ventricle; RV, right ventricle; PA, papillary muscle; P, Posterior; L, Left; R, Right; A, Anterior).

Experimental Methods

2.1.1. Langendorff perfusion for DTI

Animals

Adult male *mdx* (C57BL/10ScSn-Dmd*mdx*/J, N=14) and age matched male wild type (WT: C57BL/10SnJ, N=10 and C57BL/6, N=3) mice were purchased from the Jackson Laboratory (Bar Harbor, ME, USA) and the National Institute on Aging (NIA, MD, USA)(18) and housed under a AAALAC-approved facility to 16-month of age. All mice were housed in the same animal facility and cared for under approval by Washington University's animal study committee. All mice were separated into two groups for DTI and optical mapping studies described below.

Isolated Heart Preparation for DTI

Ten *mdx* mice and ten WT mice were used for both diastolic and systolic DTI measurement (Figure 10). Mice were heparinized (1000 U/kg) and anesthetized with isoflurane. Hearts were excised and cannulated for retrograde perfusion using a procedure modified from (Chen, Liu *et al*. 2005). Briefly, hearts were first perfused with Krebs buffer at 60 mmHg constant pressure for approximately 5 min to wash out the residual blood. Five *mdx* hearts and five WT hearts were perfusion-arrested in diastole (perfusion pressure = 60 mmHg) with regular

St. Thomas' cardioplegic solution containing normal [Ca^{2+}] of 1.2 mmol/L (denoted as *mdx*-NC and WT-NC, respectively) under room temperature. DTI of diastolic arrested hearts was performed for 1.5 hours. After that, hearts were reperfused with 37℃ Krebs buffer to resume beating. Upon stabilization of contraction (~6 min, up to 300 beats per min), 2.5 mmol/L Ba^{2+} was then introduced to induce systolic cardiac contracture while Ca^{2+} was lowered to 0.078 mmol/L (Munch, Comer *et al*. 1980; Toyota, Fujimoto *et al*. 2002; Chen, Liu *et al*. 2005). To evaluate the effect of [Ca^{2+}] on diastolic cardiomyocyte architecture in *mdx* mice, another five *mdx* hearts and five WT hearts were perfusion-arrested in diastole with a modified cardioplegic solution containing low [Ca^{2+}] of 0.078 mmol/L (denoted as *mdx*-LC and WT-LC, respectively). The 0.078 mmol/L [Ca^{2+}] was chosen over the calcium-free condition to minimize the risk of complete depletion of intracellular calcium, which can cause calcium overload upon reperfusion with solutions containing normal [Ca^{2+}], thereby exerting unfavorable effects on certain ion channels (Munch, Comer *et al*. 1980; Robinson and Harwood 1991).

The systolic arrest of *mdx*-NC, WT-NC, *mdx*-LC, and WT-LC (defined below) are all achieved with the same modified Tyrode solution containing 2.5 mmol/L Ba^{2+} and 0.078 mmol/L Ca^{2+} (Chen, Suzuki *et al*. 2005). All solutions were equilibrated with 95% O2 plus 5% CO2 (PH 7.4) and contained adenosine (45μmol/L) to maximally dilate the coronary vessels (Judd, Rottman *et al*. 1992). Bovine serum albumin (BSA; 61 μmol/L) was added to the perfusate to minimize interstitial edema (Dunphy, Richter *et al*. 1999; Watts and Maiorano 1999). DTI of systolic contracture hearts were conducted for ~1.5 hours. Upon the completion of MRI, all hearts were perfused with 10% formalin for histological study.

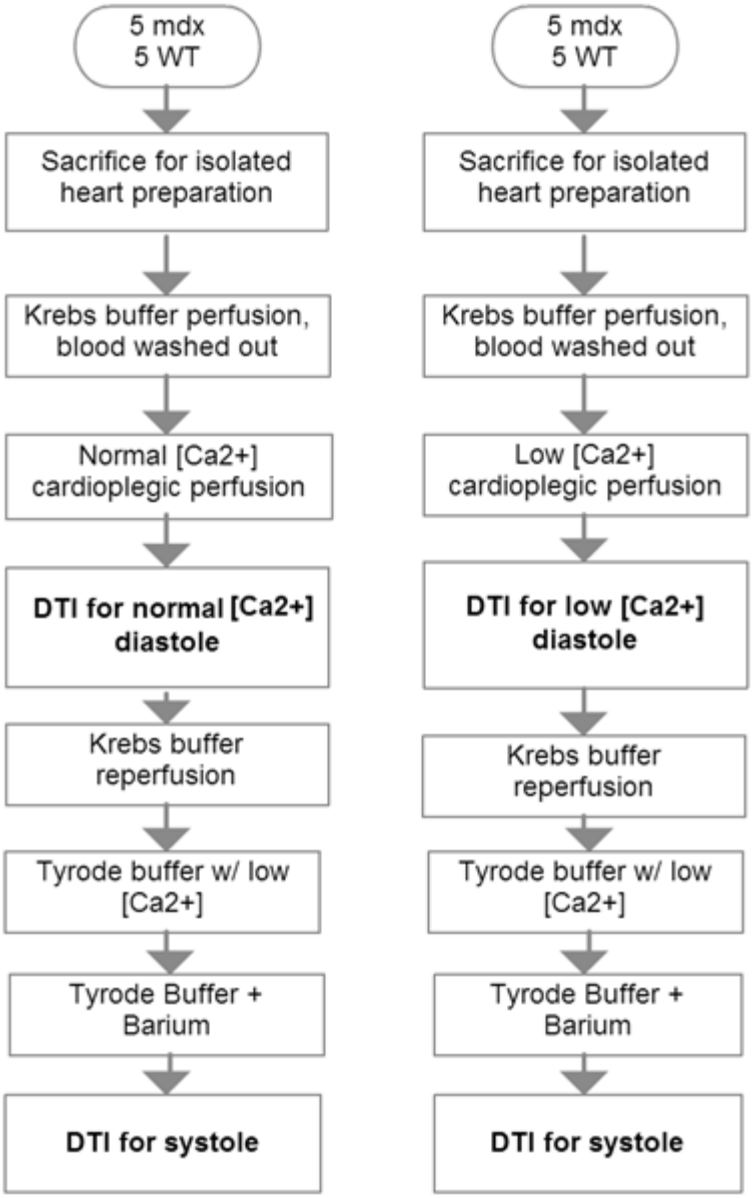

Figure 10. Flow chart for DTI acquisitions for diastolic and systolic arrested hearts. Left, ten mice perfused with normal calcium (NC) concentration for diastolic arrest then high barium for systolic arrest. Right, ten mice perfused with low calcium concentration (LC) for diastolic arrest then high barium for systolic arrest. See text for details.

2.1.2. Perfusion compatible MR Coil

A dedicated MRI-compatible retrograde mouse heart perfusion system was made. This system provides a quantitative and non-destructive assessment of diastolic and systolic myocardial architecture from the same heart. The system includes: (1) a custom-built 15 mm-diameter solenoid coil, which provides high SNR: 65 for non-diffusion weighted images and 40 for diffusion weighted images (See Figure 11 for the coil design.); (2) a Langendorff constant-pressure perfusion apparatus. The constant perfusion pressure is controlled by a reservoir with constant height. Perfusate efflux was removed by vacuum suction. The heart was contained in a plastic tube made by syringe, which is omitted in Figure 11 for simplicity but is important to prevent contact between perfusate and the copper coil. A variable capacitor was soldered at the center of the gap of the single turn copper coil for resonance frequency tuning. The distance, **h**, between the cable loop and the copper coil determines the coefficient of coupling, **k**, which determines the mutual inductance, **L**.

$\mathbf{L} = \mathrm{k}\sqrt{L_1 L_2}$, k is between 0 (when h is large) and 1 (when d is small) (eq5)

The Figure 11 B is an equivalent circuit of my coil. The resonance frequency, $\boldsymbol{f}$, of the circuit can be determined by series RLC resonator. Practically, **L** and **C** were adjusted to resonate at 499.70 MHz for the 11.7 tesla ultra-high field MR scanner used in this study.

$$f = \frac{1}{\sqrt{LC}} \quad \text{(eq6)}$$

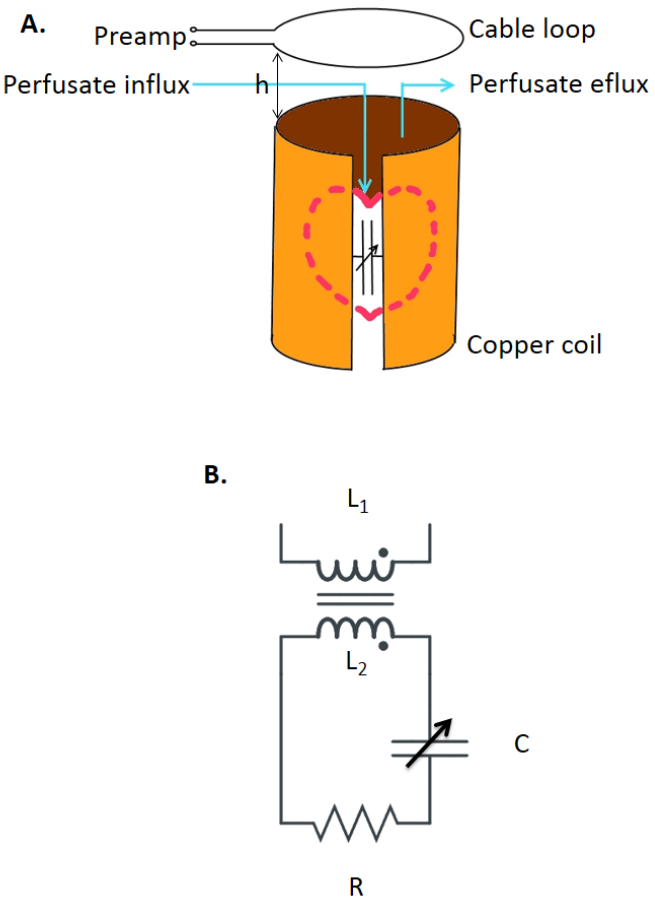

Figure 11. **A.** Cartoon of single turn solenoid coil and perfused mouse heart setup. A plastic tube containing the heart and preventing perfusate from contacting the copper coil is omitted for visual simplicity. Distance between the cable loop and the copper coil is denoted by h. **B.** Equivalent circuit. R is the resistance of loading (perfusate and heart) and copper. L_1 is the inductance of the cable loop. L_2 is the inductance of the copper coil. C is variable capacitor.

2.1.3. Imaging parameters

All MRI experiments were performed on a Varian 11.7 tesla small animal MR scanner (Varian Associates; Palo Alto, CA). Long-axis scout images were acquired as previously described (Chen, Liu *et al*. 2005). A multislice spin-echo sequence with diffusion-sensitizing gradients were used to acquire short-axis, diffusion weighted images. Diffusion-sensitizing gradients were applied in six noncolinear directions. Imaging parameters were as follows: echo time, 46 ms; time interval between diffusion-sensitizing gradients, 30 ms; b-value, 0 and 800 s/mm^2; in-plane resolution, 125 × 125 μm^2, repetition time, 3 s; and image-acquisition time, 1 h. For diastolic arrested hearts, eight contiguous slices (thickness = 0.7 mm) extending from the

base to apex were acquired. For systolic contracture hearts, eight contiguous slices were acquired with slice thickness adjusted to 0.55–0.65 mm based on the fraction of longitudinal shortening. Attention was paid to keep the slice selection and the heart orientation the same between diastole and systole imaging.

2.1.4. Post processing, sheet angle calculation (β)

All MR images were processed using custom-developed software written in Matlab (The MathWorks Inc., M.A., USA) as described previously (Chen, Liu *et al*. 2005). Specifically, fiber helix angle (α) and sheet angle (β) were calculated based on a right-handed helix, the fiber helix angle (α) was calculated as the angle between the circumferential cardiac axis and the projection of the first eigenvector of the diffusion tensor onto the circumferential-longitudinal plane (Scollan, Holmes *et al*. 1998). Sheet angle (β) was determined as the angle between the secondary eigenvector and the radial axis. Sheet inclination toward the base from endocardium to epicardium was set as positive (Figure 9 D) (Scollan, Holmes *et al*. 1998; Tseng, Wedeen *et al*. 2003). Because regional wall thickening is accompanied by a reduced magnitude of the sheet angle, |β|, therefore |β| was used to analyze sheet function (LeGrice, Takayama *et al*. 1995; Chen, Liu *et al*. 2005). LV wall thickness was calculated as the mean distance between epicardial and endocardial borders. The transmural difference of α, defined as the difference in endocardial and epicardial helix angles, i.e., $\Delta\alpha = \alpha_{endocardium}-\alpha_{epicardium}$, was used to quantify transmural changes of fiber orientation.

2.1.1. Statistical methods

Statistical differences were assessed with the analysis of variance (ANOVA) or the multivariate analysis of variance (MANOVA) as appropriate. Bonferroni correction was applied

to post-hoc comparisons. A value of $p < 0.05$ was considered significant. Data were expressed as mean ± standard error of the mean (S.E.). All statistics were conducted with the IBM SPSS Statistics program.

2.1.2. Histology

After DTI acquisition, five *mdx* and five wildtype hearts were rapidly fixed in 10% formalin. Fixed hearts were sliced into four blocks with 2 mm thickness from base to apex. Each slice was embedded in paraffin and sectioned at 4 μm thickness. The tissue sections were stained with picrosirius red for the identification of fibrosis (Van Erp, Irwin *et al*. 2006). The extent of myocardial fibrosis was quantified from digitized histological images using a thresholding algorithm implemented in Matlab. Regions that demonstrate stronger red-to-green ratio in picrosirius red staining were considered to represent interstitial fibrosis. The percentage of tissue fibrosis was calculated as the ratio of pixels representing fibrotic tissue vs. pixels of the entire short-axis slice, and the average value in two adjacent slices was used in analysis.

2.2. Results: Sheet function in 16-month old *mdx* mouse hearts

2.2.1. Morphological observation of β with histology and PAM

DTI, histology, and PAM all show a similar transmural morphological character of sheet, that is, a sharp change of β at midmyocardium of basal posterior mid-wall (Figure 12).

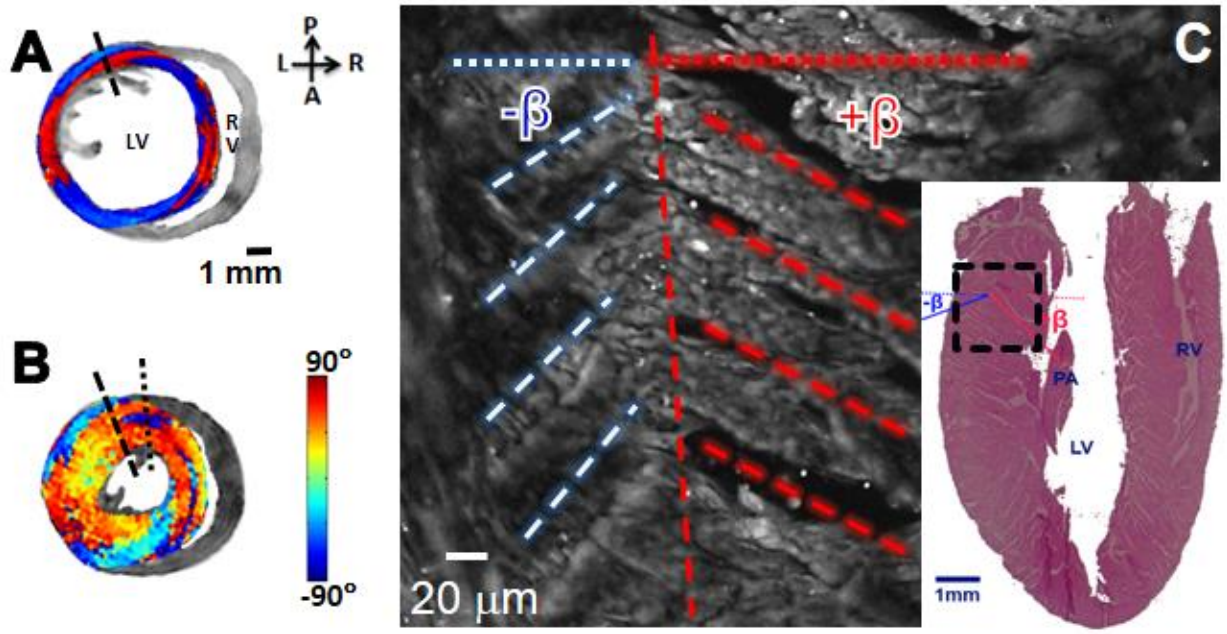

Figure 12. **A & B**, representative short-axis view of DTI determined sheet angle (β) in a basal slice of the same WT heart that was sequentially arrested in diastole (A) and systole (B). The posterior-lateral wall of LV possessed two populations of β, exhibiting positive (red) and negative (blue) values. The transmural portion of positive β is increased in systole (compare the portions of red-colored pixels under the dashed lines in A & B). The dotted line in B indicates a 3 population β transition that appears only in systole. **C**, Photoacoustic microscopy of long-axis view of a freshly half-split WT mouse heart confirmed two populations of β in LV wall. The insert showed H&E stained long-axis WT mouse heart slice with the corresponding region of photoacoustic image squared. LV: left ventricle. RV: right ventricle. PA: papillary muscle.

2.2.2. 16 month old *mdx* hearts manifest reversible regional diastolic sheet dysfunction

DTI defined two populations of β with opposite signs in the LV wall of WT and *mdx* mice, as confirmed by several previous reports (LeGrice, Smaill *et al*. 1995; Tseng, Wedeen *et al*. 2003; Chen, Liu *et al*. 2005; Helm, Beg *et al*. 2005; Gilbert, Benson *et al*. 2007; Pope, Sands *et al*. 2008). Under conditions of barium-induced systolic arrest, |β| value is decreased in systole (Figure 9 B&C, Figure 13 A&B), agreeing with *in vivo* and *ex vivo* observations (LeGrice, Smaill *et al*. 1995; LeGrice, Takayama *et al*. 1995; Costa, Takayama *et al*. 1999; Chen, Liu *et al*.

2005). At each short-axis imaging slice, the slice-averaged systolic |β| was comparable among all groups of hearts (Figure 13 B, p = N.S.). However, the diastolic |β| of *mdx* hearts (*mdx*-NC) was ~10° lower than that of WT hearts (WT-NC) at the base when perfused with regular cardioplegic solution ($p < 0.05$, Figure 13 A). The |β| at the apex of *mdx-NC* hearts appeared normal (p = N.S. compared to WT-NC at each corresponding short-axis imaging slice), demonstrating that diastolic sheet dysfunction in *mdx* hearts occurred focally at the base. By reducing the $[Ca^{2+}]$ of the cardioplegic solution to 7% of its regular concentration, a complete and rapid restoration of diastolic | β | in *mdx* hearts (*mdx*-LC) to normal values was observed. No effect of calcium manipulation on WT cardiac sheet function was observed (WT-LC, p = N.S. compared to WT-NC at each corresponding short axis imaging slice), indicating that the diastolic sheet dysfunction in *mdx* hearts was substantially calcium dependent. These data suggest that even at this advanced age, a principle mechanical abnormality in *mdx* mice likely is associated with regionally-dependent incomplete sarcomere relaxation.

At the base, further regional analysis indicated that the maximal decrease of diastolic |β| in *mdx*-NC hearts occurred in the endocardium. Compared to WT-NC, *mdx*-NC exhibited 13° lower |β| (75° ± 2° vs. 62° ± 3°) in the endocardium (inner 1/3 wall-depth in transmural direction); 10° lower |β| (74°± 1° vs. 64° ± 2°) in the midcardium (middle 1/3 wall-depth in transmural direction); and 8° lower |β| (68° ± 2° vs. 60° ± 2°) in the epicardium (outter 1/3 wall-depth in transmural direction) (Figure 13 C). Moreover, in the posterior-lateral wall, the diastolic |β| was 51° ± 6° in *mdx*-NC (Figure 13 F). This value was approximately 20° lower than that of *mdx*-LC (70°± 4°), as well as that of WT-NC (72° ± 4°) or WT-LC (72° ± 6°) groups ($p < 0.05$ for all comparisons. See post hoc multiple comparison in Table 2 in page 107). Together these

findings indicate a clear regional and transmural dependence of incomplete relaxation, despite the ubiquitous dystrophin mutation.

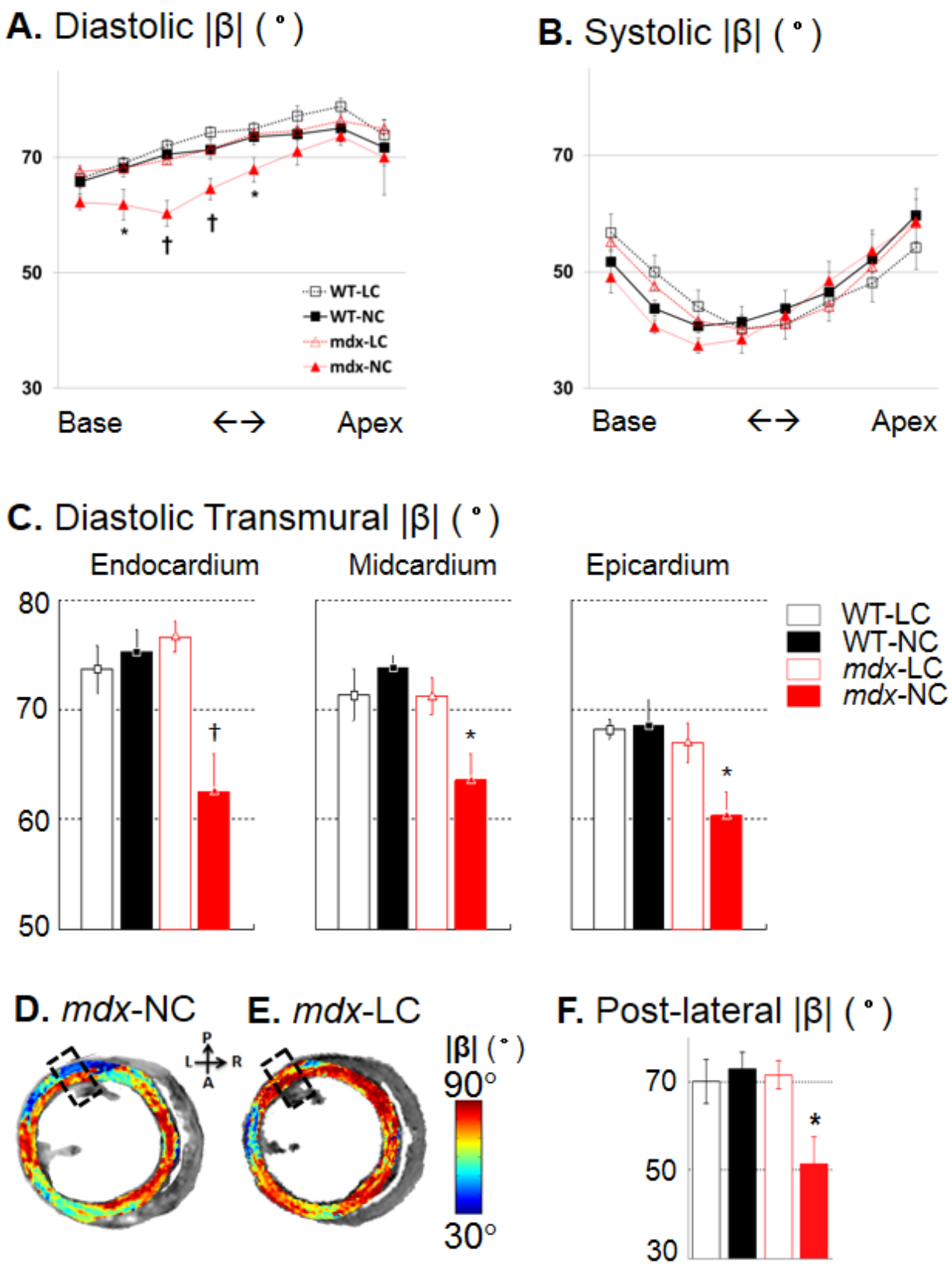
A. Diastolic |β| (°)
70
50
30
WT-LC
WT-NC
mdx-LC
mdx-NC
Base
Apex
B. Systolic |β| (°)
70
50
30
Base
Apex
C. Diastolic Transmural |β| (°)
Endocardium
Midcardium
Epicardium
80
70
60
50
WT-LC
WT-NC
mdx-LC
mdx-NC
D. mdx-NC
E. mdx-LC
P
L
R
A
|β| (°)
90°
30°
F. Post-lateral |β| (°)
70
50
30

Figure 13. DTI-determined diastolic and systolic |β| in short-axis slices. **A**, *mdx* hearts exhibited abnormally lower diastolic |β| that was recovered to normal value after reducing [Ca^{2+}] in the perfusate. For hearts perfusion-arrested in diastole with normal calcium solution, *mdx* hearts (*mdx*-NC) exhibited lower |β| than did WT (WT-NC) hearts with the maximal ~10 degree difference occurred at the basal region. In contrast, *mdx* hearts perfused with the low calcium solution (*mdx*-LC) exhibited normal diastolic |β|. Varying [Ca^{2+}] had no effect on diastolic |β| in WT hearts (WT-LC). **B**, systolic |β| exhibited no difference among four groups of hearts. **C**, diastolic |β| in the epicardium, midcardium, and endocardium at the base of WT and *mdx* hearts. In all regions, diastolic |β| of *mdx*-LC hearts were comparable to that of WT-LC and WT-NC hearts, but all are higher than that of *mdx*-NC hearts. The largest difference in diastolic |β| between *mdx*-LC and *mdx*-NC was observed in the endocardium. **D & E**, representative DTI-determined diastolic |β| maps on short-axis slices at the base of *mdx*-NC and *mdx*-LC hearts. The lower |β| in *mdx*-NC heart, indicated by fewer regions with red color, was visually appreciable. F, in the posterior-lateral region (the areas enclosed by dashed line in D & E), the diastolic |β| of *mdx*-NC hearts was approximated 20 degree lower than that of *mdx*-LC hearts and of all WT hearts. Data represent mean ± SEM. N = 5 for each group. *, $p < 0.05$; †, $p < 0.005$ for the indicated short axis location.

2.2.3. 16 month old *mdx* and WT hearts exhibit similar fiber organization and function

Wall thickness and through-wall differences of myofiber helix angle (Δα) were similar between *mdx* and WT mice (Figure 14), suggesting that the major mechanical abnormality was confined to sheets rather than fibers. The normal wall thickness agrees with former publications (Li, Liu *et al*. 2009; Stuckey, Carr *et al*. 2012)

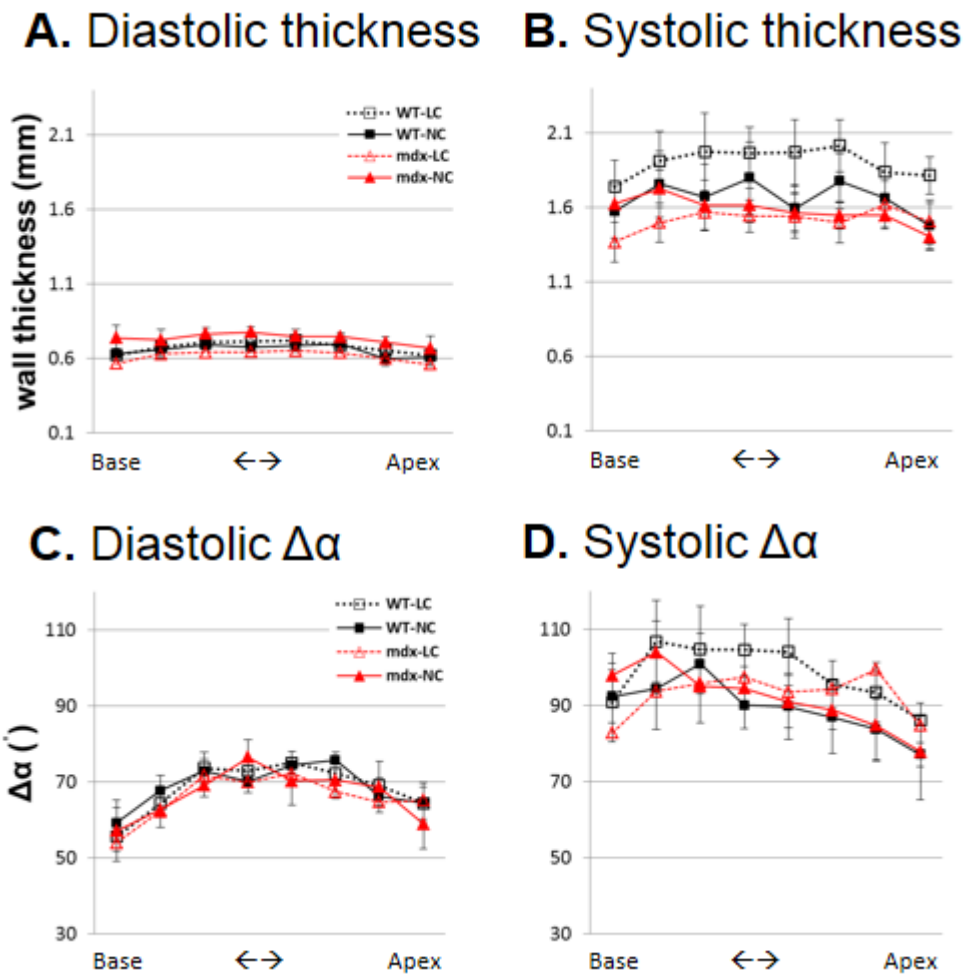

Figure 14. Averaged wall thicknesses in each short axis slice are similar in all four groups, in both diastole (**A.**) and in systole (**B.**) Averaged through-wall myofiber helix angle differences (Δα) in each short axis slice are similar in all four groups, in diastole (**C.**) and in systole (**D.**). Overall, Δα is increased in systole, agreeing with a prior publication (Chen, Liu *et al*. 2005). No significance was detected in all comparison in each panel.

2.2.4. 3 month old *mdx* mice exhibit smaller sheet dysfunction, still reversible by low calcium perfusion

The max difference in |β| between *mdx*-NC and *mdx*-LC is $6.1^{\circ} \pm 3.6^{\circ}$ ($p < 0.66$, Table 3 in page 110) and $9.3^{\circ} \pm 2.26^{\circ}$ ($p < 0.005$, Table 2 in 107), both at base in 3- and 16-month old mice respectively (Figure 15), indicating that this $[Ca^{2+}]$-dependent sheet dysfunction is also loci dependent.

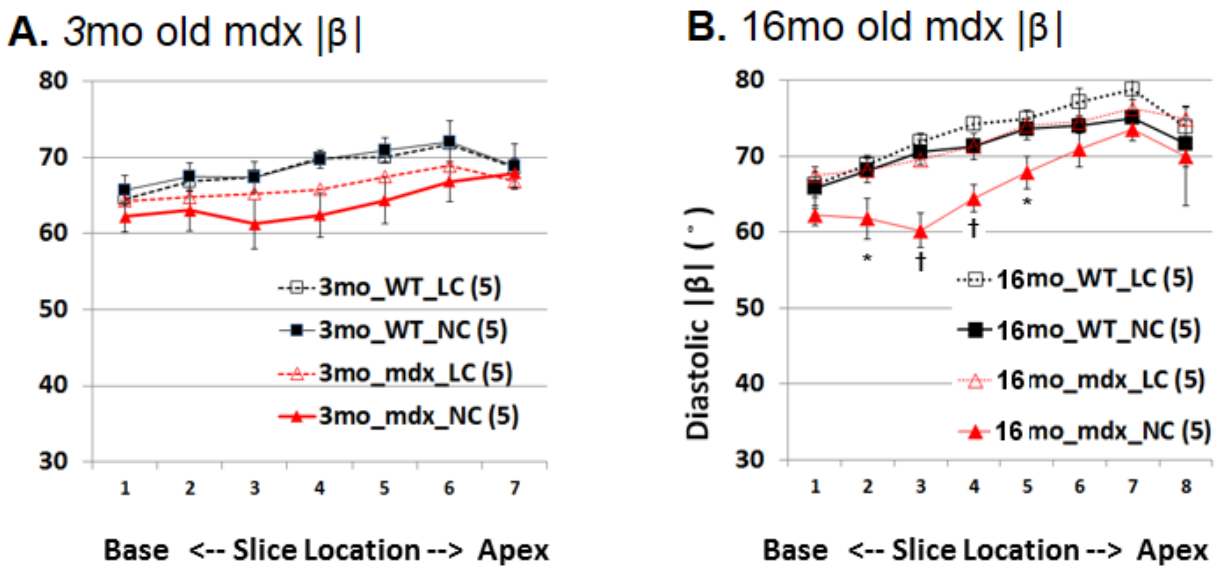

Figure 15. **A.** |β| of 3 month old *mdx* and WT mice under normal calcium (NC) and low calcium (LC) perfusion. **B.** |β| of 16 month old *mdx* and WT mice under NC and LC perfusion. Data represent mean ± SEM. N = 5 for each group. *, $p < 0.05$; †, $p < 0.005$ for the indicated short axis location.

2.3. Discussion of |β|

This study shows for the first time that *mdx* hearts exhibit an abnormal myocardial sheet angle magnitude, |β|, in diastole but not in systole. Agreeably, Goldberg reported that DMD patients have abnormally slower wall thinning but normal wall thickening in echocardiography (Goldberg, Feldman *et al*. 1980) (Figure 16), indicating that dystrophin affects normal diastolic rather than systolic function. Furthermore, regional and intramural gradients of diastolic dysfunction (Figure 13 A & C) are evident, primarily in the more basal segments where abnormal calcium handling also occurs (Chapter 4).

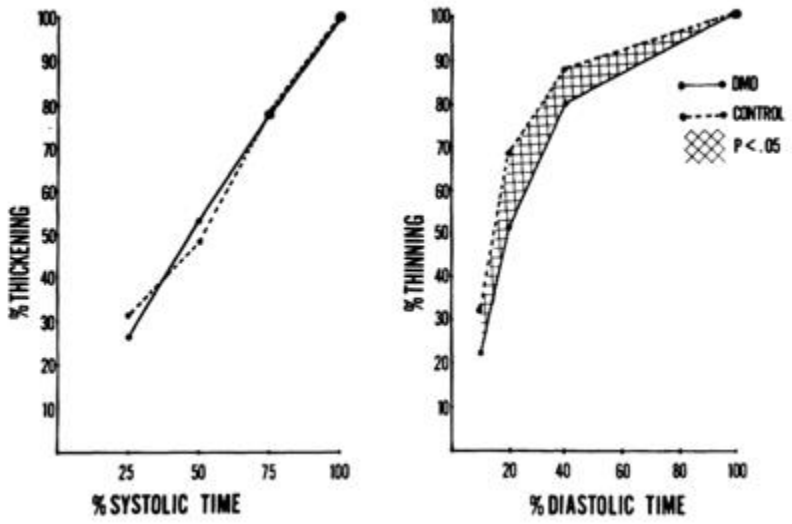

Figure 16. Using echocardiography, Goldberg has shown that DMD patient heart has significantly slower wall thinning but normal wall thickening, indicating that the absence of dystrophin affects diastolic function more than systolic function, agreeing with the DTI measured sheet angle data in Chapter 2. Figure from (Goldberg, Feldman *et al*. 1980).

These co-localized abnormalities in calcium handling and diastolic calcium-dependent sheet dysfunction strongly suggest that features other than the simple absence of dystrophin are critical to the evolution of heart failure in DMD. Indeed, it is well recognized that the mechanical defect in the dystrophin encoding gene does not independently elicit DMD cardiac dysfunctions such as reduced circumferential wall strain (Ashford, Liu *et al*. 2005), which emerge in a regionally heterogeneous fashion over time, and not at all loci where dystrophin is missing. This loci-dependency agrees with my findings.

Given that systolic $|\beta|$ < diastolic $|\beta|$ (Figure 13 A & B), the observed lower diastolic $|\beta|$ in *mdx* heart may reflect that cardiomyocytes are not fully relaxed in diastole. We also confirmed that this regional diastolic sheet dysfunction in *mdx* hearts is a likely consequence of cytosolic calcium mishandling, because the regional diastolic sheet dysfunction is quickly reversible upon perfusion with a lower level of calcium (Figure 13 A, *mdx*-NC vs *mdx*-LC).

Chapter 3: Anisotropy information in DTI

3.1. Introduction

In Chapter 2, I have used orientation information (β) derived from DTI to detect the basal myocardial function abnormality. In this Chapter, I sought for the first time to further explore the shape information with fractional anisotropy (FA) and mode of anisotropy (mode) to elucidate regional abnormal myocardial fiber/sheet shape in *mdx* mice hearts. Please refer to Chapter 2 for DTI background and methods. Refer to Advanced Engineering Mathematics by Erwin Kreysiz (9^{th} ed) for tensor matrix properties.

Each diffusion tensor can be decomposed into three eigenvectors and three corresponding eigenvalues. Eigenvectors carry orientation information, while eigenvalues provide anisotropic information for the micro-diffusion environment in the voxel (Bahn 1999). A tensor invariant is a scalar value calculated from eigenvalues. For examples, trace and norm are wildely used tensor invariants in DTI:

$$trace = \lambda_1 + \lambda_2 + \lambda_3 = 3 \times ADC, \qquad where\ \lambda_{1\sim3}\ are\ eigenvalues$$

……..eq10

$$norm = \sqrt{{\lambda_1}^2 + {\lambda_2}^2 + {\lambda_3}^2}$$

……..eq11

In an eigenvalue space of a 3-D Cartesians coordinate system, norm is the distance between the origin and the point, (λ_1, λ_2, λ_3). Trace is the sum of the coordinates. The trace is three times of the quantity of the apparent diffusion coefficient (ADC), which is an effective indicator of

stroke-sites in brain (van Gelderen, de Vleeschouwer *et al*. 1994; Latt, Nilsson *et al*. 2009). The norm is a measure of total magnitude of diffusion (Grant 1965). Trace and norm are both in the units of mm^2/sec, the same as the unit of eigenvalues.

For example, fractional anisotropy (FA) and mode are two independent scalar values calculated from eigenvalues (Figure 17). FA has been widely used in many DTI measurements (Pierpaoli and Basser 1996), especially in the brain (Papanikolaou, Karampekios *et al*. 2006). Recently, FA has been applied to delineate the contraction-induced assumption of more isotropy for tissue architecture in skeletal muscle (Galban, Maderwald *et al*. 2004; Deux, Malzy *et al*. 2008). Mode was proposed in 2006 as an FA-independent metric for anisotropy (Ennis and Kindlmann 2006). Mode has been used to detect microstructural anatomy of epidermoid cysts and nerve fibers (Jolapara, Kesavadas *et al*. 2009; Douaud, Jbabdi *et al*. 2011). However, dynamic changes in myocardial architecture for genetically abnormal dystrophic hearts have not been investigated with the use of FA or mode. Although FA is more widely used in DTI, we propose to include also mode to describe the anisotropy in myocardium, because "*No single scalar parameter can be constructed which reflects all of the information about anisotropy which is contained in the eigenvalues"* (Bahn 1999). The 3D information acquired in perfused viable *mdx* hearts should allow delineation of both the locus (regional and intramural) and the cycle dependence (diastole vs. systole) of the principle cardiac defects in dystrophin-deficiency and whether these defects might be reversible (i.e. functional) consequences of calcium mishandling (please refer to Chapter 4) or be nonreversible consequences of fibrosis (i.e., remodeling).

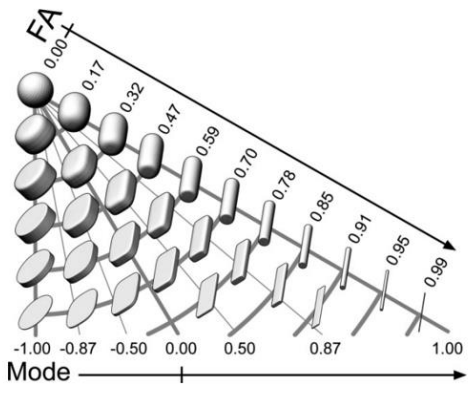

Figure 17. Demonstration of anisotropic space spanned by FA and Mode. From (Ennis, 2006)

3.2. Method: DTI Data Analysis for FA and mode

Please refer to Chapter 2 for isolated Heart Preparation for DTI and MRI procedure. The dataset is the same as acquired in Chapter 2. However, new signal processing method was used to extract information from the dataset. All MR images were processed using custom-developed software written in Matlab. FA and mode are both calculated from eigenvalues and eigenvectors of tensors according to the standard formulas below (Ennis and Kindlmann 2006).

$$FA = \sqrt{\frac{1}{2}}\frac{\sqrt{(\lambda_1 - \lambda_{mean})^2 + (\lambda_2 - \lambda_{mean})^2 + (\lambda_1 - \lambda_{mean})^2}}{\sqrt{{\lambda_1}^2 + {\lambda_2}^2 + {\lambda_3}^2}}$$

$$= \sqrt{\frac{3}{2}}\frac{\sqrt{(\lambda_1 - \lambda_2)^2 + (\lambda_2 - \lambda_3)^2 + (\lambda_1 - \lambda_3)^2}}{\sqrt{{\lambda_1}^2 + {\lambda_2}^2 + {\lambda_3}^2}}$$

$$, where\ \lambda_{1\sim3}\ are\ eigenvalues\ and\ \lambda_{mean}\ is\ the\ average\ of\ \lambda_{1\sim3}$$

……..eq12

$$mode = 3\sqrt{6}\det\left(\frac{A_{aniso}}{|A_{aniso}|}\right), where\ A_{aniso} = A - \frac{\sqrt{(ev_1 + ev_2 + ev_3)}}{3} \times I_3$$

……eq13

3.3. Result

3.3.1. *mdx* and WT hearts exhibit lower FA & higher mode

In all hearts, systolic FA was ~40% lower than diastolic FA ($p < 0.05$ for all comparisons, Figure 18), indicating that a more isotropic diffusion environment was elicited by cardiac contraction (Galban, Maderwald *et al*. 2004; Deux, Malzy *et al*. 2008), as expected from fibers shortening in the long-axis and expanding in the short axis (i.e., becoming rounder, or less oblong). Generally, systolic FA is lower (i.e., spherical instead of a ellipsoidal shape) and mode is higher (i.e., oblong instead of a discoid shape, Fig63) than those of diastole (Fig64). In diastole, *mdx*-NC hearts exhibited abnormally low FA and high mode compared to WT, indicating a regional unrelaxed myocardial fiber/sheet architecture. After perfusing the *mdx* heart with low [Ca^{2+}] (*mdx*-LC in Fig64) cardioplegic solution, recovery of diastolic FA and mode to normal values were observed.

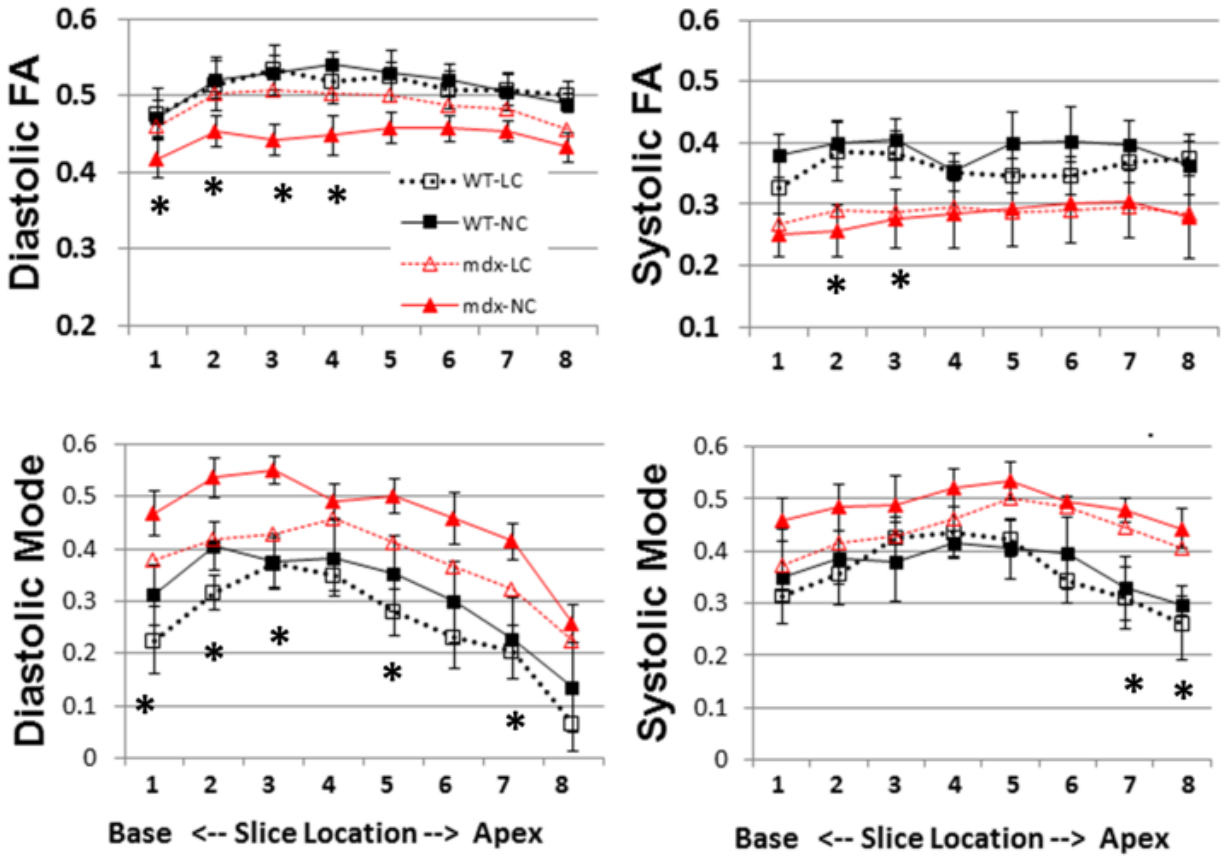

Figure 18. DTI-determined FA and mode in diastole and systole of WT and mdx mouse heart. N = 5 for each group. *, $p < 0.05$. NC, normal calcium. LC, low calcium concentration perfusion. See Methods in Chapter 2.

3.4. Discussion – abstract shape information

The low diastolic FA of *mdx* hearts, indicating more isotropic fiber/sheets organization (Galban, Maderwald *et al*. 2004; Deux, Malzy *et al*. 2008), also demonstrates this diastolic mechanical defect of *mdx* hearts. Systolic FA of *mdx* is lower than that of WT, indicating while the mechanical sheet orientation is not affected by the absence of dystrophin in systole, the microstructural environment of muscular architecture is affected. This requires further investigation.

This study shows for the first time that myocardium microstructure of *mdx* mice exhibits abnormal anisotropy that is calcium dependent, loci-dependent,[7] and rapidly reversible. Given that barium-induced cardiac contraction leads to lower FA and higher mode, the observed lower diastolic FA and higher diastolic mode in *mdx* hearts all reflect that *mdx* cardiomyocytes are not fully relaxed in diastole.

FA and mode describe the anisotropy of water diffusion in the microscopic environment that could represent several factors, including cell shape/size, extra/intracellular volume ratio, myofiber dispersion, and myocardial sheet extension, all of which broadly impact electromechanical cardiac function. The observation that changing cytosolic [Ca^{2+}] regulates the FA and mode in *mdx* hearts suggests that restoration of cell environment by allowing complete relaxation in diastole can be achieved rapidly by transient adjustments in sarcoplasmic calcium levels. Accordingly, diastolic dysfunction in *mdx* mice may be reversible in part with measures aimed at restoring normal calcium handling, and is not a permanent pathophysiological feature of the disease. Thus, FA and mode are quantitative tissue based metrics to assess microarchitectural alterations in cardiomyopathy.

[7] Loci-dependent: base is abnormal while apex is normal.

Chapter 4: Optical mapping for calcium transients in *ex vivo* viable *mdx* hearts

4.1. Acknowledgements to the contribution of Dr. Efimov's lab

After I have found the calcium-dependent regional sheet dysfunction described in last Chapter, Samuel Wickline and me proposed a collaboration to Igor Efimov's lab to test the hypothesis of regional abnormal calcium handling in a whole perfused mouse heart. I thank Di Lang, Chaoyi Kang, and Igor Efimov for their generous help on optical mapping for studying the calcium transients of 16 month old (old) and 3 month old (young) *mdx* mice. Di found that the basal calcium transients are abnormally prolonged only when the heart is stretched in old but not young *mdx* mice, for the first time. Combining Di's optical mapping findings with my DTI findings, we were able to infer that *mdx* cardiomyopathy is calcium- and loci- dependent (Cheng, Lang *et al*. 2012).

4.2. Why use optical mapping for calcium?

Ca^{2+} released by sarcoplasmic reticulum (SR) in cardiac muscle triggers conformation change in troponin, allowing the binding between actin and myosin and the following sliding action, and results in macroscopic contraction of cardiac muscle. The Ca^{2+} is released from the openings of SR Ca^{2+} release channel (ryanodine receptor, RyR). The voltage-gated sarcolemmal L-type Ca^{2+} channels (dihydropyridine receptors, DHPRs) locally increase $[Ca^{2+}]i$ and thereby activate the RyRs by Ca^{2+}-induced Ca^{2+} release (CICR). After contraction, sarco/endoplasmic reticulum Ca^{2+}-ATPase (SERCA) uptake the cytosol Ca^{2+} into SR, allowing relaxation (Cheng, Lederer *et al*. 1996). This CICR and Ca^{2+} recycling triggers every heart cycle. How

cardiomyocytes handle calcium is critical to both normal and pathological hearts. Chapter 2 suggests *mdx* mice exhibit calcium-dependent sheet dysfunction at base, leading us to hypothesize that the base handles calcium differently than the apex. We employed optical mapping to investigate calcium handling of *mdx* mouse hearts for the first time.

Optical mapping of calcium transients in ex vivo, viable, and intact heart (simply "optical mapping" hereafter) uses a camera to capture the time-varying fluorescence signals of calcium-sensitive dyes. Efimov's group pioneered the technique two decades ago (Efimov, Huang *et al*. 1994). The optical mapping technique is a powerful tool to investigate cardiac calcium transients in human, dog and mouse (Fedorov, Chang *et al*. 2010; Lang, Glukhov *et al*. 2011; Cheng, Lang *et al*. 2012). However, one needs to either open the chest or prepare an *ex vivo* Langendorff perfused heart to provide access the heart to optical cameras.

For interested readers, the best publication introducing the setup of optical mapping is on *The Journal of Visualized Experiments* (Lang, Sulkin *et al*. 2011), which is also from Efimov's lab. It utilizes online video streaming to explain the complex setup efficiently and clearly.

http://www.jove.com/video/3275/optical-mapping-action-potentials-calcium-transients-mouse

4.3. Method

4.3.1. Isolated heart preparation and calcium dye loading

Seven Langendorff-perfused hearts (Lang, Glukhov *et al*. 2011) from 16 month old mice were separated into two groups (*mdx*, N=4; and WT(C57BL/6), N=3). In brief, after anesthesia and heart excision, a short section of aorta was attached to a 21-gauge cannula. After cannulation, hearts were superfused and retrogradely perfused with oxygenated (95% O_2, 5% CO_2) constant-

temperature (37±1°C), modified Tyrode solution (in mmol/L: NaCl 128.2, KCl 4.7, NaH_2PO_4 1.19, $MgCl_2$ 1.05, $CaCl_2$ 1.3, $NaHCO_3$ 20.0, and glucose 11.1 (pH=7.3)) that was passed through a 5 μm filter (Millipore, Billerica, USA). Perfusion was performed using a peristaltic pump (Peri-Star, WPI, Sarasota, USA) under a constant aortic pressure of 60 – 80 mm Hg.

The isolated heart was pinned at the edge of ventricular apex to the Sylgard bottom of the chamber to prevent stream-induced movement. A small silicon drain tube was inserted into the left ventricle through the pulmonary vein, left atria, and tricuspid valve to prevent solution congestion and subsequent ischemia. A piece of small black tape was used to cover the atria to avoid fluorescence scattering from the atria. The excitation-contraction uncoupler Blebbistatin[8] (10 μM, Tocris Bioscience, USA) was used to prevent motion artifact on the action potential duration estimation. The heart was then stained with a calcium indicator (Rhod-2 AM, Invitrogen, Carlsbad, CA, 30μL of 1 mg/mL dimethyl sulfoxide, 1:1 mixed with Fluronic F127, Invitrogen, Carlsbad, CA in Tyrode's solution), for 5-7 minutes.

4.3.2. Optical imaging system

The excitation light was generated by a halogen lamp (Newport Oriel Instruments, Stratford, CT; SciMedia, Costa Mesa, CA) and passed through a heat filter, shutter, and excitation band-pass filter (520 ± 45 nm). A flexible light guide directed the band-pass filtered light onto the preparation. The optical mapping apparatus comprised an MiCAM Ultima-L CMOS camera (SciMedia, Costa Mesa, CA) with high spatial (100x100 pixels, 230±20 μm per pixel) and temporal (1,000-3,000 frames/sec) resolution. A band-pass filter (590±15 nm, Thorlabs, Newton, NJ) was fixed in front of the calcium-imaging camera.

[8] Blebbistatin will stop the muscle contraction, allowing motion free calcium transients recording.

4.3.3. Optical mapping protocols

After isolation and cannulation, motion suppression, and dye staining, prepared hearts were equilibrated for 5-10 min before imaging. The optical mapping signals were recorded sequentially under unloaded and stretched conditions. The unloaded condition was achieved by a pressure releasing silicon tube inserted into the LV chamber of the Langendorff heart preparation mentioned above. The stretched condition was achieved by inflating the LV chamber with Tyrode's solution to 80 mmHg pressure through the silicon tube inserted into the left ventricle. The perfusion pressure was increased from 60 to 100 mmHg to maintain the direction of the retrograde perfusion and the viability of the perfused heart. A steady-state restitution (S1-S1)(Lang, Glukhov *et al*. 2011) pacing protocol was applied under both conditions.

4.3.4. Optical mapping data processing

A custom-designed Matlab program was used to analyze the optical signals, which were filtered with a low-pass Butterworth filter at 256 Hz. Regional calcium dynamics were quantified in WT and *mdx* mouse ventricles (base vs. apex) under both unloaded and stretched conditions. Hand-drawn regions of interest were used to define basal (upper 1/3 area of left ventricle) vs. apical regions (lower 1/3 area of left ventricle). The calcium decay signal is not monoexponential and only the latter half of the decay signal could be fitted exponentially to derive the decay constant. Thus, both T50 and decay constant (Figure 19 A) are commonly used to characterize calcium relaxation kinetics (Giordano, He *et al*. 1997; Vassalle and Lin 2004; Zhu, Altschafl *et al*. 2005; Mukherjee, Apple *et al*. 2006; Taylor, Al-Saadi *et al*. 2006; Williams and Allen 2007; Sahoo and Kim do 2008; Sahoo, Kim *et al*. 2009; Chase and Orchard 2011; Mellor, Wendt *et al*.

2012). Specifically, Ca relaxation time from the calcium transient peak value to 50% relaxation (T50) was calculated to define the early calcium reuptake phase; and Ca decay constant was calculated using an exponential curve fitting program from the 50% calcium peak value to ful relaxation. Taken together, the T50 and the decay constant characterize the whole process of Ca reuptake-dependent relaxation.

4.4. Optical Mapping Results

4.4.1. Optical imaging reveals longer calcium decay time (T50) in 16 month old *mdx* mice

Under unloaded conditions, T50 was comparable between *mdx* and WT hearts. However, ventricular stretch elicited an approximately 25% increase in T50 (from 40 ± 2 ms to 51 ± 3 ms, $p < 0.05$, Figure 19) and approximately 50% increase of decay constant (from 25 ± 1 ms to 37 ± 1 ms, $p < 0.05$) at the base of *mdx* hearts, confirming abnormal calcium uptake in this region. Ventricular stretch, however, did not affect the T50 nor decay constant at the apex of *mdx* hearts, nor in the entire left ventricle of WT hearts, indicating a heterogeneous regional dependency on the development of abnormal calcium handling in *mdx*.

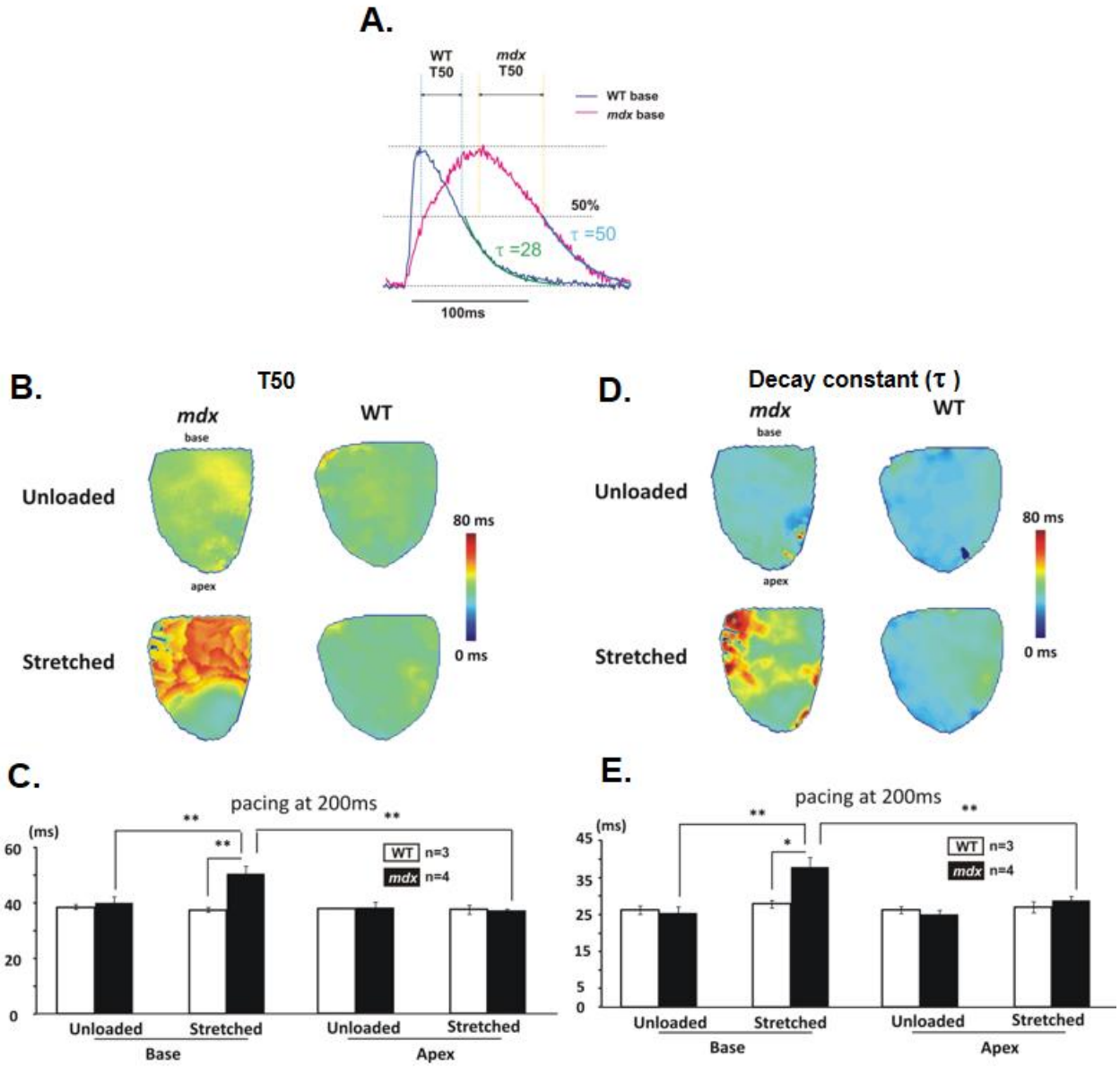

Figure 19. Calcium relaxation for *mdx* and WT. **A**, representative calcium transients at the base of a WT (blue line) and a *mdx* (red line) hearts. Signals were averaged from adjacent 25 CCD elements. Definitions of T50 and τ are illustrated. **B & C**, representative T50 and decay constant maps in *mdx* and a WT hearts under unloaded versus loaded (stretched) condition. **D & E**, under unloaded conditions, both T50 and decay constant were comparable between *mdx* and WT hearts. Ventricular stretch caused regional increases of T50 and decay constant at the base of *mdx* hearts. However, WT hearts exhibit similar T50 and decay constant. *, $p < 0.05$; **, $p < 0.01$.

4.4.2. 3 month old *mdx* mice exhibit normal calcium transients

Surprisingly, despite the fact that *mdx* mice lack dystrophin since embryo, the prolonged calcium transient abnormality did not exist in young mice (3 month old) whether stretched or not, while abnormal calcium transient exist at the base of old *mdx* mice (16 month old), only when stretched. Representative figures are shown in Figure 20.

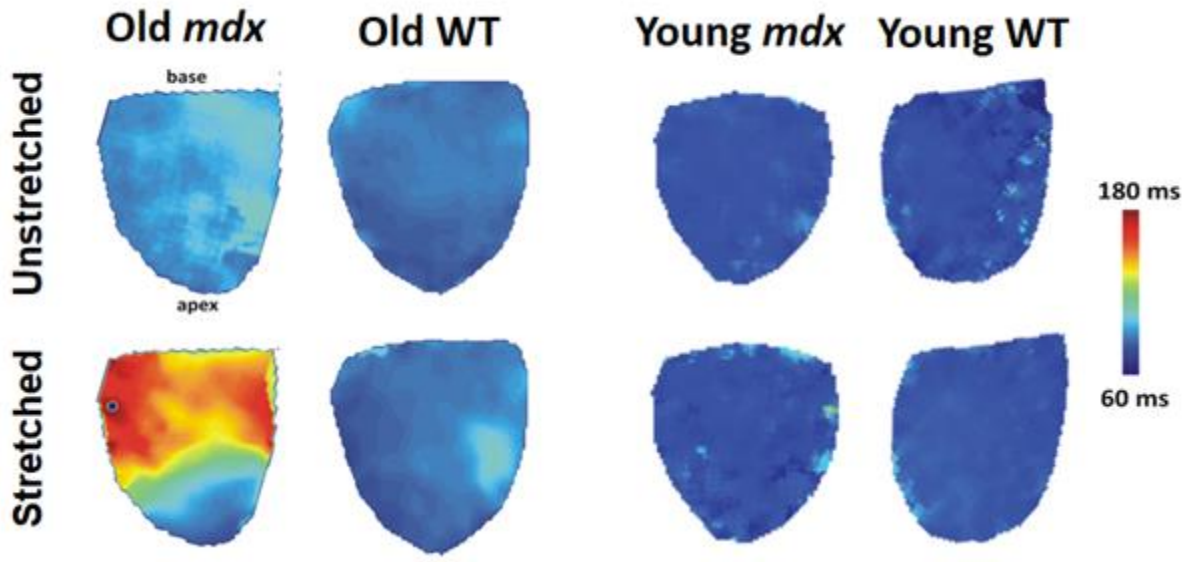

Figure 20. Calcium transient duration at 80% relaxation is only abnormal (red) in 16 month old *mdx* when stretched; but is normal (blue) when young or unstretched. T50 and decay constant exhibit the same pattern (not shown).

4.5. Discussion of regional abnormality at base

The prior recognition of stretch induced calcium mishandling in isolated *mdx* cardiomyocytes informs the present work (Williams and Allen 2007; Fanchaouy, Polakova *et al*. 2009). Specifically, mechanical stretch increases opening chance of stretch-activated channels (SAC) (Williams and Allen 2007) and induces transient membrane microruptures in *mdx* cardiomyocytes (Townsend, Blankinship *et al*. 2007; Townsend, Yasuda *et al*. 2007). The resultant leakage of extracellular calcium into the cytosol then compromises calcium clearance during relaxation and renders *mdx* cardiomyocytes vulnerable to stretch induced injury (Sapp,

Bobet *et al*. 1996). In this study of intact perfused hearts, we employed a stretch protocol to mimic cardiomyocyte activity under moderate strain regimes by inflating LV pressure to 80 mmHg, which is similar to that used for investigating fibrillation by several groups (Nazir and Lab 1996; Bode, Katchman *et al*. 2000; Zarse, Stellbrink *et al*. 2001; Eijsbouts, Majidi *et al*. 2003; Huang, Tai *et al*. 2003). Under the stretched condition, *mdx* hearts exhibited regional deficiency in calcium uptake, as evidenced by the prolonged T50 and decay time constant, at the base where the sheet functional defect was observed. Thus, our results illustrate a regional correspondence between abnormal diastolic sheet mechanics and disturbed calcium kinetics. Because sheet function is a key determinant of ventricular wall strain (Costa, Takayama *et al*. 1999; Usyk, Mazhari *et al*. 2000), and calcium mishandling in *mdx* cardiomyocytes is associated with cellular injury (Lynch 2004; Williams and Allen 2007; Prosser, Ward *et al*. 2011), the observed stretch-induced regional calcium mishandling in *mdx* hearts may be responsible in part for the local progression of diastolic sheet dysfunction.

4.6. Discussion of the perfusion condition in DTI and optic mapping

Results in Chapter 2 and 3 agree that abnormalities exist at the base of *mdx* hearts. However, Chapter 4 suggests the calcium transient abnormalities only when the left ventricle (LV) is *stretched* by 80 mmHg pressure. Why do I see abnormalities at base in Chapter 2 without stretching? Here is a possible explanation: In the DTI study, the LV was not vented, while in the optical mapping study, the LV was vented with a tube inserted in the LV through left atrium. I did not use the venting tube in DTI study, in order to avoid susceptibility artifacts and sliding motion-artifact of the tube. A venting tube in LV creates two surfaces of water/non-water materials and usually brings microbubbles into the LV. The surfaces and microbubbles both

generate unwanted susceptibility artifacts of MRI (Sakurai, Fujita *et al*. 1992). Furthermore, the tube tends to slide by few millimeter during the 1.5 hr long DTI study and generate motion artifacts. However, in optical mapping, all the signals were collected from the surface of a heart. Therefore, a tube in the LV does not affect optical imaging but does prevent the congestion of the perfusate and metabolism acidification in the LV, making a venting tube desirable for optical mapping study. In DTI, the metabolism acidification is less worrisome because the heart was arrested in diastole with the cardioplegic solution under 18 Celsius temperature which minimize the metabolism activity. In conclusion, in DTI study, all the hearts are not vented, therefore, the LV might be stretched by the perfusion pressure delivered through aorta valve incompetence or the Thebesian veins, during the 30~45 min long imaging setup time. In the future, a thin pressure transducer can be used to measure the pressure in the unvented LV for prolonged DTI acquisition to clarify this issue.

Chapter 5: Autophagy and Beneficial Effects of Rapamycin-nanoparticle

5.1. Acknowledgements

Experiment were designed by Bibee Kristine, Jon Marsh, Samuel Wickline and me. Richard Killing and I performed strength measurements. Sharron Yang and I performed autophagy nanoparticle treatments. Huiying Zhang and I performed histology of myocardium. Echocardiography ejection fraction were performed and processed by Dr. Jon Marsh. Western blots were performed by Dr. Kristine Bibee and Dr. James Ching.

5.2. Abstract

Current supportive therapy for DMD patients with corticosteroids results in a modest increase in strength as a consequence of a general reduction in inflammation, albeit with potential untoward long-term side effects and ultimate failure of the agent to maintain strength. Here, we demonstrate that rescuing defective autophagy in *mdx* mice, a model of DMD, with the use of rapamycin-loaded nanoparticles (RNP) induces a reproducible increase in both skeletal muscle strength and cardiac ejection fraction that is not achievable with conventional oral rapamycin delivery. *Rapamycin induces autophagy, or "self-eating", which is a cellular process responsible for recycling metabolites and eliminating toxic byproducts.* The resulted increase in physical performance occurs in both young and adult mice, and surprisingly even in aged wild-type mice. RNP treatment of old mdx mice increases autophagic activity with rapid beneficial consequences for improved LV function after only eight doses.

5.3. Introduction

As discussed earlier, DMD now is treated symptomatically with corticosteroids, resulting in a modest increase in strength albeit with expected and unavoidable side effects (Balaban, Matthews et al. 2005; Markham, Spicer et al. 2005; Moxley, Ashwal et al. 2005; Biggar, Harris et al. 2006). However, the cardiac phenotype has proven difficult to modify, and pursuit of combination therapies that might be steroid sparing remains an active area of research (van Deutekom, Janson et al. 2007; Kinali, Arechavala-Gomeza et al. 2009; Cirak, Arechavala-Gomeza et al. 2011; Goemans, Tulinius et al. 2011).

New pharmaceutical strategies other than steroid are desirable. A recent promising treatment target is the *autophagy pathway*, which is a cellular process responsible for recycling reusable products of metabolism and/or efficient elimination of toxic byproducts (Kundu and Thompson 2008). Indeed, rapamycin, a known inducer of autophagy, was reported by Eghtesad et al. (Eghtesad, Jhunjhunwala et al. 2011) in 6-week-old *mdx* mice to improve diaphragm muscle histopathology. Protein restriction has been shown to activate autophagy in 16-week-old mdx leading to enhanced grip strength (De Palma, Morisi et al. 2012). Recent work by Pauly et al. has demonstrated that autophagy induction in the diaphragm of 6-week-old *mdx* animals by daily intraperitoneal injections of an AMP-activated protein kinase agonist also promotes clearance of defective mitochondria and improves diaphragm strength (Pauly, Daussin et al. 2012). However, the potential benefits of enhancing autophagy in multiple muscle groups with the use of clinically practicable therapeutic agents that might elicit rapid and repeatable responses in *both* global physical performance and cardiac functionality in vivo over a broad range of ages (e.g., ≥16 months) have not been examined.

Rapamycin, an immune-suppressing macrolide typically used to prevent organ transplant rejection and as an anti-inflammatory agent to prevent angioplasty restenosis (Vilquin, Asselin et al. 1995; Thomson, Turnquist et al. 2009; Adelman), is known to induce autophagy, thereby inciting a cell survival program that enables useful recycling of amino acids via non-specific degradation of long-lived proteins and dysfunctional organelles (Shigemitsu, Tsujishita et al. 1999). By binding to the mammalian target of rapamycin complex 1 (mTORC1), rapamycin blocks proliferative signaling (Wullschleger, Loewith et al. 2006). Paradoxically, blocking mTORC1 with rapamycin might be expected to exert *deleterious* effects on protein synthesis, muscle fiber regeneration, and cell growth in *mdx* mice, all of which might be expected to maintain strength. However, if autophagy is fundamentally defective in DMD/*mdx* and can be shown to reverse weakness and cardiac dysfunction, and if a method for effective delivery of clinically approved doses of rapamycin to muscle tissues that might enhance autophagy and improve endurance can be designed, then a compelling mechanistic link between disturbed autophagy and progressive deterioration of global physical strength and contractile performance in vivo would be suggested.

Nanoparticle therapeutics for treating cancer and other pathologies are now undergoing clinical trials in multiple drug combinations (Etheridge, Campbell et al. 2013), but heretofore have not been evaluated in neuromuscular diseases. The potential advantage conferred by such agents is their high local accumulation at sites of disease in concert with the use of lower serum levels of free drug that would limit unwanted off targeted side effects, as has been shown for Doxil™ and Abraxane™ in cancer for example. Accordingly, we compared both an oral preparation of rapamycin and an intravenous nanoparticle-based formulation of rapamycin (RNP) for ability to improve a clinically significant global performance factor related to endurance and

grip strength, with the use of validated methods that are translationally relevant and highly correlated with mortality in the *mdx* model (Keeling, Golumbek et al. 2007). Furthermore, we measured autophagic responses to rapamycin nanoparticles in skeletal muscle tissues for correlation with grip strength metrics (designed and performed by Jon Marsh and Kristine Bibee). Finally, we delineated the effects of these agents on cardiac function in aged *mdx* and wild-type mice.

5.4. Methods

5.4.1. Reagents

All chemicals were purchased from Sigma-Aldrich, Inc. (St. Louis, MO, USA) unless otherwise specified.

5.4.2. Nanoparticle formulation

The perfluorocarbon nanoparticle emulsions without or with rapamycin (at a concentration of 0.275 mol%) were prepared as previously described (Cyrus, Zhang et al. 2008). In general the sizes of the PFC NP range between ~160-240 nm (Wickline, Neubauer et al. 2006; Wickline, Mason et al. 2010). As an example, batch MS1-92b exhibited a diameter of 184.7 nm, polydispersity 0.120, and zeta potential -15.31 mV. We note from prior experience that drug loading has little effect on the size but may affect zeta potential depending on the exact composition and charge of the loaded moiety (Soman, Lanza et al. 2008; Soman, Baldwin et al. 2009). An additional, dual-fluorophore emulsion was formulated to verify delivery of both nanoparticles and rapamycin to skeletal muscle. The emulsion lipid moiety incorporated rhodamine B (Avanti Polar Lipids, Alabaster, AL, USA), and the rapamycin was conjugated with a near-infrared (IR) fluorescent dye (Cy7.5, Lumiprobe Corporation, Hallandale Beach, FL) before formulation into the nanoparticles. Perfluorocarbon nanoparticles are exceedingly stable in blood as they were originally developed as a blood substitute (Flaim 1994). The stability of rapamycin incorporated into nanoparticles has been reported previously (Cyrus, Zhang et al.

2008). Drug release kinetics against an infinite sink of releasing medium in vitro verified retention of 97% of nanoparticle rapamycin over three days.

5.4.3. Animal studies

Strength studies: Male *mdx* mice (strain C57BL/10ScSn-Dmd^{mdx}/J) and age-matched controls (strain C57BL/10SnJ) were purchased from The Jackson Laboratory (Bar Harbor, ME, USA). All mice were housed in the same animal facility and cared for under approval by Washington University's animal study committee. Starting at age 14 weeks, mice were injected twice weekly for four weeks with plain nanoparticles (n=18 for *mdx*, n=4 for control) or nanoparticles loaded with rapamycin (n=16 for *mdx*, n=5 for wild-type). Dosage was 1 mL emulsion/kg body mass, injected via lateral tail vein resulting in approximately 0.002 mg rapamycin per animal per treatment. An additional set of *mdx* (n=8) mice was housed in an AAALAC-approved facility until they were 17 months of age, at which point they received 4 weeks of RNP treatment as described above.

Separate groups were utilized for oral rapamycin therapy. For these animals, rapamycin was solubilized in grain alcohol and was delivered in a mixture of dextrose and water twice weekly for four weeks via micropipette gavage, typically 40–50 µL per mouse. There were three treatment groups: *mdx* mice given rapamycin (n=6); control mice given rapamycin (n=6); and *mdx* mice given placebo (n=6).

Treatment effectiveness was determined by measuring forelimb grip strength within one week before beginning each treatment regimen, and subsequently within one week after treatment completion. Strength testing was performed in blinded fashion by an experienced technician as previously described by our group (Keeling, Golumbek et al. 2007) and by others who have used this standardized test of physical fitness and endurance. Strength testing was

performed using a grip meter attached to a force transducer (E-DF 002 Digital Force Gauge, Chatillon Force Measurement Systems, Largo, FL, USA). The tests relied on the animal's instinct to grab hold as it was pulled backward. Each mouse was grasped by the tail and encouraged to grab a trapeze bar attached to the force transducer using its forelimbs. The mouse was then pulled away and the peak force was recorded on a digital display. This procedure was repeated five times in a row for each animal. The three highest readings were averaged and normalized by the animal's weight to give the strength score.

Rapamycin nanoparticle drug holiday studies: To determine if the effects of RNP on grip strength were reproducible in individual animals, a cohort (n=7 for *mdx*/no drug, n=8 for *mdx*/rapamycin, n=4 for wild-type/no drug, and n=5 for wild-type/rapamycin) of the originally treated 14-week-old mice was maintained off drug therapy over the span of 18-34 weeks of age to allow washout of the RNP effect. The same one month RNP treatment and grip strength testing regimen was then repeated for 1 month starting at age 34 wks.

Cardiac studies: A cohort of 17-month old *mdx* mice received either RNP (n=9) i.v. via eight tail vein injections (1.5 mL/kg/dose), 2x/week over four weeks to deliver the same cumulative amount of rapamycin as for the other studies above or no treatment (n=7). Wild-type mice of the same age were used as controls (n=6 for RNP, n=8 for no treatment). The mice were lightly anesthetized for cardiac ultrasonography with isoflurane and placed supine for examination with a 16 MHz array (Spark, Ardent Sound, Inc., Mesa, AZ, USA). Prior to imaging, the thorax of each animal was shaved and depilated. Animal body temperature was maintained with a heated water blanket and thermistor-controlled heating lamp. Heated ultrasound coupling gel was liberally applied to the shaved area. Waveforms were sampled at the system's clock frequency (66.67 MHz) using a 12-bit digitizer (GaGe Compuscope 12400, DynamicSignals LLC,

Lockport, IL, USA). Two hundred frames of cardiac data were acquired for each view at a frame rate of 152 Hz, with each frame consisting of 128 A-lines (2048 sampled points/line). Each loop thus consisted of between 8 and 12 heart cycles. Radiofrequency (RF) data were converted to scaled image data using custom plugins written for the open-source image processing software ImageJ (Rasband, W.S., U. S. National Institutes of Health, Bethesda, MD, USA, http://imagej.nih.gov/ij/, 1997-2013). Backscattered ultrasound energy was mapped to grayscale by taking the log of the sum of the squares of the digitized voltage values in a center-weighted moving window. The resulting image loops were scaled to a resolution of 0.05 mm/pixel. Left ventricular ejection fraction (LVEF) was computed using ImageJ by manually tracing the ventricular endocardium border at systole and diastole in the short-axis (SAX) view for each beat and by recording the area region of interest (ROI). Ventricular length was computed from the long-axis (LAX) view by determining the length of a line manually drawn from the apex endocardium to the aortic valve plane. Left ventricular volume at systole (or diastole) was estimated by computing the volume of an ellipsoid having a circular cross-section equal to the mean systolic (or diastolic) ROI area and length equal to the mean systolic (or diastolic) measured ventricular length. LVEF was then computed as the ratio of the difference in volume of this ellipsoid between diastole and systole, and the diastolic volume.

5.4.4. Histology

Fibrosis imaging was performed in the diaphragm by analyzing trichrome stained (Masson), formalin-fixed sections (8-µm thickness) with a stain kit (HT-15-1KT, Sigma-Aldrich) and in the heart with picrosirius red stains per standard protocol (Dolber and Spach 1987). Color light microscope images of collagen were acquired from five randomly selected fields for each

diaphragm section at 200X with an Olympus BX61 microscope and F-View camera (Olympus America Inc., 3500 Corporate Parkway, Center Valley, PA, USA). Similar assessments were performed for basal heart sections from 5 treated and 5 untreated *mdx*. Custom software (written as a plugin for ImageJ) was used to quantify the area of each image associated with collagen-labeled pixels relative to the area of each image associated with tissue of any type.

For fluorescence histologic imaging, 14-week old *mdx* mice were given intravenous injections (1 mL/kg) of dual-labeled fluorescent nanoparticles and sacrificed 4 hours post-injection following systemic saline perfusion to wash out any residual circulating nanoparticles. Nanoparticle and/or rapamycin tissue distribution was demonstrated in the biceps, diaphragm, gluteus, and myocardium of mice injected with fluorophore-loaded emulsions in excised and frozen (OCT medium: Tissue-Tek, Sakura Finetek, Torrance, CA, USA) or paraffin-embedded tissues. Sectioning (8-µm) was performed on 10 consecutive slides from each tissue sample (a total of 60 slides were prepared), and random sections were chosen by a blinded observer for fluorescence microscopy. Adjacent slides were saved for H&E. Multiple images were acquired from each section with an Olympus BX51 fluorescence microscope image system, using an Infinity3 camera (Lumenera Corporation, Ottawa, Ontario, Canada) for optical image recording and digitization, and F-View II B&W CCD camera for fluorescent images.

Tissue nanoparticle biodistribution

^{19}F perfluorocarbon-core nanoparticles were administered to 14 *mdx* mice (18 weeks old) by tail vein injection; and tissue and organ harvesting conducted at either 2, 12, or 24 hours. Tissues harvested for measurement of nanoparticle concentrations were acquired after in situ

perfusion fixation of the mouse that was initiated by cardiac puncture and flow-through of buffer solution until venous effluent was clear (~10 min). This washout procedure ensured that blood contamination was not a factor in the estimation of tissue nanoparticle content. We also note that the tissue distributions and clearances for similar particles are not affected by drug loading and have been reported before for mice and rabbits (Hu 2007; Soman, Lanza et al. 2008; Soman, Baldwin et al. 2009). The specimens were blotted dry, weighed, fixed in formalin, and then subjected to fluorine spectroscopy with the use of an 11.7T Varian MRI/MRS scanner and a custom-built single-turn solenoid coil. ^{19}F spectra signal from each specimen and from a standard of perfluoro-15-crown-5 ether were obtained via non-localized 90-FID spectroscopy (2.5-s pulse repetition time TR, and 128, 256, or 512 signal averages NT). The unique and quantitative fluorine signature was expressed as total tissue fluorine content per gram. This methodology fortunately avoids the necessity for extraction of the target compound (perfluorocarbon in this case) with its attendant inefficiencies, since the total amount of ^{19}F signal in the entire unprocessed tissue can be registered nondestructively. Because there is a direct and linear relationship between the ^{19}F signal and the nanoparticle concentration, the analytical method yields essentially the nanoparticle concentration per unit tissue mass (Morawski, Winter et al. 2004).

Creatine Kinase

Blood was obtained by left ventricular cardiocentesis, and serum extracted by centrifugation. Serum creatine kinase (CK) levels were measured spectrophotometrically with a Vitros DT60 dry reagent chemistry analyzer (OrthoClinical Diagnostics, Raritan, NJ, USA).

Autophagy and autophagic flux measurements

Muscle tissues were extracted from the *mdx* mice and homogenized in 0.5 mL of RIPA buffer with 1-mM PMSF, Complete Protease Inhibitor Cocktail (Roche, Indianapolis, IN, USA), and Phosphatase Inhibitor Cocktail (Roche) using a glass grinding tube. The tissue homogenates were centrifuged at 10,000xg for 10 min at 4℃ and the supernatant was stored at -80℃.

Proteins in tissue homogenates were resolved on a NuPAGE Novex 4-12% Bis-Tris Gel (Invitrogen, Carlsbad, CA, USA), transferred to 0.2 μM nitrocellulose, blocked in 5.0% milk/TBS-T and incubated with the following primary antibodies: rabbit anti-pS6 (1:1000, Cell Signaling 4857, Boston, MA, USA), rabbit anti-S6 (1:1000, Cell Signaling 2217), rabbit anti-LC3B (1:2000, Sigma-Aldrich), rabbit anti-Beclin1 (1:1000, Cell Signaling), goat anti-actin (Santa Cruz Biotechnology, Inc., Santa Cruz, CA, USA). Corresponding secondary antibodies were used at 1:5000. Protein bands were visualized using either ECL Western Blotting Substrate (Pierce 32106, Rockford, IL, USA) or Super Signal West Femto Maximum Sensitivity Substrate (Pierce 34095). Western blot image was used to calculate relative protein expression using densitometry with ImageJ. Values were normalized to myosin loading control and reported as fold change compared to the control, non-treated sample.

To illustrate how this approach might apply to actual primary human cells and be potentially generalizable, tumor cells (HIM3 line from the Washington University HAMLET Core) were derived from a biopsy specimen that was procured from a triple negative primary breast tumor and were passaged through immunodeficient animals in a method described previously (Ding, Ellis et al.). Cells were maintained in McCoy's 5A media (Invitrogen, Carlsbad, CA) supplemented with 10% FBS (Sigma, St. Louis, MO) and penicillin/streptomycin (Invitrogen, Carlsbad, CA) in a 37^{o} C humidified tissue culture incubator with 5% carbon dioxide. Lentivirus containing the LC3-GFP fusion was obtained from C. Weihl (Washington University, St. Louis, MO). The cells were transfected using a standard spinfection method with protamine sulfate. After recovery, the cells were sorted on a BD Aria II High Speed Cell Sorter three times with one-week recovery periods between each sort. The stable cell lines were then treated for 24 hours with DMSO (vehicle for rapamycin), rapamycin (100nM), nanoparticles ($3.09x10^{10}$ particles/mL), or rapamycin-nanoparticles ($3.09x10^{10}$ particles/mL = 100nM rapamycin). After treatment, the cells were washed, fixed with paraformadehyde and imaged with a Zeiss LSM510

microscope. GFP-positive puncta were counted by a blinded observer. Other treated cells were prepared for transmission electron microscopy per standard protocols

For *in vivo* autophagic flux assessment, we utilized a recently developed autophagic flux assay that measures turnover of LC3B-II in mouse skeletal muscle by comparing mice treated with and without a potent blocker of autophagic protein degradation (colchicine) (Ju, Miller et al.). Colchicine was administered over 48 hours in two doses (0.4 mg/kg) delivered intraperitoneally, followed by diaphragm or heart tissue collection. Tissue homogenates were probed as above.

A separate set of experiments using oral prednisolone as the active agent was conducted to delineate potential mechanistic similarities between RNP and steroids with respect to their effects on autophagy for an agent that is known to improve strength experimentally and in patients. Four *mdx* mice were treated with oral prednisolone and four control *mdx* were treated with vehicle for 42 weeks (starting at age 4 weeks), after which muscle tissues [tibialis anterior (TA)] were extracted for autophagy measurements as above.

Statistics

Statistics were generated as noted below for selected ANOVA, t-test, and groupwise comparison procedures using SAS software (SAS Institute, Cary, NC, USA) and the open-source statistical package R (R Foundation for Statistical Computing, Vienna, Austria, http://www.R-project.org).

5.5. Results

5.5.1. Rapid enhancement of global physical performance with RNP

None of the fourteen-week-old *mdx* and wild-type mice treated with nanoparticles demonstrated apparent adverse effects from the treatment at any time point and all animals

completed the study. Figure 21a shows that grip strength increased significantly when RNP were employed as therapy (30% absolute increase in mean strength of group). Unexpectedly, when nanoparticles (NP) alone were employed as therapy, grip strength exhibited a trend toward a modest strength increase (Figure 21a) of 8%.

To determine whether the grip strength improvement was due to the drug alone, animals were treated with oral rapamycin administered at 10x the equivalent nanoparticle i.v. dose to account for an expected 10% oral absorption rate (Napoli, Wang et al. 1997; Crowe, Bruelisauer et al. 1999; Stepkowski 2003; O'Reilly, McSheehy et al.). As shown in Figure 21a, the oral rapamycin did not improve grip strength. Age-matched wild-type mice exhibited no significant increase in grip strength when treated with rapamycin-loaded nanoparticles or oral rapamycin (Figure 21b).

Figure 21c shows that over this washout interval, strength declined as anticipated. After the repeat dosing of i.v. RNP, grip strength once again improved in the older *mdx* animals ($p=0.008$, linear contrast model). No significant trend was observed in wild-type mice (Figure 21d). Interestingly, RNP treatment of a cohort of 17-month-old *mdx* ($n=8$) mice treated for a month in similar fashion revealed a more muted effect on strength (Figure 22a: $p = 0.201$, two-tailed paired t-test).

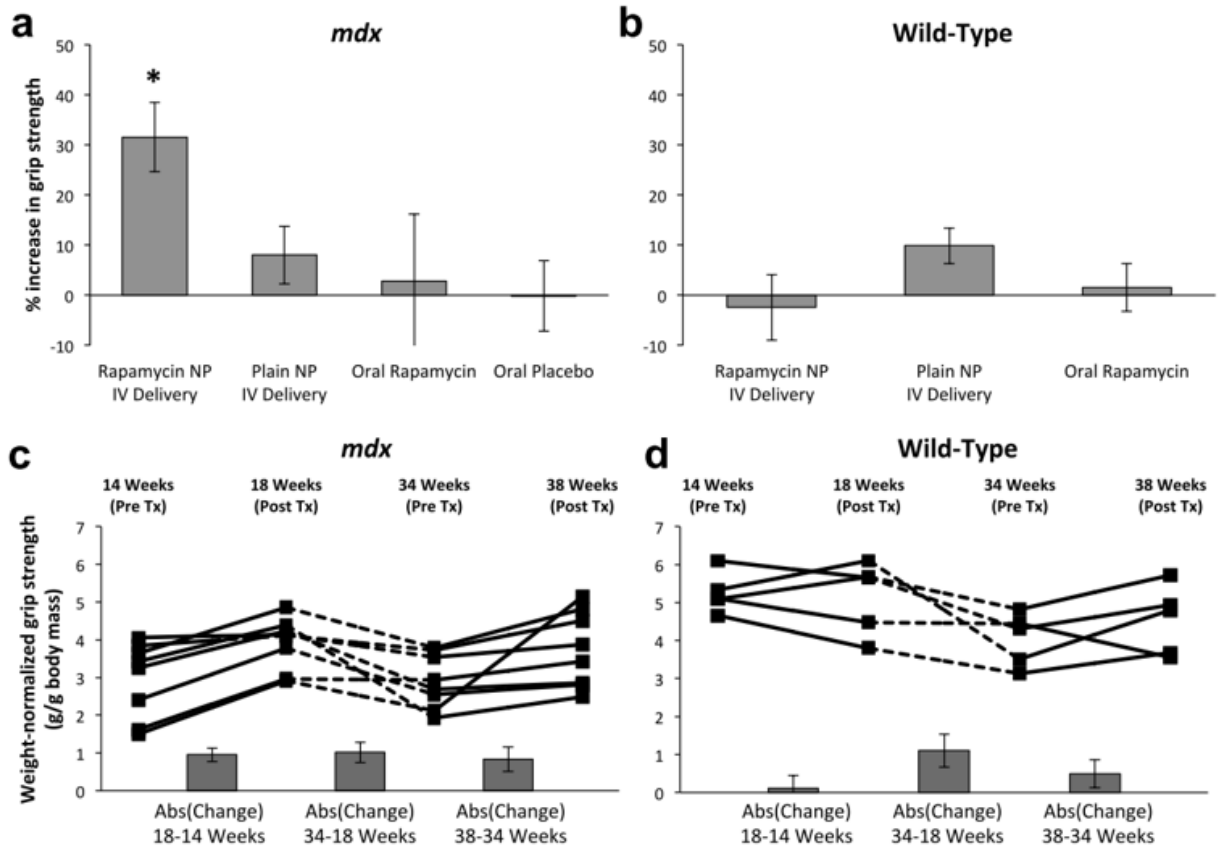

Figure 21. Rapamycin-loaded nanoparticle treatment improves strength in *mdx* mice.

a) Four weeks of treatment with rapamycin-loaded nanoparticles (RNP) delivered intravenously significantly increased mean weight-normalized grip strength in 14-week old *mdx* animals (n=16) vs. groups given plain nanoparticles (NP) IV (n=18), equivalent oral doses of rapamycin (n=6), or oral placebo (n=6) (p=0.012, p=0.027, and p=0.016, respectively, using Fisher's protected least significant difference at 5% significance level). b) No significant difference in mean strength was observed for age-matched wild-type mice given either NP (n=4) or RNP intravenously (n=5) or oral rapamycin (n=6). c) The increase in weight-normalized strength in a subset of *mdx* mice (n=8) treated with IV RNP occurred in both young (14-18 wk) and old (34-38 wk) animals (p=0.008 using a linear contrast model comparing pre- to post-treatment differences at a 5% significance level). Absolute values of the mean change in strength between time points are shown in columns below trend data. d) Wild-type mice (n=5) given a similar longitudinal treatment and drug-holiday exhibited no significant difference between pre- and post-treatment strength (p=0.598). All bar graphs show mean values +/- s.e.m.

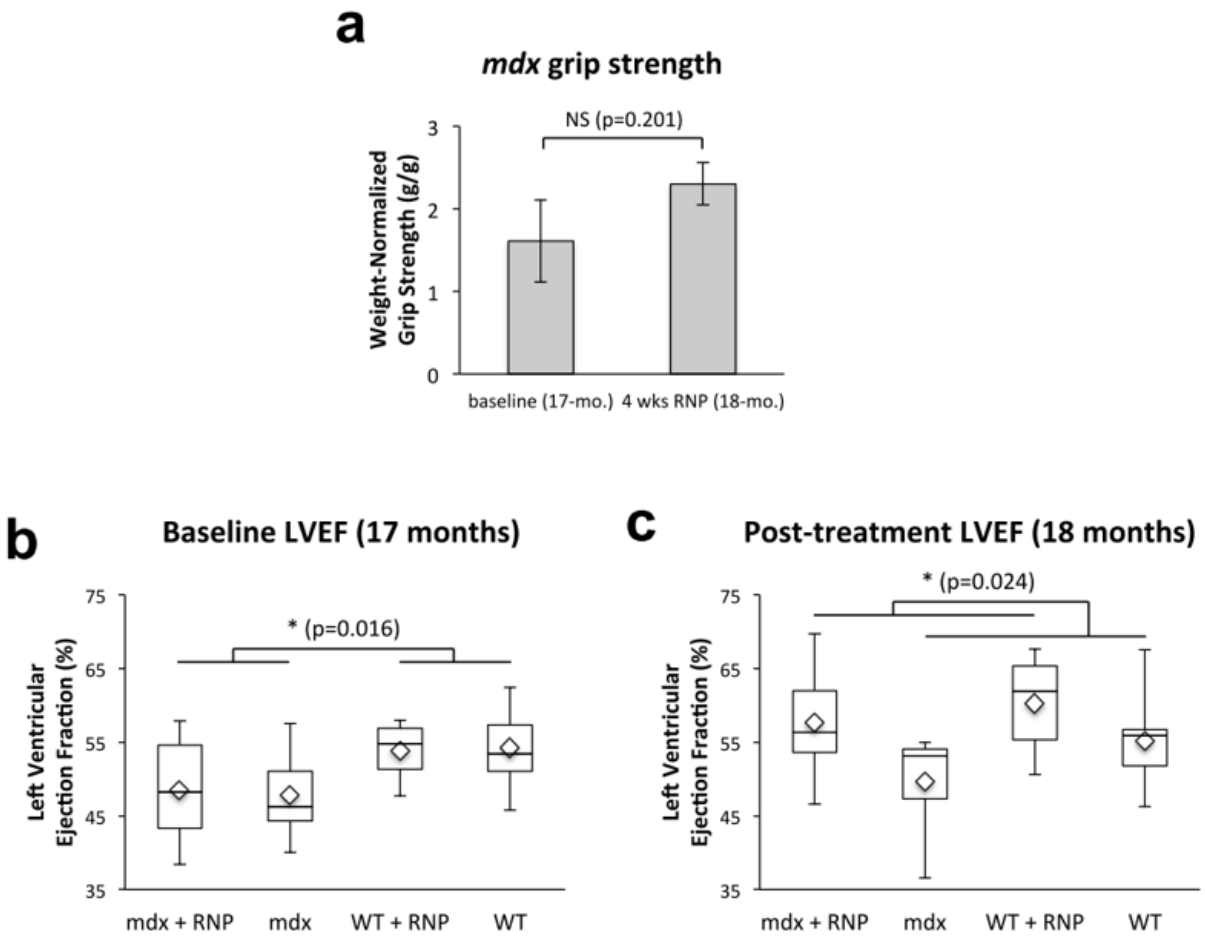

Figure 22. Aged *mdx* mice show muted responses in grip strength after treatment with RNP, but marked improvement in cardiac function commensurate with wild-type animals

a) Four weeks of treatment of 17-month-old *mdx* (n=8) yielded no significant increase in grip strength (p=0.201, two-tailed paired t-test). **b)** LVEF in wild-type mice is greater than *mdx* before treatment (p=0.016), as expected. **c)** Cardiac function significantly improved after RNP therapy, irrespective of animal type (16% difference for mdx and 9% difference for WT; p=0.024).

5.5.2. Rapid enhancement of cardiac performance with RPN in aged mice

In the cohort of 17 month-old mdx and wild-type mice, one month of biweekly RNP versus no treatment yielded two compelling findings: 1) LVEF in *mdx* was significantly lower than that of wild-type mice before treatment ($p=0.016$) as expected (Figure 22b); and 2) LV ejection fraction for RNP treated mice was 57 ± 2.9 %, and approximately 16% higher than that of none-treated mdx mice (49 ± 2.5 %; $p=0.024$).

5.5.3. Nanoparticle tissue distribution

Results of fluorescence microscopy of fluorophore-labeled rapamycin and fluorophore-labeled lipids contained in the outer nanoparticle shell are shown in Figure 23. It is clear that the particles penetrate heart tissue to deliver rapamycin locally (Figure 23). The labeled rapamycin appears to achieve an even greater penetration into tissues than do the nanoparticles, arguing for some degree of local rapamycin release and more complete passive diffusion. We note that the use of the near-IR fluorophore avoids the problem of background autofluorescence, thereby permitting confident assessment of the more diffuse penetration of rapamycin into muscle tissues beyond the loci of nanoparticle deposition. The observation of diffuse rapamycin penetration into tissues beyond the nanoparticle carriers (Figure 23) was further supported by analyzing both blank slides and unstained muscle tissue specimens that were microscopically digitized at the same settings to rule out background signals of any type that might have overlapped with the rapamycin signal, and none were observed (data not shown).

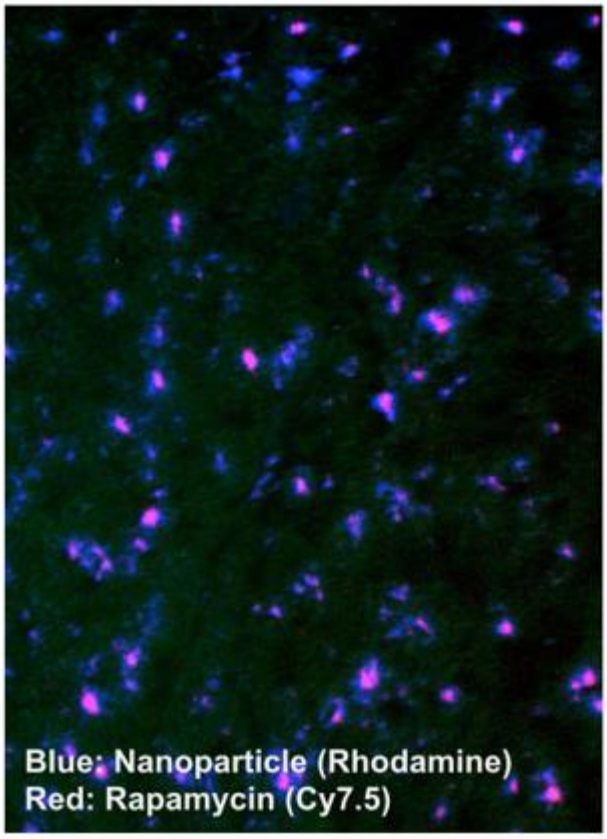

Figure 23. Nanoparticles and rapamycin are delivered to cardiac muscle in *mdx* animals.

Nanoparticle lipid (rhodamine, displayed as blue) and rapamycin (Cy7.5, labeled as red) are colocalized in *mdx* cardiac tissue.

5.5.4. Effects on skeletal and cardiac mTOR and autophagic processes

To further demonstrate that the drug reaches muscle tissue and then acts on a known target, lysates from the muscle were probed for phosphorylated S6. S6 is downstream of mTORC1, so that blocking mTORC1 with rapamycin should cause a decrease in pS6 levels. Indeed, in diaphragm, triceps, biceps, and gluteus, S6 levels were decreased in *mdx* animals treated with rapamycin-loaded nanoparticles when compared to mice treated with nanoparticles alone (Figure 24a). Interestingly, the nanoparticles themselves caused a modest *increase* in pS6 levels when compared with saline treated animals. Thus, the particle itself may induce signaling through mTORC1, but adding rapamycin to the particle then decreases the level of signaling, yet does not cause a return to baseline levels.

Our data confirm that the *mdx* mouse harbors a defect in autophagy in muscle tissues, as there is an increase in p62 protein (Figure 24b) with no difference in p62 transcription (Figure 24c). This expression pattern suggests that p62 is not being consumed in the process of autophagy in the *mdx* animal as it is in the wild-type animals. Further, BNIP3, a protein that is known to trigger autophagy, is found at lower levels in *mdx* animals when compared to wild-type (Figure 24b, c). Additional in vivo confirmation of the effects of rapamycin nanoparticles on autophagy revealed that basal autophagic flux was diminished in *mdx* mouse heart as demonstrated by comparing the change in LC3II protein levels with and without colchicine treatment (Figure 24d).

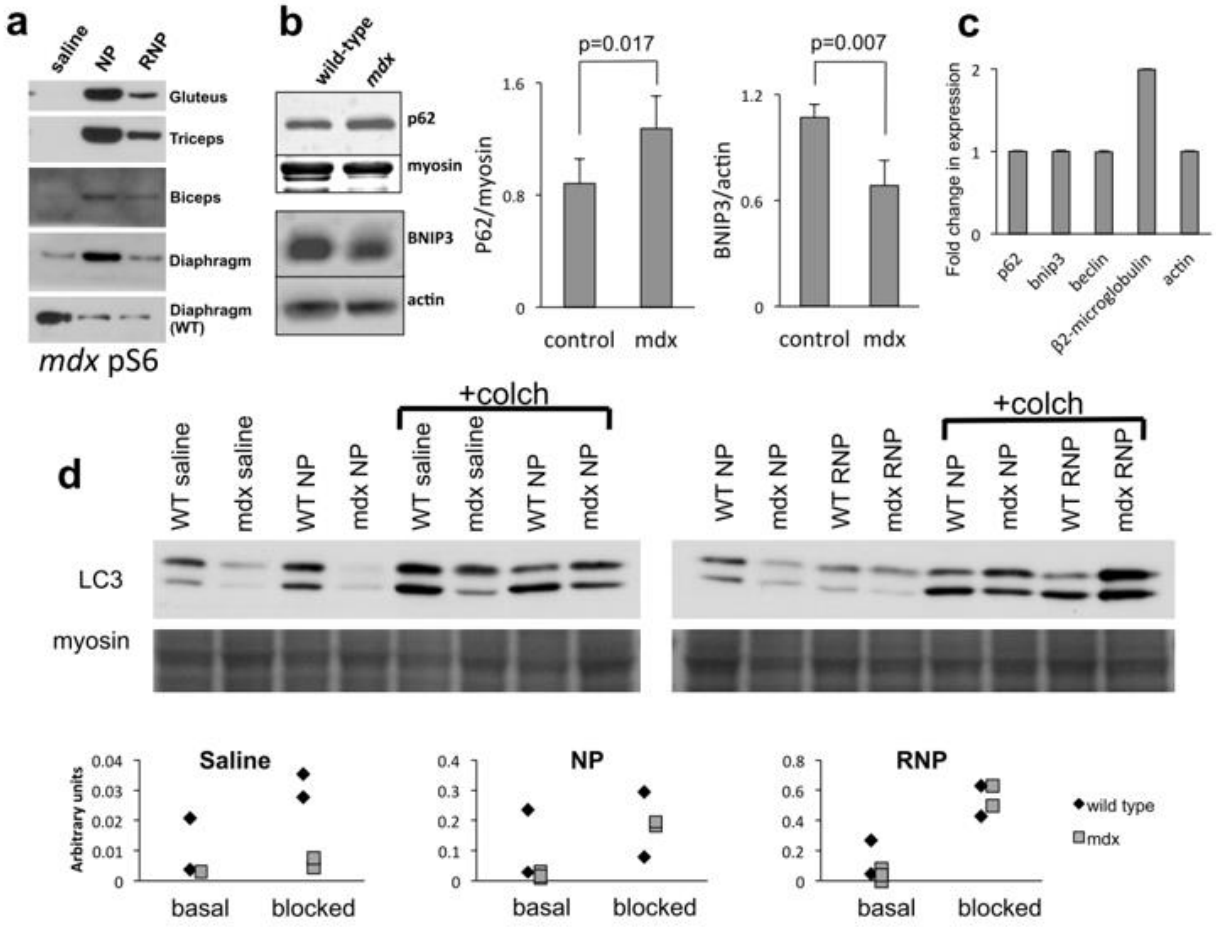

Figure 24. *mdx* animals exhibit a defect in autophagy that is restored by nanoparticle treatment.

a) RNP cause a decrease in S6 levels in *mdx* animals when compared to NP treatment. However, compared to saline treatment, the NP increased S6 phosphorylation in all muscle groups tested, a trend not observed in the muscles from wild-type animals. **b)** Proteins were extracted from *mdx* and age-matched control animal muscle. Western blot analysis for p62 (n=5 per group) and BNIP3 (n=3 per group) reveal a defect in autophagy as *mdx* animals exhibited higher levels of p62 and lower BNIP3 when compared to wild-type (Student's t-test at 5% significance level). Myosin was used as the loading control. **c)** RNA was isolated from the tibialis anterior muscle of age matched *mdx* (n=5) and control mice (n=3). QPCR was performed and normalized to GAPDH. Graph demonstrates fold change in the following transcripts vs. control: there was no change in p62, BNIP3 or beclin. Beta 2 microglobin is increased as expected, because it is part of MHCI, which is known to be upregulated in *mdx* muscle. Actin levels (normal) serve as an internal control. **d)** Representative Western blots demonstrate that both nanoparticle (NP) and rapamycin-loaded nanoparticles (RNP) increase the levels of LC3B-II in the *mdx* animal, whereas saline treated animals exhibit a low level of LC3B-II expression, even when blocked with colchicine. Scatter plots show results from individual animals.

Additional probing of the tibialis anterior (TA) and heart muscle in the 17 month-old mice treated for 1 month with RNP was performed to assess the autophagic responses. Figure 25a illustrates significant effects of RNP in TA on p62 (decrease), BNIP3 (increase), and LC3II (increase). Figure 25b confirms that RNP also enhanced autophagy in the heart in the same manner. Figure 25c shows autophagic responses to prednisolone in the TA of mdx mice, where changes in p62, BNIP3, and LC3II are all similar in direction and magnitude to those reported above for RNP, further suggesting that autophagy responses to either RNP or steroids in the mdx represents a likely candidate mechanism for the observed augmentation of muscle strength and cardiac function. Taken together, these data point to a rapid and widespread induction of autophagy in diverse muscle tissues after RNP treatment.

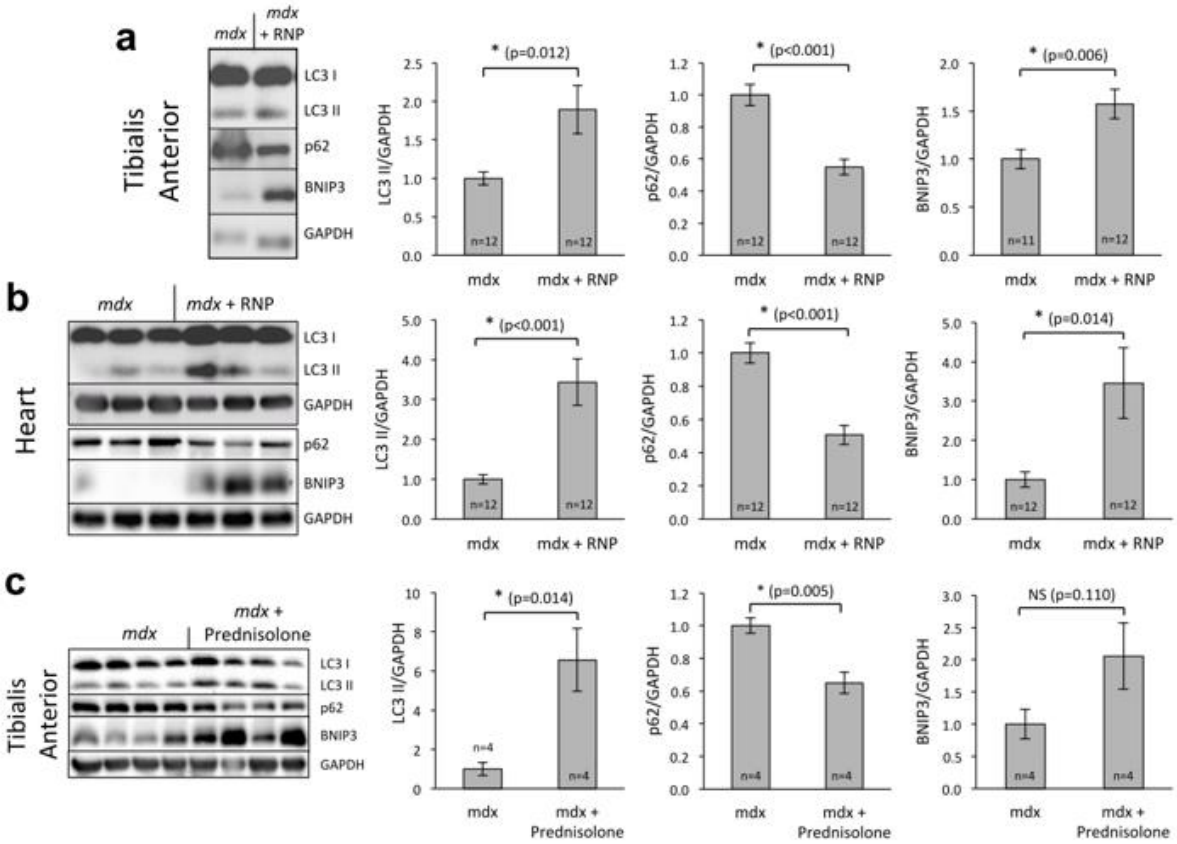

Figure 25. Rapamycin nanoparticles alter autophagic biomarkers in heart and skeletal muscle of *mdx* mice similar to that after steroid therapy.

a) Tibialis anterior (TA) muscle in 17-month-old *mdx* mice treated for 1 month with RNP exhibited significant effects of RNP on p62 (decrease), BNIP3 (increase), and LC3II (increase). b) Cardiac data confirms that RNP also enhance autophagy in the heart in the same manner. c) Young *mdx* mice given 42 weeks of steroid therapy show similar autophagic responses in the TA muscle.

5.5.5. Tissue structural responses

The amount of collagen within skeletal and cardiac muscles (Figure 26a-d) was not different between the treatment groups ($p=0.900$ for diaphragm using mixed model nested ANOVA, $p=0.664$ for heart using unpaired two-tailed t-test). Figure 26e demonstrates no significant difference between creatine kinase (CK) levels in saline treated animals when compared to those treated with NP or RNP ($p=0.682$, one-way ANOVA). From these data, it does not appear that the nanoparticles are exerting their beneficial effect on strength by altering the turnover of myocytes or the replacement of myocytes with collagen in the short term, as might be expected after only 8 doses of therapy.

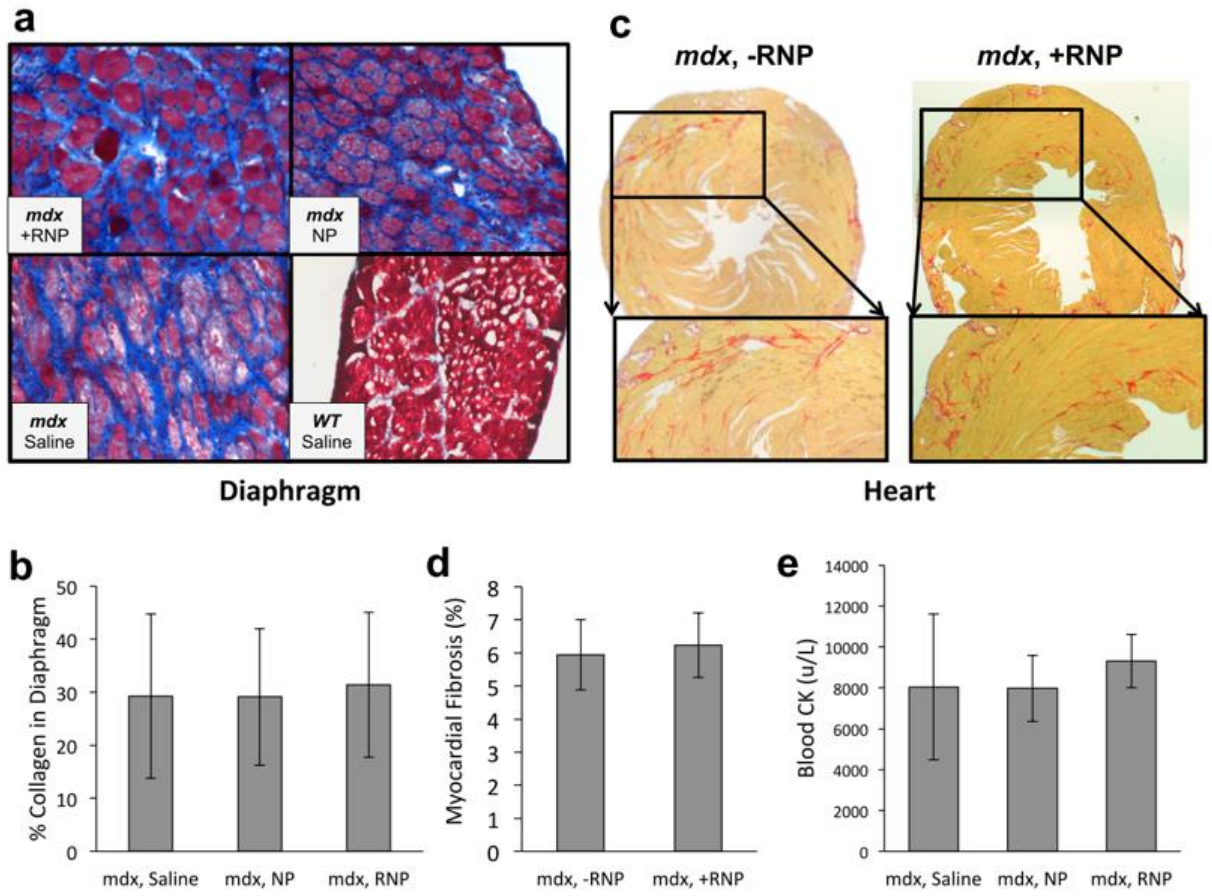

Figure 26. Intravenously injected nanoparticles do not affect short-term muscle cell destruction or fibrosis.

a) Masson trichrome stains performed on diaphragm sections and visualized with light microscopy (200x) showed increased fibrosis (blue) for *mdx* animals relative to WT. **b)** No significant difference occurred over the short 4 week test interval in *mdx* collagen levels after treatment with either rapamycin-loaded nanoparticles, plain nanoparticles, or saline (mixed model nested ANOVA, p=0.90). c) Picrosirius red stains of *mdx* mice show diffuse heterogeneous fibrosis with d) no significant difference (p=0.664) when treated with RNP. e) Serum creatine kinase levels for *mdx* mice exhibited no significant difference after treatment with either RNP, NP, or saline (ANOVA, p=0.71). All bar graphs show mean values +/- s.d.

5.6. Discussion

The present findings indicate that rapid improvement in physical performance of either skeletal and cardiac muscle can be achieved after only 8 doses of RNP in conjunction with

augmented autophagy. In contrast, oral rapamycin in pharmacological doses exerted no significant effect on strength within the same interval. The observations that the improvement in grip strength is repeatable after a drug holiday in the same mice, together offer further support for the salutary role of RNP on enhancing autophagy, global physical performance, and cardiac function in muscular dystrophy. The muted response to strength testing in aged mdx as compared to the clear enhancement in cardiac function reveals a not unexpected limitation on what might be achievable after initiation of therapy late in the disease process.

Recently published work suggests that autophagy induction may be beneficial to *mdx* animals, whether induced by rapamycin or by dietary protein reduction (Pauly, Daussin et al. 2012). Moreover**,** a decrease in autophagic flux in vivo has been previously reported for an animal model of Bethlem myopathy and Ullrich congenital muscular dystrophy due to mutations in *Col6a*-/- suggesting that disturbed autophagy might occur in other muscular dystrophies (Grumati, Coletto et al.), yet this mechanism has not been evaluated previously for *aged* DMD/*mdx,* as we show here. Furthermore, no prior studies have demonstrated improvements in global physical performance in vivo or cardiac function after rapamycin therapy in aged animals that might be attributable to enhanced autophagy.

The observation of a muted response to short term RNP in the older 17-month-old mice for skeletal muscle performance in the face of a clear improvement in myocardial LVEF and clear induction of autophagy points out certain divergent pathophysiological features of the disease. It is recognized that the heart disease in DMD appears later than the skeletal muscle weakness, but emerges ultimately as a major source of morbidity and mortality. Why heart muscle is relatively more resistant to disease progression than is skeletal muscle despite continuous contractile

activity remains unknown. Interestingly, the disease in the heart evolves *regionally* (e.g., base>apex) despite the ubiquitous loss of the dystrophin (Chapter 2~3).

Although recent retrospective analyses of steroids in DMD are highly suggestive of a beneficial long-term effect on cardiac function (Schram, Fournier et al. 2013), the present data are the first to illustrate such rapid improvement with systemic rapamycin in a prospective trial invoking a unique mechanism of action. Parenthetically, our observation of improved LVEF even in wild type subjects (Figure 22) accords with a recent report by Flynn et al. noting better LVEF in 24 month-old female nondystrophic animalds treated continuously for 3 months with rapamycin in an oral "high delivery" formulation (Flynn, O'Leary et al. 2013). The attenuated response of skeletal muscle strength to RNP in older mdx in our study suggests either that longer term or more aggressive therapy might be required at this stage to enhance strength, or that certain limitations may exist for this (or even any) form of therapy, neither of which is especially surprising. Interestingly, Flynn et al also reported that oral rapamycin increased *endurance* but not *intensity* of activity in 24 month-old female mice, suggesting a muted effect on strength improvement in older subjects in general, which accords with our observation on grip strength for the 17-month old dystrophic mice (Flynn, O'Leary et al. 2013). Regardless, the ability of RNP to rapidly improve cardiac performance suggests that a single agent might be useful.

The cumulative dose of rapamycin administered to the animals in the rapamycin-loaded nanoparticle treatment group was within the limits of recommended oral doses for patients receiving immunosuppressive therapy when accounting for ~20% oral absorption in humans (Ferron, Conway et al. 1997). The rationale for comparing intravenous nanoparticle rapamycin

therapy with oral rapamycin delivery stems from the conventional practice of oral delivery as standard of care in patients requiring immune suppression, which is known to be effective and well tolerated at the recommended dose levels. We accounted for the well-known and previously reported bioavailability for oral dosing (rough estimates: ~10% in mice (Napoli, Wang et al. 1997; Stepkowski 2003; O'Reilly, McSheehy et al. 2010) by augmenting the doses that were delivered to mice by oral gavage to ensure adequate delivery. Typical clinical maintenance dosing for oral delivery of sirolimus in organ-transplant scenarios for body mass greater than 40 kg is 2 mg/day (Rapamune, Pfizer Inc, Philadelphia, PA). Assuming 20% bioavailability, this equates to approximately 0.4 mg of rapamycin in circulation per day, or approximately 0.006 mg/kg/day for a 70 kg patient. The maximum permissible daily dose of rapamycin is 40 mg, which equates to 0.11 mg/kg/day. Mice treated with RNP i.v. in the current study were given 0.067 mg/kg rapamycin biweekly for a total of 8 times over 4 weeks, or the equivalent of 0.002 mg/kg/day, within the clinical bounds for regular therapeutic use.

The intravenous dose used here was approximately 7-fold less than the calculated absorbed oral dose administered to *mdx* mice by Eghtesad and colleagues to improve muscle histopathology (Eghtesad, Jhunjhunwala et al.). Moreover, Eghtesad also reported that oral or injected rapamycin exerted no affect on the TA muscle, in contrast to the marked upregulation of autophagy reported here in the TA after RNP therapy (see Figure 26). Taken together, these data indicate that at clinically relevant doses of oral rapamycin for *mdx* animals, which scale up to 4–fold greater than the recommended oral dose for patients, no improvement in skeletal muscle strength might be expected. In contrast, a clinically approved cumulative dose of rapamycin administered in NP formulations rapidly elicited marked improvement in both global physical

performance and cardiac function after only eight i.v. treatments, which could represent an advantage for periodic, short-term dosing.

Furthermore, nanoparticles alone did not increase autophagic flux in wild-type mice whereas rapamycin nanoparticles did. While rapamycin is known to promote autophagy via an mTOR dependent mechanism, the mechanism by which nanoparticles influence autophagy is not known. It is intriguing that nanoparticles were unable to enhance autophagy in wild-type mice with presumably normal sarcolemmal structure whereas in *mdx* mice that have defective sarcolemmal integrity due to dystrophin mutations, nanoparticles were effective.

Rapamycin also exhibits mTORC1-independent effects when it binds to FKBP12 on the ryanodine receptor. Previous studies suggest that binding of rapamycin disrupts the ryanodine receptor's functions and therefore would be expected to elicit dysfunctional calcium handling (Ahern, Junankar et al. 1997; Avila, Lee et al. 2003). However, in *mdx* animals, the ryanodine receptor itself appears to be dysfunctional (Bellinger, Reiken et al. 2009). It may be the case that the addition of rapamycin acts to modulate some of these receptors in a favorable manner and effect more normal calcium handling or else acts to decrease the expression of the receptors as has been previously reported (Avila and Dirksen 2005).

The effectiveness of nanoparticles and rapamycin nanoparticles for stimulating autophagy in *mdx* mouse muscle mirrors that of their efficacy in rapidly improving grip strength and cardiac function. Although these data may not establish absolute proof of cause and effect for the relationship between autophagy and strength, they suggest an intriguing candidate mechanism for the decline in strength that might be manageable clinically with an approved drug and a new delivery system.

Although the exact mechanism responsible for rapamycin's entry into muscle tissue remains to be clarified, the effect on autophagy is clear and seems dependent on nanoparticle depot delivery, because oral therapy is ineffective at the doses that were administered. The sustained presence of nanoparticles and rapamycin in skeletal and cardiac tissues is clear from the ^{19}F spectroscopy and the fluorescence imaging data. Prior pharmacokinetic studies in both rabbits and mice using PFC nanoparticles have confirmed a clearance halftime (or, elimination half-life) of ~3-5 hours in normal mice and rabbits used in various cancer models (Hu 2007; Soman, Baldwin et al. 2009), irrespective of molecular targeting, suggesting that there should be ample opportunity to penetrate into the damaged tissues. We previously have demonstrated rapid permeation of these nanoparticles in other situations where leaky or disrupted vasculature pertains, such as advanced atherosclerosis in cholesterol fed rabbits, and even in atherosclerotic human carotid endarterectomy specimens (Cyrus, Zhang et al. 2008; Zhang, Zhang et al. 2011). It is instructive to note that in dystrophic subjects, recent and prior publications have pointed out the widespread vascular dysfunction and damage that permits egress of circulating components into muscle interstitium (Vidal, Ardite et al. 2012). Dystrophic subjects also harbor defects in vascular endothelium that render lining cells susceptible to apoptosis and impaired angiogenesis (Palladino, Gatto et al. 2013), creating a situation of barrier dysfunction that even applies to the blood-brain barrier (Lien, Mohanta et al. 2012).

Regarding the translational potential of this approach, we note that these beneficial effects on both heart and skeletal muscle were achieved at a cumulative dose of rapamycin that accords with clinically recommended dosing. Although the side effects of rapamycin on glucose tolerance, weight gain, blood pressure, and immune responsiveness are recognized, the drug is generally well tolerated over many years by patients with organ transplantation. The fact that

both prednisone and rapamycin appear to induce autophagy as a possible mechanism of action raises the possibility that the potential deleterious consequences of either agent might be mitigated if used in lower doses in combination, or at least if RNP could be employed for a steroid sparing action.

Chapter 6: Conclusion

6.1. Summary of major findings

In this study, we observed that:

1. Myocardial sheets can be imaged in fresh/unfixed/unstained heart with photoacoustic image microscopy, indicating that sheet structures are not just dehydration artifacts as criticized in earlier histology studies (Zhang, Cheng *et al*. 2012).
2. By using Langendorff perfused heart preparations with DTI, viable myocardial sheet function can be imaged without motion-artifact. We observed that sheet dysfunction is manifest in diastole but not in systole, indicating a relaxation problem with mdx hearts (Chapter 2).
3. Fibrosis and sheet dysfunction evolve *regionally* in the *mdx* mouse heart at the base despite the lack of dystrophin in every cardiac cell, indicating that all other observed concomitant pathologies contributing mechanistically to the cardiomyopathy are secondary and developmental rather than primary drivers of the disease process (Chapter 2).
4. Sheet dysfunction is *reversible* by lowering the perfusate calcium concentration, i.e., *mdx* heart exhibits *calcium* dependent relaxation-failure (Chapter 2).
5. At least two tensor invariants are needed to describe the anisotropy of the diffusion tensor, although most related research has reported only fractional anisotropy for reasons of simplicity. Here we demonstrate how the *mode of anisotropy* and *fractional anisotropy* provide complimentary information regarding myocardial architecture anisotropy in mdx mice (Chapter 3).

6. Abnormal calcium transients are *stretch activated* and evolve *regionally* first at the base, indicating that the lack of dystrophin triggers calcium mishandling more quickly at the base but not the apex, especially when stretched (Chapter 4).
7. Fibrosis, sheet dysfunction, and calcium mishandling are all more severe in older *mdx* mice (16 month old) than in young mice (3 month old).

6.2. Future works:

6.2.1. Intervention for calcium mishandling and autophagy in DMD

In Chapter 2, we found that mdx sheet dysfunction is regional, progressive and calcium dependent. Therefore, we hypothesized that if we correct the calcium mishandling, we could ameliorate sheet dysfunction. This was carried out in whole hearts by adjusting perfusates with good results, which is compatible with other strategies mentioned above to ameliorate calcium mishandling and systolic dysfunction by genetically engineered approaches. In the case of sheet dysfunction that produces diastolic abnormalities early in the course of heart disease, which itself may predispose to further damage by "stiffening" the heart, even earlier metrics of beneficial interventions might be observed via restoration of sheet mechanics. Although steroids are currently the most effective treatment for DMD patients, their efficacy decreases after prolonged treatment (Markham, Spicer et al. 2005). Therefore, cocktail therapies targeting different pathological mechanisms with the use of steroids, current calcium approaches, ACEi, autophagy, and beta-blockers might be desirable in the hopes that gene therapy might emerge as a first line therapy. The proposed DTI measured sheet angle could offer a surrogate for the efficacy of such interventions.

6.3. Remarks on dystrophin function

Here it is instructive to quote from other author's insights into the progressive regional nature of dystrophin-null cardiomyopathy (Judge, Kass *et al*. 2011):

> "One hypothesis regarding the cause of cardiomyopathy for individuals with reduced or absent dystrophin is based simply on a structural deficiency. Since dystrophin is part of the DGC, its primary role may be to hold this complex together. When deficient or absent, the dystrophin-associated glycoprotein complex may deteriorate due to the hemodynamic stress associated with normal left ventricular function. Evidence for this includes the loss of several components of the DGC from the plasmalemma when dystrophin is absent. If this were the only contribution of dystrophin to normal cardiac function, then one would anticipate that cardiac dysfunction would be more *uniform* with regard to its age of onset and severity in DMD. … Another hypothesis for cardiac dysfunction in DMD and BMD posits that dystrophin and its associated complex of ECM glycoproteins play a *regulatory* role. "

Then one might ask, what regulatory function might dystrophin have? And furthermore, why would this be different at the base and apex? In fact, nitric oxide, SMAD, or TGF-beta pathways all are reported to be affected by dystrophin-null conditions (Chao, Silvagno *et al*. 1998; Heydemann, Ceco *et al*. 2009; Goldstein, Kelly *et al*. 2011), but it is still unclear what the role of dystrophin in those pathway might be and whether these problems are primary or secondary to myocyte damage. For example, does dystrophin turn on NO pathway to increase coronary flow in response to certain mechanical input? If dystrophin is a switch, what turns it on in response to what stimulus? The function of dystrophin can be discussed from an evolutionary standpoint. First, dystrophin is an ancient protein that exists even in drosophila and sea urchin (Neuman, Kaban *et al*. 2001; Kucherenko, Marrone *et al*. 2011). Morris 1977 found that "*In Xenopus heart, little or no dystrophin was found on Western blots but the dystrophin-related protein, utrophin, was abundant. ... In skeletal muscle, however, Xenopus resembles mammals in expressing dystrophin at the sarcolemma and very little utrophin*" (Morris 1997). Based on the fact that

Xenopus, an amphibian, does not express dystrophin in the heart, one could hypothesize that dystrophin was adapted in mammal hearts for some unknown function that is not required in amphibian hearts. Therefore, a comparative study on heart function and dystrophin distribution in base vs apex of the heart could shed lights on dystrophin's mysterious function. It also would be telling to investigate dystrophin's expression in heart development, especially to focus on different locations exhibiting different stress levels in embryological development; and at different development stages such as before and after the foramen ovale closes. It is possible that cardiac dystrophin's regional expression may change dramatically as a marked redistribution of cardiac stress occurs during and after birth, in light that dystrophin protein was not detected in early embryonic days until prenatal stage in rat (Tanaka and Ozawa 1990).

It also is curious why the apex is spared. Recall the Laplace law (eq41).

$$S = \frac{P}{2} \times \frac{r}{h} \qquad \ldots\ldots \qquad \text{eq41}$$

Stress in the ventricular wall (**S**) is proportional to transmural pressure (**P**) and the ratio between radius (**r**) to wall thickness (**h**) (Warren W. Burggren 1997). Indeed, Kim *el al* have reported ~30% higher wall stress at the base of anesthetized canine heart (Kim, Min *et al*. 1985). In 1998, using markers and intraventricular pressure catheters, DeAnda *et al* also estimated up to four times higher wall stress in base compared to apex in awake dogs (DeAnda, Komeda *et al*. 1998), agreeing with the prediction made with Laplace law.

Evolution in some respects is an adaptation to stress. 360 Million years ago, fish evolved into amphibians and faced new challenges in a terrestrial environment, including air exchange, dehydration, and *gravity*. In water, animal's body weight is supported by buoyancy, which is not operative on land. Therefore, gravity might contribute to the fact that the largest extant land

animal, the African bush elephant (4.9 tons, 6m)[9], is 22 times lighter than the largest marine animal blue whales (110 tons, 25.5m)[10]. Humans assume that living on the land is simple, but living in the ocean is challenging. But in evolution, the ability to deal with the land environment is *emergent* as opposed to encoded. Indeed, terrestrial animals likely must "pay" for their body size with certain limiting adaptations. Because area-dependent functions increase less rapidly than volume-dependent functions as an organism's size increase, severe scaling constraints may result as land organisms evolved to larger size (Schmidt-Nielsen 1984). For example, assuming no allometry, body weight is proportional to the body length to the power of **three**, while the muscle cross section area[11] is proportional to body length to the power of **two.** Therefore, the stress (force/area) in muscle, in order to bear the body weight of the land animal, is proportional to the "body weight divided by muscle cross section area," which is body length to the power of **one**. Therefore, we might assume that a 180 cm tall man experiences **twice** the stress in the calf as does a 90 cm tall man, all else being equal.

It is logical then that the fundamental function of *dystrophin* is **to protect muscle in high stress environment**. Myocardial sheet/calcium transient abnormalities and fibrosis manifest more at base but not apex in 16 month old *mdx* mice (Chapter 2), consistent with higher stress at the base than apex (DeAnda, Komeda *et al*. 1998). Furthermore, myocardial sheet abnormalities and fibrosis do not appear in 3 month old *mdx* mice, which have 15% smaller heart radius. Potentially, the smaller radius resulting in smaller stress spares the heart from abnormalities at

[9] African bush elephant. Animal Diversity Web. http://animaldiversity.ummz.umich.edu/site/accounts/information/Loxodonta_africana.html

[10] Blue Whale. The Marine Mammal Center. http://www.marinemammalcenter.org/education/marine-mammal-information/cetaceans/blue-whale.html#.UjIVGcZ6ZRs

[11] Vertebrate striated muscle exerts nearly a constant peak tensile stress, ~200k Pa = 2M dyn/cm^2, among species. Biewener, A. A. (1989). "Scaling body support in mammals: limb posture and muscle mechanics." Science **245**(4913): 45-48.

earlier ages. Therefore, young mice do not exhibit a cardiac, or even much skeletal dystrophic phenotype, despite the fact that all tissues lack dystrophin before birth.

DMD patients (dystrophin-null) experience the onset of symptoms before two year old and become wheelchair bounded between ages 7 and 13. On the other hand, BMD patients (dystrophin-deficient) have much more benign progress of disease. BMD patients have their onset of symptoms between ages 2 to 21, and become wheelchair bound between ages 22 and 51 (Emery and Skinner 1976). That is, the partially expressed dystrophin in BMD patients is still able to protect the increased stress from the growing body size until age 22 to 51. In a 111 DMD patients study, height was found to be correlated with disease progression (disability accessed by the Vignose scale) with a correlation coefficient of 0.352 ($p<0.001$), indicating that small stature might protect against the ravages of DMD. A classic paper that has been cited 870 times has reported sarcolemma damage is linearly correlated with stress (force/area cross section). That is, *mdx* diaphragm muscle shows more damage than does wildtype diaphragm muscle (Petrof, Shrager *et al*. 1993). Similarly, cardiomyocytes of *mdx* mice are more vulnerable to mechanical stress induced by isoproterenol and aortic banding (Danialou, Comtois *et al*. 2001) than are normal myocytes. Indeed, anti human growth hormone (HGH) therapy was found to be effective in DMD patients (Zatz, Betti *et al*. 1986). Four case reports suggested that patients with deficiency in both HGH and dystrophin show slow or no progress of muscular waste until the administered to solve the short stature (Zatz, Betti *et al*. 1981; Zatz and Betti 1986; Ghafoor, Mahmood *et al*. 2003; Calcaterra, Malvezzi *et al*. 2013). However, an HGH inhibitor, mazindol, fails to inhibit the growth over longer times as suggested by Zatz (Zatz, Rapaport *et al*. 1988):

> "However, the recent report of two new DMD patients with short stature and a benign evolution of the dystrophic process (Passos *et al*., 1988; Wu *et al*., 1988) and the observation of wide variability in the progression of the disease in DMD/BMD patients

> with apparently the same DNA deletions suggests that secondary factors, such as growth hormone (GH) may be implicated in the progression of the disease (Infante and Huszagh, 1988; Malhotra et al., 1988)."

That is, Zatz speculated GH itself might have modified the disease. It appears rather more likely that the GH→height→stress cascade is the operative factor in modifying the disease.

It is known that, in DMD patients, calf muscles fail to perform normal function first, then the diaphragm fails (Bach 1992; Hamada, Ishikawa *et al*. 2011). The cardiomyopathy emerges last (Fayssoil, Nardi *et al*. 2010). It is natural to ask: among the calf, the diaphragm, and the heart, which muscle bears the most stress (force/area)? Does the failure sequence in DMD muscles correspond to the ranking of stress? To the best of my knowledge, there is no study comparing stresses in these three muscles together in DMD nor in *mdx* mice. However, the following summarizes the existing data.

Thorpe *et al* found normal young adults (~1.7m ~73kg) have peak stresses of 100 kNm^{-2} during high jumps and 150kNm^{-2} during 4ms^{-1} running in calf (gastrocnemius and the soleus) (Thorpe, Li *et al*. 1998). Using the reported height of age 8 DMD patients, ~1.4m (Beenakker, de Vries *et al*. 2002), and assuming no allometry and stress is roughly proportional to the height, we can estimate the high jump and **running** stress in a DMD boy are 82 and **123** kN/m^2 , respectively, which should be the upper limit of stress in DMD patient calf, because they have pseudo-hypertrophic calf and less contractility due to fibrosis.

Stress data in calf muscles in a standing posture in normal humans are scanty. However, Morse *et al* have reported isometric maximum stress of calf muscles in young (131 kN/m^2 , age 25, 1.7m, 79 kg) and elderly (92 kN/m^2 , age 74, 1.7 m, 78 kg) normal people (Morse, Thom *et al*. 2005). Taking elderly subjects stress data and assuming no allometry, a DMD patient of 1.4 m

height should have an isometric maximum stress of 92*1.4/1.7= **75** kN/m^2 in calf. Although assuming no allometry may not be true, it is the best approximation devoid of additional calf geometry information. I cannot find any literature addressing the fascicle force and physiological cross-sectional area in calf muscles of DMD patients. However, from the above two literature sources, I estimate that standing calf stress in DMD patient is smaller than **75 kN/m^2**.

mdx mice diaphragm strips were reported to exert maximum tetanic stress of **91~136 kN/m^2** in *ex vivo* experiment (Lynch, Rafael *et al*. 1997; Lynch, Hinkle *et al*. 2001). *In vivo* measurement of diaphragm stress were not available in literature, to the best of my knowledge, probably because the thin anatomical geometry of the diaphragm limits the observation opportunity. However, Hughes *et al* used two balloons placed in the stomach and esophagus to measure the transdiaphragmatic pressure in normal adult humans and reported a value of 143 cm H_2O (105 mmHg) (Hughes, Polkey *et al*. 1999). Meanwhile, Beck reported a maximum transdiaphragmatic pressure of 7.6 cmH_2O (5.6 mmHg) in DMD patients with advanced stage disease (N=8, mean age 25) (Beck, Weinberg *et al*. 2006). Although the *in vivo* stress of the diaphragm was not reported, it is not unreasonable to assume that the diaphragm exhibits comparable or higher stress than does heart wall, because the thickness of diaphragm (1.74 mm thick in 10 year old DMD patients; 1.45 mm in normal controls (De Bruin, Ueki *et al*. 1997)) is >3 times thinner than heart wall (4.8 mm in diastole; 8.7 mm in systole (Goldberg, Feldman *et al*. 1980)). Diaphragm has comparable maximal transmural pressure as with the heart (105 mmHg vs 120mmHg). Meanwhile, the diaphragm has much larger radius of curvature.

Numerical values of stress in normal adult human heart wall are more abundant. Normal wall stress was reported to be **18~33 kN/m^2** in systole and 2~3 kN/m^2 in diastole (Hood, Rackley *et al*. 1968; Grossman, Jones *et al*. 1975). In DMD, one study reported 23 DMD patients with

mean age of 8 have a wall stress of **49** (Markham, Kinnett *et al*. 2008). Unfortunately. this paper ignored the units of wall stress.

In conclusion, values from literature suggest that the calf might be stressed more in 1.4m tall boys than the heart (**75** vs **18~49 kN/m^2**). I speculate that the diaphragm might experience even higher stresses than the heart because of the comparable transmural pressures in the face of thinner thickness, and larger curvature radius, but there are no available data reported. After reviewing all of the published values of stresses, it would not be surprising if the stress ranking is actually: calf > diaphragm > heart, which might explain the temporal sequence of failing muscles in DMD patients.

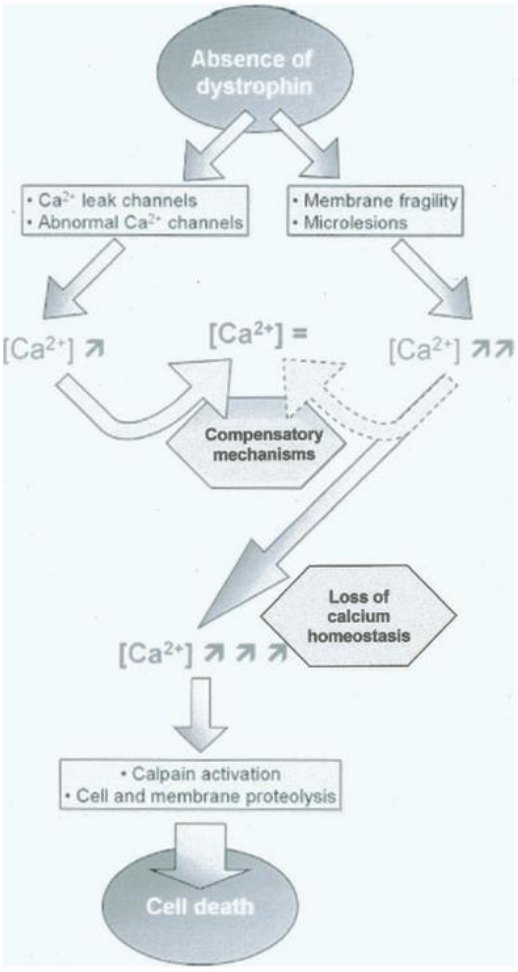

Deconinck proposed a damage pathway initiating with the lack of dystrophin (Figure 27) (Deconinck and Dan 2007). However, this simplistic model fails to incorporate the supposition that it might be stress itself that modifies the degree of damage in different parts of the heart and skeletal muscles at different ages and body sizes.

Figure 27. mdx dystrophy pathway proposed by Deconinck *et al*. (Deconinck and Dan 2007)

Hauser, Whitehead, and Yeung suggested that "*NADPH oxidase is a major source of reactive oxygen species in dystrophic muscle and its enhanced activity has a stimulatory effect on* ***stretch-induced*** *Ca^{2+} entry, a key mechanism for muscle damage and functional impairment.*" (Hauser, Hoger *et al*. 1995; Whitehead, Yeung *et al*. 2010; Yang, Chin *et al*. 2013) That is, these authors have recognized the stretch-induced damage is a factor complementing the lack of dystrophin. Therefore, I propose an updated damage pathway in Figure 28, proposing that the stress in muscle is the activation factor operating on the ubiquitous lack of dystrophin.

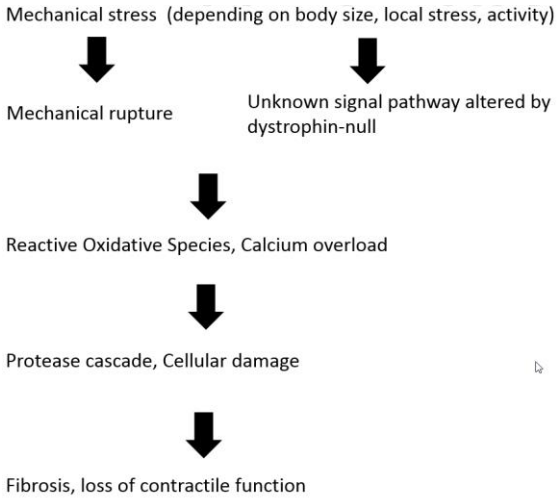

Figure 28. Hypothesized *mdx* dystrophy pathway.

To ameliorate DMD, beta blockers, ACE inhibitors, and growth inhibition have all been reported to slow DMD progression (Zatz, Betti *et al*. 1986). In the hypothesis proposed in this Chapter, these therapies work because they all modulate stresses in muscles. However, none of these can have a long-term curative effect, leaving more revolutionary genetic and pharmaceutical strategies desirable.

References

Adelman, S. J. (2010). "Sirolimus and its analogs and its effects on vascular diseases." Curr Pharm Des **16**(36): 4002-4011.

Ahern, G. P., P. R. Junankar, et al. (1997). "Ryanodine receptors from rabbit skeletal muscle are reversibly activated by rapamycin." Neurosci Lett **225**(2): 81-84.

Ahuja, R., V. Kalra, et al. (2000). "Prevalence and patterns of cardiac involvement in duchenne muscular dystrophy." Indian Pediatr **37**(11): 1246-1251.

Allen, D. G., O. L. Gervasio, et al. (2010). "Calcium and the damage pathways in muscular dystrophy." Can J Physiol Pharmacol **88**(2): 83-91.

Alloatti, G., M. P. Gallo, et al. (1995). "Properties of cardiac cells from dystrophic mouse." Journal of molecular and cellular cardiology **27**(8): 1775-1779.

Altamirano, F., J. R. Lopez, et al. (2012). "Increased resting intracellular calcium modulates NF-kappaB-dependent inducible nitric-oxide synthase gene expression in dystrophic mdx skeletal myotubes." The Journal of biological chemistry **287**(25): 20876-20887.

Araujo, K. P., G. Bonuccelli, et al. (2013). "Bortezomib (PS-341) treatment decreases inflammation and partially rescues the expression of the dystrophin-glycoprotein complex in GRMD dogs." PLoS One **8**(4): e61367.

Ashford, M. W., Jr., W. Liu, et al. (2005). "Occult cardiac contractile dysfunction in dystrophin-deficient children revealed by cardiac magnetic resonance strain imaging." Circulation **112**(16): 2462-2467.

Ashikaga, H., J. C. Criscione, et al. (2004). "Transmural left ventricular mechanics underlying torsional recoil during relaxation." American journal of physiology. Heart and circulatory physiology **286**(2): H640-647.

Avila, G. and R. T. Dirksen (2005). "Rapamycin and FK506 reduce skeletal muscle voltage sensor expression and function." Cell Calcium **38**(1): 35-44.

Avila, G., E. H. Lee, et al. (2003). "FKBP12 binding to RyR1 modulates excitation-contraction coupling in mouse skeletal myotubes." J Biol Chem **278**(25): 22600-22608.

Bach, J. R. (1992). "Ventilator use by muscular dystrophy association patients." Archives of physical medicine and rehabilitation **73**(2): 179-183.

Bahler, R. C., T. Mohyuddin, et al. (2005). "Contribution of Doppler tissue imaging and myocardial performance index to assessment of left ventricular function in patients with Duchenne's muscular dystrophy." Journal of the American Society of Echocardiography : official publication of the American Society of Echocardiography **18**(6): 666-673.

Bahn, M. M. (1999). "Invariant and orthonormal scalar measures derived from magnetic resonance diffusion tensor imaging." Journal of magnetic resonance **141**(1): 68-77.

Balaban, B., D. J. Matthews, et al. (2005). "Corticosteroid treatment and functional improvement in Duchenne muscular dystrophy: long-term effect." Am J Phys Med Rehabil **84**(11): 843-850.

Balzer, P., A. Furber, et al. (1999). "Regional assessment of wall curvature and wall stress in left ventricle with magnetic resonance imaging." The American journal of physiology **277**(3 Pt 2): H901-910.

Banks, G. B. and J. S. Chamberlain (2008). "The value of mammalian models for duchenne muscular dystrophy in developing therapeutic strategies." Curr Top Dev Biol **84**: 431-453.

Banks, G. B. and J. S. Chamberlain (2008). "The value of mammalian models for duchenne muscular dystrophy in developing therapeutic strategies." Current topics in developmental biology **84**: 431-453.

Baron, M. L., S. Hecht, et al. (2011). "Intracranial extension of retrobulbar blastomycosis (Blastomyces dermatitidis) in a dog." Veterinary ophthalmology **14**(2): 137-141.

Basser, P. J. (1995). "Inferring microstructural features and the physiological state of tissues from diffusion-weighted images." NMR in biomedicine **8**(7-8): 333-344.

Beck, J., J. Weinberg, et al. (2006). "Diaphragmatic function in advanced Duchenne muscular dystrophy." Neuromuscular disorders : NMD **16**(3): 161-167.

Beenakker, E. A., J. de Vries, et al. (2002). "Quantitative assessment of calf circumference in Duchenne muscular dystrophy patients." Neuromuscular disorders : NMD **12**(7-8): 639-642.
Bellinger, A. M., S. Reiken, et al. (2009). "Hypernitrosylated ryanodine receptor calcium release channels are leaky in dystrophic muscle." Nat Med **15**(3): 325-330.
Bellinger, A. M., S. Reiken, et al. (2008). "Remodeling of ryanodine receptor complex causes "leaky" channels: a molecular mechanism for decreased exercise capacity." Proc Natl Acad Sci U S A **105**(6): 2198-2202.
Berry, S. E., P. Andruszkiewicz, et al. (2013). "Nestin expression in end-stage disease in dystrophin-deficient heart: implications for regeneration from endogenous cardiac stem cells." Stem cells translational medicine **2**(11): 848-861.
Biewener, A. A. (1989). "Scaling body support in mammals: limb posture and muscle mechanics." Science **245**(4913): 45-48.
Biggar, W. D., V. A. Harris, et al. (2006). "Long-term benefits of deflazacort treatment for boys with Duchenne muscular dystrophy in their second decade." Neuromuscul Disord **16**(4): 249-255.
Bode, F., A. Katchman, et al. (2000). "Gadolinium decreases stretch-induced vulnerability to atrial fibrillation." Circulation **101**(18): 2200-2205.
Bowles, D. E., S. W. McPhee, et al. (2012). "Phase 1 gene therapy for Duchenne muscular dystrophy using a translational optimized AAV vector." Molecular therapy : the journal of the American Society of Gene Therapy **20**(2): 443-455.
Bulfield, G., W. G. Siller, et al. (1984). "X chromosome-linked muscular dystrophy (mdx) in the mouse." Proceedings of the National Academy of Sciences of the United States of America **81**(4): 1189-1192.
Calcaterra, V., A. Malvezzi, et al. (2013). "Growth hormone deficiency in a patient with becker muscular dystrophy: a pediatric case report." Case reports in endocrinology **2013**: 684249.
Cerqueira, M. D., N. J. Weissman, et al. (2002). "Standardized myocardial segmentation and nomenclature for tomographic imaging of the heart. A statement for healthcare professionals from the Cardiac Imaging Committee of the Council on Clinical Cardiology of the American Heart Association." The international journal of cardiovascular imaging **18**(1): 539-542.
Chase, A. and C. H. Orchard (2011). "Ca efflux via the sarcolemmal Ca ATPase occurs only in the t-tubules of rat ventricular myocytes." J Mol Cell Cardiol **50**(1): 187-193.
Chelly, J., J. C. Kaplan, et al. (1988). "Transcription of the dystrophin gene in human muscle and non-muscle tissue." Nature **333**(6176): 858-860.
Chen, F., Y. Suzuki, et al. (2005). "Dynamic susceptibility contrast-enhanced perfusion MR imaging at 1.5 T predicts final infarct size in a rat stroke model." J Neurosci Methods **141**(1): 55-60.
Chen, J., W. Liu, et al. (2005). "Regional ventricular wall thickening reflects changes in cardiac fiber and sheet structure during contraction: quantification with diffusion tensor MRI." Am J Physiol Heart Circ Physiol **289**(5): H1898-1907.
Cheng, H., M. R. Lederer, et al. (1996). "Excitation-contraction coupling in heart: new insights from Ca^{2+} sparks." Cell Calcium **20**(2): 129-140.
Cheng, Y. J., D. Lang, et al. (2012). "Focal but reversible diastolic sheet dysfunction reflects regional calcium mishandling in dystrophic mdx mouse hearts." American journal of physiology. Heart and circulatory physiology **303**(5): H559-568.
Cirak, S., V. Arechavala-Gomeza, et al. (2011). "Exon skipping and dystrophin restoration in patients with Duchenne muscular dystrophy after systemic phosphorodiamidate morpholino oligomer treatment: an open-label, phase 2, dose-escalation study." Lancet **378**(9791): 595-605.
Costa, K. D., Y. Takayama, et al. (1999). "Laminar fiber architecture and three-dimensional systolic mechanics in canine ventricular myocardium." The American journal of physiology **276**(2 Pt 2): H595-607.
Costa, K. D., Y. Takayama, et al. (1999). "Laminar fiber architecture and three-dimensional systolic mechanics in canine ventricular myocardium." Am J Physiol **276**(2 Pt 2): H595-607.

Crowe, A., A. Bruelisauer, et al. (1999). "Absorption and intestinal metabolism of SDZ-RAD and rapamycin in rats." Drug Metab Dispos **27**(5): 627-632.
Cyrus, T., H. Zhang, et al. (2008). "Intramural delivery of rapamycin with αvβ3-targeted paramagnetic nanoparticles inhibits stenosis after balloon injury." Arteriosclerosis, Thrombosis, and Vascular Biology **28**(5): 820-826.
Danialou, G., A. S. Comtois, et al. (2001). "Dystrophin-deficient cardiomyocytes are abnormally vulnerable to mechanical stress-induced contractile failure and injury." FASEB journal : official publication of the Federation of American Societies for Experimental Biology **15**(9): 1655-1657.
Danowski, B. A., K. Imanaka-Yoshida, et al. (1992). "Costameres are sites of force transmission to the substratum in adult rat cardiomyocytes." The Journal of cell biology **118**(6): 1411-1420.
De Bruin, P. F., J. Ueki, et al. (1997). "Diaphragm thickness and inspiratory strength in patients with Duchenne muscular dystrophy." Thorax **52**(5): 472-475.
De Palma, C., F. Morisi, et al. (2012). "Autophagy as a new therapeutic target in Duchenne muscular dystrophy." Cell Death Dis **3**: e418.
DeAnda, A., Jr., M. Komeda, et al. (1998). "Estimation of regional left ventricular wall stresses in intact canine hearts." The American journal of physiology **275**(5 Pt 2): H1879-1885.
Deconinck, N. and B. Dan (2007). "Pathophysiology of duchenne muscular dystrophy: current hypotheses." Pediatric neurology **36**(1): 1-7.
Deux, J. F., P. Malzy, et al. (2008). "Assessment of calf muscle contraction by diffusion tensor imaging." European radiology **18**(10): 2303-2310.
Ding, L., M. J. Ellis, et al. (2010). "Genome remodelling in a basal-like breast cancer metastasis and xenograft." Nature **464**: 999-1005.
Dolber, P. C. and M. S. Spach (1987). "Picrosirius red staining of cardiac muscle following phosphomolybdic acid treatment." Stain Technol **62**(1): 23-26.
Dou, J. (2002). Mapping MyocardiaI Structure-Function Relations with Cardiac Diffusion and Strain MRI. PhD, Massachusetts Institute of Technology.
Dou, J., W. Y. Tseng, et al. (2003). "Combined diffusion and strain MRI reveals structure and function of human myocardial laminar sheets in vivo." Magnetic resonance in medicine : official journal of the Society of Magnetic Resonance in Medicine / Society of Magnetic Resonance in Medicine **50**(1): 107-113.
Douaud, G., S. Jbabdi, et al. (2011). "DTI measures in crossing-fibre areas: increased diffusion anisotropy reveals early white matter alteration in MCI and mild Alzheimer's disease." NeuroImage **55**(3): 880-890.
Duboc, D., C. Meune, et al. (2007). "Perindopril preventive treatment on mortality in Duchenne muscular dystrophy: 10 years' follow-up." Am Heart J **154**(3): 596-602.
Duboc, D., C. Meune, et al. (2007). "Perindopril preventive treatment on mortality in Duchenne muscular dystrophy: 10 years' follow-up." American heart journal **154**(3): 596-602.
Dunphy, G., H. W. Richter, et al. (1999). "The effects of mannitol, albumin, and cardioplegia enhancers on 24-h rat heart preservation." The American journal of physiology **276**(5 Pt 2): H1591-1598.
Efimov, I. R., D. T. Huang, et al. (1994). "Optical mapping of repolarization and refractoriness from intact hearts." Circulation **90**(3): 1469-1480.
Eghtesad, S., S. Jhunjhunwala, et al. (2011). "Rapamycin ameliorates dystrophic phenotype in mdx mouse skeletal muscle." Mol Med **17**(9-10): 917-924.
Eijsbouts, S. C., M. Majidi, et al. (2003). "Effects of acute atrial dilation on heterogeneity in conduction in the isolated rabbit heart." Journal of cardiovascular electrophysiology **14**(3): 269-278.
Emery, A. E. and R. Skinner (1976). "Clinical studies in benign (Becker type) X-linked muscular dystrophy." Clinical genetics **10**(4): 189-201.
Ennis, D. B. and G. Kindlmann (2006). "Orthogonal tensor invariants and the analysis of diffusion tensor magnetic resonance images." Magnetic resonance in medicine : official journal of the Society of Magnetic Resonance in Medicine / Society of Magnetic Resonance in Medicine **55**(1): 136-146.

Etheridge, M. L., S. A. Campbell, et al. (2013). "The big picture on nanomedicine: the state of investigational and approved nanomedicine products." Nanomedicine **9**(1): 1-14.
Fairclough, R. J., M. J. Wood, et al. (2013). "Therapy for Duchenne muscular dystrophy: renewed optimism from genetic approaches." Nature reviews. Genetics **14**(6): 373-378.
Fanchaouy, M., E. Polakova, et al. (2009). "Pathways of abnormal stress-induced Ca^{2+} influx into dystrophic mdx cardiomyocytes." Cell Calcium **46**(2): 114-121.
Fayssoil, A., O. Nardi, et al. (2010). "Cardiomyopathy in Duchenne muscular dystrophy: pathogenesis and therapeutics." Heart failure reviews **15**(1): 103-107.
Fayssoil, A., O. Nardi, et al. (2010). "Cardiomyopathy in Duchenne muscular dystrophy: pathogenesis and therapeutics." Heart Fail Rev **15**(1): 103-107.
Fedorov, V. V., R. Chang, et al. (2010). "Complex interactions between the sinoatrial node and atrium during reentrant arrhythmias in the canine heart." Circulation **122**(8): 782-789.
Ferron, G. M., W. D. Conway, et al. (1997). "Lipophilic benzamide and anilide derivatives as high-performance liquid chromatography internal standards: application to sirolimus (rapamycin) determination." J Chromatogr B Biomed Appl **703**(1-2): 243-251.
Finsterer, J. and C. Stollberger (2007). "Cardiac involvement determines the prognosis of Duchenne muscular dystrophy." Indian J Pediatr **74**(2): 209; author reply 210-202.
Flaim, S. (1994). "Pharmacokinetics and side effects of perfluorocarbon-based blood substitutes." Art Cells Blood Subs and Immob Biotech **22**(4): 1043-1054.
Flynn, J. M., M. N. O'Leary, et al. (2013). "Late-life rapamycin treatment reverses age-related heart dysfunction." Aging Cell.
Franco-Obregon, A. and J. B. Lansman (2002). "Changes in mechanosensitive channel gating following mechanical stimulation in skeletal muscle myotubes from the mdx mouse." The Journal of physiology **539**(Pt 2): 391-407.
Gailly, P., F. De Backer, et al. (2007). "In situ measurements of calpain activity in isolated muscle fibres from normal and dystrophin-lacking mdx mice." J Physiol **582**(Pt 3): 1261-1275.
Galban, C. J., S. Maderwald, et al. (2004). "Diffusive sensitivity to muscle architecture: a magnetic resonance diffusion tensor imaging study of the human calf." European journal of applied physiology **93**(3): 253-262.
Garrido, L., V. J. Wedeen, et al. (1994). "Anisotropy of water diffusion in the myocardium of the rat." Circulation research **74**(5): 789-793.
Geerts, L., P. Bovendeerd, et al. (2002). "Characterization of the normal cardiac myofiber field in goat measured with MR-diffusion tensor imaging." American journal of physiology. Heart and circulatory physiology **283**(1): H139-145.
Ghafoor, T., A. Mahmood, et al. (2003). "Duchenne muscular dystrophy with associated growth hormone deficiency." Journal of the College of Physicians and Surgeons--Pakistan : JCPSP **13**(12): 722-723.
Ghate, S. V., J. A. Baker, et al. (2011). "Titanium vs carbon coated ceramic breast tissue marker clips: 3T MR susceptibility artifact and local signal disturbance." Academic radiology **18**(6): 770-773.
Gilbert, S. H., D. Benoist, et al. (2012). "Visualization and quantification of whole rat heart laminar structure using high-spatial resolution contrast-enhanced MRI." American journal of physiology. Heart and circulatory physiology **302**(1): H287-298.
Gilbert, S. H., A. P. Benson, et al. (2007). "Regional localisation of left ventricular sheet structure: integration with current models of cardiac fibre, sheet and band structure." European journal of cardio-thoracic surgery : official journal of the European Association for Cardio-thoracic Surgery **32**(2): 231-249.
Giordano, F. J., H. He, et al. (1997). "Adenovirus-mediated gene transfer reconstitutes depressed sarcoplasmic reticulum Ca^{2+}-ATPase levels and shortens prolonged cardiac myocyte Ca^{2+} transients." Circulation **96**(2): 400-403.
Goemans, N. M., M. Tulinius, et al. (2011). "Systemic administration of PRO051 in Duchenne's muscular dystrophy." N Engl J Med **364**(16): 1513-1522.

Goldberg, S. J., L. Feldman, et al. (1980). "Echocardiographic determination of contraction and relaxation measurements of the left ventricular wall in normal subjects and patients with muscular dystrophy." Circulation **62**(5): 1061-1069.
Golumbek, P. T., R. M. Keeling, et al. (2007). "Strength and corticosteroid responsiveness of mdx mice is unchanged by RAG2 gene knockout." Neuromuscular disorders : NMD **17**(5): 376-384.
Goonasekera, S. A., C. K. Lam, et al. (2011). "Mitigation of muscular dystrophy in mice by SERCA overexpression in skeletal muscle." The Journal of clinical investigation **121**(3): 1044-1052.
Grant, R. P. (1965). "Notes on the Muscular Architecture of the Left Ventricle." Circulation **32**: 301-308.
Griggs, R. C., R. T. Moxley, 3rd, et al. (1991). "Prednisone in Duchenne dystrophy. A randomized, controlled trial defining the time course and dose response. Clinical Investigation of Duchenne Dystrophy Group." Archives of neurology **48**(4): 383-388.
Grossman, W., D. Jones, et al. (1975). "Wall stress and patterns of hypertrophy in the human left ventricle." The Journal of clinical investigation **56**(1): 56-64.
Grumati, P., L. Coletto, et al. (2010). "Autophagy is defective in collagen VI muscular dystrophies, and its reactivation rescues myofiber degeneration." Nat Med **16**(11): 1313-1320.
Gulati, S., A. Saxena, et al. (2005). "Duchenne muscular dystrophy: prevalence and patterns of cardiac involvement." Indian J Pediatr **72**(5): 389-393.
Hamada, S., Y. Ishikawa, et al. (2011). "Indicators for ventilator use in Duchenne muscular dystrophy." Respiratory medicine **105**(4): 625-629.
Han, R., M. D. Grounds, et al. (2006). "Measurement of sub-membrane [Ca^{2+}] in adult myofibers and cytosolic [Ca^{2+}] in myotubes from normal and mdx mice using the Ca^{2+} indicator FFP-18." Cell Calcium **40**(3): 299-307.
Hauser, E., H. Hoger, et al. (1995). "Oxyradical damage and mitochondrial enzyme activities in the mdx mouse." Neuropediatrics **26**(5): 260-262.
He, C. L., P. F. Yi, et al. (2013). "Xiang-Qi-Tang and its active components exhibit anti-inflammatory and anticoagulant properties by inhibiting MAPK and NF-kappaB signaling pathways in LPS-treated rat cardiac microvascular endothelial cells." Immunopharmacology and immunotoxicology **35**(2): 215-224.
Hecht, S., W. H. Adams, et al. (2011). "Magnetic resonance imaging susceptibility artifacts due to metallic foreign bodies." Veterinary radiology & ultrasound : the official journal of the American College of Veterinary Radiology and the International Veterinary Radiology Association **52**(4): 409-414.
Helm, P., M. F. Beg, et al. (2005). "Measuring and mapping cardiac fiber and laminar architecture using diffusion tensor MR imaging." Annals of the New York Academy of Sciences **1047**: 296-307.
Hermans, M. C., Y. M. Pinto, et al. (2010). "Hereditary muscular dystrophies and the heart." Neuromuscul Disord **20**(8): 479-492.
Hollinger, K., D. Gardan-Salmon, et al. (2013). "Rescue of dystrophic skeletal muscle by PGC-1alpha involves restored expression of dystrophin-associated protein complex components and satellite cell signaling." American journal of physiology. Regulatory, integrative and comparative physiology **305**(1): R13-23.
Holmes, A. A., D. F. Scollan, et al. (2000). "Direct histological validation of diffusion tensor MRI in formaldehyde-fixed myocardium." Magn Reson Med **44**(1): 157-161.
Hood, W. P., Jr., C. E. Rackley, et al. (1968). "Wall stress in the normal and hypertrophied human left ventricle." The American journal of cardiology **22**(4): 550-558.
Hsu, E. W., A. L. Muzikant, et al. (1998). "Magnetic resonance myocardial fiber-orientation mapping with direct histological correlation." The American journal of physiology **274**(5 Pt 2): H1627-1634.
Hu, G., Lijowski, M., Zhang, H., Partlow, K.C., Caruthers, S.D., Kiefer, G., Gulyas, G., Athey, P., Scott, M.J., Wickline, S.A., Lanza, G.M. (2007). " Imaging of Vx-2 rabbit tumors with αvβ3-integrin-targeted 111In nanoparticles." International Journal of Cancer **120**: 1951-1957.

Huang, J. L., C. T. Tai, et al. (2003). "Effect of atrial dilatation on electrophysiologic properties and inducibility of atrial fibrillation." Basic research in cardiology **98**(1): 16-24.
Hughes, P. D., M. I. Polkey, et al. (1999). "Diaphragm strength in chronic heart failure." American journal of respiratory and critical care medicine **160**(2): 529-534.
Ishikawa, Y., J. R. Bach, et al. (1999). "Cardioprotection for Duchenne's muscular dystrophy." Am Heart J **137**(5): 895-902.
Iwata, M., R. T. Cowling, et al. (2011). "Targeting the ACE2-Ang-(1-7) pathway in cardiac fibroblasts to treat cardiac remodeling and heart failure." Journal of molecular and cellular cardiology **51**(4): 542-547.
Janssen, P. M., N. Hiranandani, et al. (2005). "Utrophin deficiency worsens cardiac contractile dysfunction present in dystrophin-deficient mdx mice." American journal of physiology. Heart and circulatory physiology **289**(6): H2373-2378.
Jolapara, M., C. Kesavadas, et al. (2009). "Diffusion tensor mode in imaging of intracranial epidermoid cysts: one step ahead of fractional anisotropy." Neuroradiology **51**(2): 123-129.
Ju, J. S., S. E. Miller, et al. (2010). "Quantitation of selective autophagic protein aggregate degradation in vitro and in vivo using luciferase reporters." Autophagy **6**(5).
Judd, R. M., G. A. Rottman, et al. (1992). "Feasibility of 19F imaging of perfluorochemical emulsions to measure myocardial vascular volume." Magn Reson Med **28**(1): 129-136.
Judge, D. P., D. A. Kass, et al. (2011). "Pathophysiology and therapy of cardiac dysfunction in Duchenne muscular dystrophy." American journal of cardiovascular drugs : drugs, devices, and other interventions **11**(5): 287-294.
Keeling, R. M., P. T. Golumbek, et al. (2007). "Weekly oral prednisolone improves survival and strength in male mdx mice." Muscle Nerve **35**(1): 43-48.
Kim, H. C., B. G. Min, et al. (1985). "Estimation of local cardiac wall deformation and regional wall stress from biplane coronary cineangiograms." IEEE transactions on bio-medical engineering **32**(7): 503-512.
Kim, H. K., T. Laor, et al. (2010). "T2 mapping in Duchenne muscular dystrophy: distribution of disease activity and correlation with clinical assessments." Radiology **255**(3): 899-908.
Kim, H. K., T. Laor, et al. (2010). "Quantitative assessment of the T2 relaxation time of the gluteus muscles in children with Duchenne muscular dystrophy: a comparative study before and after steroid treatment." Korean journal of radiology : official journal of the Korean Radiological Society **11**(3): 304-311.
Kinali, M., V. Arechavala-Gomeza, et al. (2009). "Local restoration of dystrophin expression with the morpholino oligomer AVI-4658 in Duchenne muscular dystrophy: a single-blind, placebo-controlled, dose-escalation, proof-of-concept study." Lancet Neurol **8**(10): 918-928.
Kissel, J. T., D. J. Lynn, et al. (1993). "Mononuclear cell analysis of muscle biopsies in prednisone- and azathioprine-treated Duchenne muscular dystrophy." Neurology **43**(3 Pt 1): 532-536.
Kundu, M. and C. B. Thompson (2008). "Autophagy: basic principles and relevance to disease." Annu Rev Pathol **3**: 427-455.
Lang, D., A. V. Glukhov, et al. (2011). "Role of Pyk2 in cardiac arrhythmogenesis." Am J Physiol Heart Circ Physiol **301**(3): H975-983.
Lang, D., A. V. Glukhov, et al. (2011). "Role of Pyk2 in cardiac arrhythmogenesis." American journal of physiology. Heart and circulatory physiology **301**(3): H975-983.
Lang, D., M. Sulkin, et al. (2011). "Optical mapping of action potentials and calcium transients in the mouse heart." Journal of visualized experiments : JoVE(55).
Latt, J., M. Nilsson, et al. (2009). "Diffusion-weighted MRI measurements on stroke patients reveal water-exchange mechanisms in sub-acute ischaemic lesions." NMR in biomedicine **22**(6): 619-628.
LeGrice, I. J., B. H. Smaill, et al. (1995). "Laminar structure of the heart: ventricular myocyte arrangement and connective tissue architecture in the dog." Am J Physiol **269**(2 Pt 2): H571-582.

LeGrice, I. J., Y. Takayama, et al. (1995). "Transverse shear along myocardial cleavage planes provides a mechanism for normal systolic wall thickening." Circ Res **77**(1): 182-193.
Lehnart, S. E., C. Terrenoire, et al. (2006). "Stabilization of cardiac ryanodine receptor prevents intracellular calcium leak and arrhythmias." Proceedings of the National Academy of Sciences of the United States of America **103**(20): 7906-7910.
Lester, B. E., R. A. Standley, et al. (2013). "Muscle-specific substrate use during cycle exercise at 1 G: implications for astronaut muscle health." Aviation, space, and environmental medicine **84**(8): 789-796.
Li, W., W. Liu, et al. (2009). "Early manifestation of alteration in cardiac function in dystrophin deficient mdx mouse using 3D CMR tagging." J Cardiovasc Magn Reson **11**: 40.
Lien, C. F., S. K. Mohanta, et al. (2012). "Absence of glial alpha-dystrobrevin causes abnormalities of the blood-brain barrier and progressive brain edema." J Biol Chem **287**(49): 41374-41385.
Lynch, G. S. (2004). "Role of contraction-induced injury in the mechanisms of muscle damage in muscular dystrophy." Clin Exp Pharmacol Physiol **31**(8): 557-561.
Lynch, G. S., R. T. Hinkle, et al. (2001). "Force and power output of diaphragm muscle strips from mdx and control mice after clenbuterol treatment." Neuromuscular disorders : NMD **11**(2): 192-196.
Lynch, G. S., J. A. Rafael, et al. (1997). "Contractile properties of diaphragm muscle segments from old mdx and old transgenic mdx mice." The American journal of physiology **272**(6 Pt 1): C2063-2068.
Markham, L. W., K. Kinnett, et al. (2008). "Corticosteroid treatment retards development of ventricular dysfunction in Duchenne muscular dystrophy." Neuromuscular disorders : NMD **18**(5): 365-370.
Markham, L. W., E. C. Michelfelder, et al. (2006). "Abnormalities of diastolic function precede dilated cardiomyopathy associated with Duchenne muscular dystrophy." Journal of the American Society of Echocardiography : official publication of the American Society of Echocardiography **19**(7): 865-871.
Markham, L. W., R. L. Spicer, et al. (2005). "Steroid therapy and cardiac function in Duchenne muscular dystrophy." Pediatric cardiology **26**(6): 768-771.
Markham, L. W., R. L. Spicer, et al. (2005). "Steroid therapy and cardiac function in Duchenne muscular dystrophy." Pediatr Cardiol **26**(6): 768-771.
McNally, E. M. (2008). "Duchenne muscular dystrophy: how bad is the heart?" Heart **94**(8): 976-977.
Medvedev, A. V., A. M. Murro, et al. (2011). "Abnormal interictal gamma activity may manifest a seizure onset zone in temporal lobe epilepsy." International journal of neural systems **21**(2): 103-114.
Mellor, K. M., I. R. Wendt, et al. (2012). "Fructose diet treatment in mice induces fundamental disturbance of cardiomyocyte Ca^{2+} handling and myofilament responsiveness." Am J Physiol Heart Circ Physiol **302**(4): H964-972.
Mendell, J. R., K. Campbell, et al. (2010). "Dystrophin immunity in Duchenne's muscular dystrophy." The New England journal of medicine **363**(15): 1429-1437.
Mertens, L., J. Ganame, et al. (2008). "Early regional myocardial dysfunction in young patients with Duchenne muscular dystrophy." Journal of the American Society of Echocardiography : official publication of the American Society of Echocardiography **21**(9): 1049-1054.
Morawski, A. M., P. M. Winter, et al. (2004). "Quantitative "magnetic resonance immunohistochemistry" with ligand-targeted ^{19}F nanoparticles." Magn Reson Med **52**: 1255–1262.
Morelli, J. N., V. M. Runge, et al. (2011). "An image-based approach to understanding the physics of MR artifacts." Radiographics : a review publication of the Radiological Society of North America, Inc **31**(3): 849-866.
Mori, S. and J. Zhang (2006). "Principles of diffusion tensor imaging and its applications to basic neuroscience research." Neuron **51**(5): 527-539.
Morse, C. I., J. M. Thom, et al. (2005). "In vivo physiological cross-sectional area and specific force are reduced in the gastrocnemius of elderly men." Journal of applied physiology **99**(3): 1050-1055.

Moxley, R. T., 3rd, S. Ashwal, et al. (2005). "Practice parameter: corticosteroid treatment of Duchenne dystrophy: report of the Quality Standards Subcommittee of the American Academy of Neurology and the Practice Committee of the Child Neurology Society." Neurology **64**(1): 13-20.
Mukherjee, R., K. A. Apple, et al. (2006). "Protein kinase C isoform activation and endothelin-1 mediated defects in myocyte contractility after cardioplegic arrest and reperfusion." Circulation **114**(1 Suppl): I308-313.
Munch, D. F., H. T. Comer, et al. (1980). "Barium contracture: a model for systole." Am J Physiol **239**(3): H438-442.
Napoli, K. L., M. E. Wang, et al. (1997). "Distribution of sirolimus in rat tissue." Clin Biochem **30**(2): 135-142.
Napoli, K. L., M. E. Wang, et al. (1997). "Distribution of sirolimus in rat tissue." Clinical biochemistry **30**(2): 135-142.
Nazir, S. A. and M. J. Lab (1996). "Mechanoelectric feedback in the atrium of the isolated guinea-pig heart." Cardiovascular research **32**(1): 112-119.
Nicolas-Metral, V., E. Raddatz, et al. (2001). "Mdx myotubes have normal excitability but show reduced contraction-relaxation dynamics." Journal of muscle research and cell motility **22**(1): 69-75.
O'Brien, B. J., J. S. Stinson, et al. (2008). "Characterization of an NbTaWZr alloy designed for magnetic resonance angiography compatible stents." Biomaterials **29**(34): 4540-4545.
O'Reilly, T., P. M. McSheehy, et al. (2010). "Comparative pharmacokinetics of RAD001 (everolimus) in normal and tumor-bearing rodents." Cancer Chemother Pharmacol **65**(4): 625-639.
O'Reilly, T., P. M. McSheehy, et al. (2010). "Comparative pharmacokinetics of RAD001 (everolimus) in normal and tumor-bearing rodents." Cancer chemotherapy and pharmacology **65**(4): 625-639.
Ogata, H., Y. Ishikawa, et al. (2009). "Beneficial effects of beta-blockers and angiotensin-converting enzyme inhibitors in Duchenne muscular dystrophy." J Cardiol **53**(1): 72-78.
Olamaei, N., F. Cheriet, et al. (2010). "MRI visualization of a single 15 microm navigable imaging agent and future microrobot." Conference proceedings : ... Annual International Conference of the IEEE Engineering in Medicine and Biology Society. IEEE Engineering in Medicine and Biology Society. Conference **2010**: 4355-4358.
Palladino, M., I. Gatto, et al. (2013). "Angiogenic impairment of the vascular endothelium: a novel mechanism and potential therapeutic target in muscular dystrophy." Arterioscler Thromb Vasc Biol **33**(12): 2867-2876.
Papanikolaou, N., S. Karampekios, et al. (2006). "Fractional anisotropy and mean diffusivity measurements on normal human brain: comparison between low-and high-resolution diffusion tensor imaging sequences." European radiology **16**(1): 187-192.
Pauly, M., F. Daussin, et al. (2012). "AMPK activation stimulates autophagy and ameliorates muscular dystrophy in the mdx mouse diaphragm." Am J Pathol **181**(2): 583-592.
Petrof, B. J., J. B. Shrager, et al. (1993). "Dystrophin protects the sarcolemma from stresses developed during muscle contraction." Proceedings of the National Academy of Sciences of the United States of America **90**(8): 3710-3714.
Phillips, M. F. and R. Quinlivan (2008). "Calcium antagonists for Duchenne muscular dystrophy." Cochrane Database Syst Rev(4): CD004571.
Pierpaoli, C. and P. J. Basser (1996). "Toward a quantitative assessment of diffusion anisotropy." Magnetic resonance in medicine : official journal of the Society of Magnetic Resonance in Medicine / Society of Magnetic Resonance in Medicine **36**(6): 893-906.
Pollack, G. (1990). Muscles and Molecules - Uncovering the Principles of Biological Motion, Ebner and Sons Publishers.
Pope, A. J., G. B. Sands, et al. (2008). "Three-dimensional transmural organization of perimysial collagen in the heart." Am J Physiol Heart Circ Physiol **295**(3): H1243-H1252.
Pressmar, J., H. Brinkmeier, et al. (1994). "Intracellular Ca^{2+} concentrations are not elevated in resting cultured muscle from Duchenne (DMD) patients and in MDX mouse muscle fibres." Pflugers Arch **426**(6): 499-505.

Quinlan, J. G., H. S. Hahn, et al. (2004). "Evolution of the mdx mouse cardiomyopathy: physiological and morphological findings." Neuromuscul Disord **14**(8-9): 491-496.
Riley, D. A., J. L. Bain, et al. (2002). "Thin filament diversity and physiological properties of fast and slow fiber types in astronaut leg muscles." Journal of applied physiology **92**(2): 817-825.
Rinaldi, R., M. Mayer, et al. (2013). "Current Concepts in the Management of Duchenne Muscular Dystrophy." Current Physical Medicine and Rehabilitation Reports **1**(2): 65-71.
Roberts, T. P. and E. S. Schwartz (2007). "Principles and implementation of diffusion-weighted and diffusion tensor imaging." Pediatric radiology **37**(8): 739-748.
Robinson, L. A. and D. L. Harwood (1991). "Lowering the calcium concentration in St. Thomas' Hospital cardioplegic solution improves protection during hypothermic ischemia." J Thorac Cardiovasc Surg **101**(2): 314-325.
Romfh, A. and E. M. McNally (2010). "Cardiac assessment in duchenne and becker muscular dystrophies." Curr Heart Fail Rep **7**(4): 212-218.
Rybakova, I. N., J. R. Patel, et al. (2000). "The dystrophin complex forms a mechanically strong link between the sarcolemma and costameric actin." The Journal of cell biology **150**(5): 1209-1214.
Safford, R. E., E. A. Bassingthwaighte, et al. (1978). "Diffusion of water in cat ventricular myocardium." The Journal of general physiology **72**(4): 513-538.
Sahoo, S. K. and H. Kim do (2008). "Calumenin interacts with SERCA2 in rat cardiac sarcoplasmic reticulum." Mol Cells **26**(3): 265-269.
Sahoo, S. K., T. Kim, et al. (2009). "Characterization of calumenin-SERCA2 interaction in mouse cardiac sarcoplasmic reticulum." J Biol Chem **284**(45): 31109-31121.
Sakurai, K., N. Fujita, et al. (1992). "Magnetic susceptibility artifact in spin-echo MR imaging of the pituitary gland." AJNR. American journal of neuroradiology **13**(5): 1301-1308.
Sapp, J. L., J. Bobet, et al. (1996). "Contractile properties of myocardium are altered in dystrophin-deficient mdx mice." Journal of the neurological sciences **142**(1-2): 17-24.
Schmidt-Nielsen, K. (1984). Scaling, why is animal size so important? Cambridge ; New York, Cambridge University Press.
Schmidt, G. N., M. A. Burmeister, et al. (2003). "Acute heart failure during spinal surgery in a boy with Duchenne muscular dystrophy." British journal of anaesthesia **90**(6): 800-804.
Schram, G., A. Fournier, et al. (2013). "All-cause mortality and cardiovascular outcomes with prophylactic steroid therapy in Duchenne muscular dystrophy." J Am Coll Cardiol **61**(9): 948-954.
Scollan, D. F., A. Holmes, et al. (1998). "Histological validation of myocardial microstructure obtained from diffusion tensor magnetic resonance imaging." Am J Physiol **275**(6 Pt 2): H2308-2318.
Sethna, N. F., M. A. Rockoff, et al. (1988). "Anesthesia-related complications in children with Duchenne muscular dystrophy." Anesthesiology **68**(3): 462-465.
Shannon, T. R. (2009). "Ryanodine receptor Ca^{2+} sensitivity and excitation-contraction coupling in muscular dystrophy and heart failure: similar and yet different." Am J Physiol Heart Circ Physiol **297**(6): H1965-1966.
Shigemitsu, K., Y. Tsujishita, et al. (1999). "Regulation of translational effectors by amino acid and mammalian target of rapamycin signaling pathways. Possible involvement of autophagy in cultured hepatoma cells." J Biol Chem **274**(2): 1058-1065.
Shin, J. H., B. Bostick, et al. (2011). "SERCA2a gene transfer improves electrocardiographic performance in aged mdx mice." Journal of translational medicine **9**: 132.
Skrzypiec-Spring, M., B. Grotthus, et al. (2007). "Isolated heart perfusion according to Langendorff---still viable in the new millennium." Journal of pharmacological and toxicological methods **55**(2): 113-126.
Smith, S. M., T. McCoy, et al. (2012). "Space flight calcium: implications for astronaut health, spacecraft operations, and Earth." Nutrients **4**(12): 2047-2068.
Soman, N. R., S. L. Baldwin, et al. (2009). "Molecularly targeted nanocarriers deliver the cytolytic peptide melittin specifically to tumor cells in mice, reducing tumor growth." J Clin Invest **119**(9): 2830-2842.

Soman, N. R., G. M. Lanza, et al. (2008). "Synthesis and characterization of stable fluorocarbon nanostructures as drug delivery vehicles for cytolytic peptides." Nano Lett **8**(4): 1131-1136.
Sosnovik, D. E., R. Wang, et al. (2009). "Diffusion MR tractography of the heart." Journal of cardiovascular magnetic resonance : official journal of the Society for Cardiovascular Magnetic Resonance **11**: 47.
Spencer, M. J., D. E. Croall, et al. (1995). "Calpains are activated in necrotic fibers from mdx dystrophic mice." J Biol Chem **270**(18): 10909-10914.
Spencer, M. J. and J. G. Tidball (1996). "Calpain translocation during muscle fiber necrosis and regeneration in dystrophin-deficient mice." Exp Cell Res **226**(2): 264-272.
Spurney, C. F. (2011). "Cardiomyopathy of Duchenne muscular dystrophy: current understanding and future directions." Muscle & nerve **44**(1): 8-19.
Stejskal, E., Tanner, J. (1965). "Spin Diffusion Measurements: Spin Echoes in the Presence of a Time-Dependent Field Gradient." J. Chem. Phys. 42, 288 (1965).
Stepkowski, S. M. (2003). "Preclinical results of sirolimus treatment in transplant models." Transplant Proc **35**(3 Suppl): 219S-226S.
Stepkowski, S. M. (2003). "Preclinical results of sirolimus treatment in transplant models." Transplantation proceedings **35**(3 Suppl): 219S-226S.
Streeter, D. D., Jr. and W. T. Hanna (1973). "Engineering mechanics for successive states in canine left ventricular myocardium. II. Fiber angle and sarcomere length." Circ Res **33**(6): 656-664.
Stuckey, D. J., C. A. Carr, et al. (2012). "In vivo MRI characterization of progressive cardiac dysfunction in the mdx mouse model of muscular dystrophy." PLoS One **7**(1): e28569.
Tanaka, H. and E. Ozawa (1990). "Expression of dystrophin mRNA and the protein in the developing rat heart." Biochemical and biophysical research communications **172**(2): 824-829.
Taylor, A. J., N. Al-Saadi, et al. (2006). "Elective percutaneous coronary intervention immediately impairs resting microvascular perfusion assessed by cardiac magnetic resonance imaging." Am Heart J **151**(4): 891 e891-897.
Thomson, A. W., H. R. Turnquist, et al. (2009). "Immunoregulatory functions of mTOR inhibition." Nat Rev Immunol **9**(5): 324-337.
Thorpe, S. K., Y. Li, et al. (1998). "Stresses in human leg muscles in running and jumping determined by force plate analysis and from published magnetic resonance images." The Journal of experimental biology **201**(Pt 1): 63-70.
Townsend, D., M. J. Blankinship, et al. (2007). "Systemic administration of micro-dystrophin restores cardiac geometry and prevents dobutamine-induced cardiac pump failure." Mol Ther **15**(6): 1086-1092.
Townsend, D., S. Yasuda, et al. (2007). "Cardiomyopathy of Duchenne muscular dystrophy: pathogenesis and prospect of membrane sealants as a new therapeutic approach." Expert Rev Cardiovasc Ther **5**(1): 99-109.
Toyota, E., K. Fujimoto, et al. (2002). "Dynamic changes in three-dimensional architecture and vascular volume of transmural coronary microvasculature between diastolic- and systolic-arrested rat hearts." Circulation **105**(5): 621-626.
Tseng, W. Y., V. J. Wedeen, et al. (2003). "Diffusion tensor MRI of myocardial fibers and sheets: correspondence with visible cut-face texture." J Magn Reson Imaging **17**(1): 31-42.
van Deutekom, J. C., M. Bremmer-Bout, et al. (2001). "Antisense-induced exon skipping restores dystrophin expression in DMD patient derived muscle cells." Human molecular genetics **10**(15): 1547-1554.
van Deutekom, J. C., A. A. Janson, et al. (2007). "Local dystrophin restoration with antisense oligonucleotide PRO051." N Engl J Med **357**(26): 2677-2686.
Van Erp, C., N. G. Irwin, et al. (2006). "Long-term administration of pirfenidone improves cardiac function in mdx mice." Muscle & nerve **34**(3): 327-334.
Van Erp, C., D. Loch, et al. (2010). "Timeline of cardiac dystrophy in 3-18-month-old MDX mice." Muscle Nerve **42**(4): 504-513.

van Gelderen, P., M. H. de Vleeschouwer, et al. (1994). "Water diffusion and acute stroke." Magnetic resonance in medicine : official journal of the Society of Magnetic Resonance in Medicine / Society of Magnetic Resonance in Medicine **31**(2): 154-163.
Vassalle, M. and C. I. Lin (2004). "Calcium overload and cardiac function." J Biomed Sci **11**(5): 542-565.
Vidal, B., E. Ardite, et al. (2012). "Amelioration of Duchenne muscular dystrophy in mdx mice by elimination of matrix-associated fibrin-driven inflammation coupled to the alphaMbeta2 leukocyte integrin receptor." Hum Mol Genet **21**(9): 1989-2004.
Vilquin, J. T., I. Asselin, et al. (1995). "Successful myoblast allotransplantation in mdx mice using rapamycin." Transplantation **59**(3): 422-426.
Wagner, K. R., N. Lechtzin, et al. (2007). "Current treatment of adult Duchenne muscular dystrophy." Biochim Biophys Acta **1772**(2): 229-237.
Ward, C. W., M. F. Schneider, et al. (2000). "Expression of ryanodine receptor RyR3 produces Ca^{2+} sparks in dyspedic myotubes." J Physiol **525 Pt 1**: 91-103.
Ward, M. L., I. A. Williams, et al. (2008). "Stretch-activated channels in the heart: contributions to length-dependence and to cardiomyopathy." Prog Biophys Mol Biol **97**(2-3): 232-249.
Warren W. Burggren, B. B. K. (1997). Development of Cardiovascular Systems: Molecules to Organisms, Cambridge University Press.
Watts, J. A. and P. C. Maiorano (1999). "Trace amounts of albumin protect against ischemia and reperfusion injury in isolated rat hearts." Journal of molecular and cellular cardiology **31**(9): 1653-1662.
Webster, C., L. Silberstein, et al. (1988). "Fast muscle fibers are preferentially affected in Duchenne muscular dystrophy." Cell **52**(4): 503-513.
Wehrens, X. H., S. E. Lehnart, et al. (2004). "Protection from cardiac arrhythmia through ryanodine receptor-stabilizing protein calstabin2." Science **304**(5668): 292-296.
Whitehead, N. P., M. Streamer, et al. (2006). "Streptomycin reduces stretch-induced membrane permeability in muscles from mdx mice." Neuromuscul Disord **16**(12): 845-854.
Whitehead, N. P., E. W. Yeung, et al. (2010). "Skeletal muscle NADPH oxidase is increased and triggers stretch-induced damage in the mdx mouse." PLoS One **5**(12): e15354.
Wickline, S., A. Neubauer, et al. (2006). "Applications of nanotechnology to atherosclerosis, thrombosis, and vascular biology." Arteriosclerosis, Thrombosis & Vascular Biology **26**: 435-441.
Wickline, S. A., R. P. Mason, et al. (2010). Fluorocarbon agents for multimodal molecular imaging and targeted therapeutics. MOLECULAR IMAGING: PRINCIPLES AND PRACTICE R. Weissleder, B. D. Ross, A. Rehemtulla and S. S. Gambhir. Shelton, CT, Peoples Medical Publishing House-USA**:** 542-573.
Williams, I. A. and D. G. Allen (2007). "Intracellular calcium handling in ventricular myocytes from mdx mice." Am J Physiol Heart Circ Physiol **292**(2): H846-855.
Wullschleger, S., R. Loewith, et al. (2006). "TOR signaling in growth and metabolism." Cell **124**(3): 471-484.
Yang, X., L. Chin, et al. (2013). "Quantitative assessment of muscle damage in the mdx mouse model of Duchenne muscular dystrophy using polarization-sensitive optical coherence tomography." Journal of applied physiology.
Yasuda, S., D. Townsend, et al. (2005). "Dystrophic heart failure blocked by membrane sealant poloxamer." Nature **436**(7053): 1025-1029.
Yeung, E. W. and D. G. Allen (2004). "Stretch-activated channels in stretch-induced muscle damage: role in muscular dystrophy." Clin Exp Pharmacol Physiol **31**(8): 551-556.
Yilmaz, A., H. J. Gdynia, et al. (2008). "Cardiac involvement in patients with Becker muscular dystrophy: new diagnostic and pathophysiological insights by a CMR approach." Journal of cardiovascular magnetic resonance : official journal of the Society for Cardiovascular Magnetic Resonance **10**: 50.

Yilmaz, A., H. J. Gdynia, et al. (2010). "Images in cardiovascular medicine. Cardiomyopathy in a Duchenne muscular dystrophy carrier and her diseased son: similar pattern revealed by cardiovascular MRI." Circulation **121**(10): e237-239.
Zarse, M., C. Stellbrink, et al. (2001). "Verapamil prevents stretch-induced shortening of atrial effective refractory period in langendorff-perfused rabbit heart." Journal of cardiovascular electrophysiology **12**(1): 85-92.
Zatz, M. and R. T. Betti (1986). "Benign Duchenne muscular dystrophy in a patient with growth hormone deficiency: a five years follow-up." American journal of medical genetics **24**(3): 567-572.
Zatz, M., R. T. Betti, et al. (1986). "Treatment of Duchenne muscular dystrophy with growth hormone inhibitors." American journal of medical genetics **24**(3): 549-566.
Zatz, M., R. T. Betti, et al. (1981). "Benign Duchenne muscular dystrophy in a patient with growth hormone deficiency." American journal of medical genetics **10**(3): 301-304.
Zatz, M., D. Rapaport, et al. (1989). "Nocturnal rhythm of growth hormone in Duchenne patients: effect of different doses of mazindol and/or cyproheptadine." American journal of medical genetics **33**(4): 457-467.
Zatz, M., D. Rapaport, et al. (1988). "Effect of mazindol on growth hormone levels in patients with Duchenne muscular dystrophy." American journal of medical genetics **31**(4): 821-833.
Zhang, C., Y. J. Cheng, et al. (2012). "Label-free photoacoustic microscopy of myocardial sheet architecture." Journal of biomedical optics **17**(6): 060506.
Zhang, H., L. Zhang, et al. (2011). "Quantifying the evolution of vascular barrier disruption in advanced atherosclerosis with semipermeant nanoparticle contrast agents." PLoS One **6**(10): e26385.
Zhu, X., B. A. Altschafl, et al. (2005). "Altered Ca^{2+} sparks and gating properties of ryanodine receptors in aging cardiomyocytes." Cell Calcium **37**(6): 583-591.

Appendices

Principle of MRI

-Physics

In the view of classic physics, hydrogen nuclear spins, and thus creates magnetic moment, which aligns to surrounding magnetic field (B_0) in the same way compass points to the North Pole. [12] Instead of aligning statically with B_0, the magnetic moment would precess about the B_0 direction. The precession frequency, ω, is named Larmor Frequency and defined by $\omega = \gamma B$, where γ is gyromagetic ratio, depending on nuclear species. While nuclei spin reaches steady state of precession toward B_0, we can excite the steady state temporarily with an added magnetic field (B_1), causing the nuclear spin to deviate from its steady state orientation.[13] After the B_1 was stopped, nuclear spin will align back to the B_0 direction and release energy in a form of detectable radio frequency magnetic waves (called free induction decay, FID), which can be recorded and signal processed for imaging purposes.

-Imaging

Invented in 1952, MRI allows scientist to acquire FID and forms images to provide structural and functional information. Recall the Larmor Frequency, $\omega = \gamma B$, which is proportional to the magnetic field strength B, allowing us to control the ω by varying the B. For imaging purpose, we are interested in encode spin at different spatial locations with different ω. Therefore, a *gradient* of magnetic field, G_x, was applied along x direction on top of the B_0, making the ω a function of x, that is, $\omega(x)=B_0 + x \cdot G$, therefore, the recorded FID carries spatial information in different frequencies, allowing imaging reconstruction through inverse Fourier transform. This imaging technique is called frequency encoding. Please refer to book in footnote 11 for more information. By turning on-off radio frequency pulses and gradients at specific time and direction, we would be able to form images to suit specific purpose. The specific timing/direction/strength of radio frequency pulses and gradients are call **pulse sequence**, which determines the sources of contrast and properties of the images.

[12] The mechanism of nuclear spin is beyond scope, please refer to "Questions and Answers in Magnetic Resonance Imaging", 2000, by Allen D. Elster.

[13] For detailed physics explanation, see "Spin Dynamics: Basics of Nuclear Magnetic Resonance" by Malcolm H. Levitt (2008)

Supplemental tables

Table 2.Post Hoc Multiple Comparisons of |β| in 16 month old mice

Bonferroni

Dependent Variable	(I) group	(J) group	Mean Difference (I-J)	Std. Error	Sig.	95% Confidence Interval	
						Lower Bound	Upper Bound
magB_slc1	1	2	2.4033	2.01043	1.000	-3.6447	8.4514
		3	1.0321	2.01043	1.000	-5.0159	7.0802
		4	6.7905*	2.01043	.023	.7425	12.8386
	2	1	-2.4033	2.01043	1.000	-8.4514	3.6447
		3	-1.3712	2.01043	1.000	-7.4193	4.6768
		4	4.3872	2.01043	.266	-1.6608	10.4353
	3	1	-1.0321	2.01043	1.000	-7.0802	5.0159
		2	1.3712	2.01043	1.000	-4.6768	7.4193
		4	5.7584	2.01043	.067	-.2896	11.8065
	4	1	-6.7905*	2.01043	.023	-12.8386	-.7425
		2	-4.3872	2.01043	.266	-10.4353	1.6608
		3	-5.7584	2.01043	.067	-11.8065	.2896
magB_slc2	1	2	-.6827	2.36177	1.000	-7.7877	6.4223
		3	-1.3088	2.36177	1.000	-8.4138	5.7962
		4	4.9628	2.36177	.311	-2.1422	12.0677
	2	1	.6827	2.36177	1.000	-6.4223	7.7877
		3	-.6261	2.36177	1.000	-7.7311	6.4789
		4	5.6455	2.36177	.177	-1.4595	12.7504
	3	1	1.3088	2.36177	1.000	-5.7962	8.4138
		2	.6261	2.36177	1.000	-6.4789	7.7311
		4	6.2715	2.36177	.104	-.8334	13.3765
	4	1	-4.9628	2.36177	.311	-12.0677	2.1422
		2	-5.6455	2.36177	.177	-12.7504	1.4595
		3	-6.2715	2.36177	.104	-13.3765	.8334
magB_slc3	1	2	-.9798	2.26177	1.000	-7.7840	5.8244
		3	-.3786	2.26177	1.000	-7.1828	6.4255
		4	8.3630*	2.26177	.012	1.5588	15.1672
	2	1	.9798	2.26177	1.000	-5.8244	7.7840
		3	.6012	2.26177	1.000	-6.2030	7.4053
		4	9.3428*	2.26177	.005	2.5387	16.1470
	3	1	.3786	2.26177	1.000	-6.4255	7.1828

		2	-.6012	2.26177	1.000	-7.4053	6.2030
		4	8.7416*	2.26177	.008	1.9375	15.5458
	4	1	-8.3630*	2.26177	.012	-15.1672	-1.5588
		2	-9.3428*	2.26177	.005	-16.1470	-2.5387
		3	-8.7416*	2.26177	.008	-15.5458	-1.9375
magB_slc4	1	2	-1.3733	2.27890	1.000	-8.2290	5.4824
		3	-.3664	2.27890	1.000	-7.2221	6.4893
		4	5.1555	2.27890	.228	-1.7002	12.0112
	2	1	1.3733	2.27890	1.000	-5.4824	8.2290
		3	1.0069	2.27890	1.000	-5.8488	7.8626
		4	6.5288	2.27890	.067	-.3269	13.3845
	3	1	.3664	2.27890	1.000	-6.4893	7.2221
		2	-1.0069	2.27890	1.000	-7.8626	5.8488
		4	5.5219	2.27890	.166	-1.3338	12.3776
	4	1	-5.1555	2.27890	.228	-12.0112	1.7002
		2	-6.5288	2.27890	.067	-13.3845	.3269
		3	-5.5219	2.27890	.166	-12.3776	1.3338
magB_slc5	1	2	.4927	1.96992	1.000	-5.4334	6.4189
		3	.3064	1.96992	1.000	-5.6198	6.2325
		4	5.6741	1.96992	.065	-.2520	11.6003
	2	1	-.4927	1.96992	1.000	-6.4189	5.4334
		3	-.1863	1.96992	1.000	-6.1125	5.7398
		4	5.1814	1.96992	.109	-.7448	11.1076
	3	1	-.3064	1.96992	1.000	-6.2325	5.6198
		2	.1863	1.96992	1.000	-5.7398	6.1125
		4	5.3677	1.96992	.090	-.5584	11.2939
	4	1	-5.6741	1.96992	.065	-11.6003	.2520
		2	-5.1814	1.96992	.109	-11.1076	.7448
		3	-5.3677	1.96992	.090	-11.2939	.5584
magB_slc6	1	2	1.4707	2.06307	1.000	-4.7357	7.6771
		3	1.4960	2.06307	1.000	-4.7104	7.7025
		4	4.2457	2.06307	.338	-1.9607	10.4521
	2	1	-1.4707	2.06307	1.000	-7.6771	4.7357
		3	.0253	2.06307	1.000	-6.1811	6.2317
		4	2.7750	2.06307	1.000	-3.4314	8.9814
	3	1	-1.4960	2.06307	1.000	-7.7025	4.7104
		2	-.0253	2.06307	1.000	-6.2317	6.1811
		4	2.7497	2.06307	1.000	-3.4567	8.9561

	4	1	-4.2457	2.06307	.338	-10.4521	1.9607
		2	-2.7750	2.06307	1.000	-8.9814	3.4314
		3	-2.7497	2.06307	1.000	-8.9561	3.4567
magB_slc7	1	2	2.7587	3.21547	1.000	-6.9145	12.4319
		3	1.1879	3.21547	1.000	-8.4853	10.8611
		4	3.6151	3.21547	1.000	-6.0581	13.2883
	2	1	-2.7587	3.21547	1.000	-12.4319	6.9145
		3	-1.5708	3.21547	1.000	-11.2440	8.1024
		4	.8564	3.21547	1.000	-8.8168	10.5296
	3	1	-1.1879	3.21547	1.000	-10.8611	8.4853
		2	1.5708	3.21547	1.000	-8.1024	11.2440
		4	2.4272	3.21547	1.000	-7.2460	12.1004
	4	1	-3.6151	3.21547	1.000	-13.2883	6.0581
		2	-.8564	3.21547	1.000	-10.5296	8.8168
		3	-2.4272	3.21547	1.000	-12.1004	7.2460
magB_slc8	1	2	6.8267	5.77138	1.000	-10.5356	24.1889
		3	1.4031	5.77138	1.000	-15.9591	18.7654
		4	8.6303	5.77138	.926	-8.7320	25.9925
	2	1	-6.8267	5.77138	1.000	-24.1889	10.5356
		3	-5.4235	5.77138	1.000	-22.7858	11.9387
		4	1.8036	5.77138	1.000	-15.5586	19.1659
	3	1	-1.4031	5.77138	1.000	-18.7654	15.9591
		2	5.4235	5.77138	1.000	-11.9387	22.7858
		4	7.2271	5.77138	1.000	-10.1351	24.5894
	4	1	-8.6303	5.77138	.926	-25.9925	8.7320
		2	-1.8036	5.77138	1.000	-19.1659	15.5586
		3	-7.2271	5.77138	1.000	-24.5894	10.1351

Table 2. Post hoc multiple comparisons for diastolic |β| of 16 month old *mdx* and WT mice.

Group1,2,3, and 4 are WT-LC, WT-NC, *mdx*-LC, and *mdx*-NC respectively. MagB, |β|. Slc1 is base. Slc8 is apex. *, $p < 0.05$ level. Bonferroni correction. Most differences exist in the slc3 of group 4, indicating abnormal |β| manifest closer to base than apex.

Table 3. Post Hoc Multiple Comparisons of |β| in 3 month old mice

Bonferroni

Dependent Variable	(I) group	(J) group	Mean Difference (I-J)	Std. Error	Sig.	95% Confidence Interval	
						Lower Bound	Upper Bound
magB_slc1	1	2	-1.1000	2.97694	1.000	-10.0556	7.8556
		3	.3200	2.97694	1.000	-8.6356	9.2756
		4	2.4000	2.97694	1.000	-6.5556	11.3556
	2	1	1.1000	2.97694	1.000	-7.8556	10.0556
		3	1.4200	2.97694	1.000	-7.5356	10.3756
		4	3.5000	2.97694	1.000	-5.4556	12.4556
	3	1	-.3200	2.97694	1.000	-9.2756	8.6356
		2	-1.4200	2.97694	1.000	-10.3756	7.5356
		4	2.0800	2.97694	1.000	-6.8756	11.0356
	4	1	-2.4000	2.97694	1.000	-11.3556	6.5556
		2	-3.5000	2.97694	1.000	-12.4556	5.4556
		3	-2.0800	2.97694	1.000	-11.0356	6.8756
magB_slc2	1	2	-.6400	3.36391	1.000	-10.7598	9.4798
		3	2.0400	3.36391	1.000	-8.0798	12.1598
		4	3.7400	3.36391	1.000	-6.3798	13.8598
	2	1	.6400	3.36391	1.000	-9.4798	10.7598
		3	2.6800	3.36391	1.000	-7.4398	12.7998
		4	4.3800	3.36391	1.000	-5.7398	14.4998
	3	1	-2.0400	3.36391	1.000	-12.1598	8.0798
		2	-2.6800	3.36391	1.000	-12.7998	7.4398
		4	1.7000	3.36391	1.000	-8.4198	11.8198
	4	1	-3.7400	3.36391	1.000	-13.8598	6.3798
		2	-4.3800	3.36391	1.000	-14.4998	5.7398
		3	-1.7000	3.36391	1.000	-11.8198	8.4198
magB_slc3	1	2	.0600	3.60697	1.000	-10.7910	10.9110
		3	2.1800	3.60697	1.000	-8.6710	13.0310
		4	6.1800	3.60697	.636	-4.6710	17.0310
	2	1	-.0600	3.60697	1.000	-10.9110	10.7910
		3	2.1200	3.60697	1.000	-8.7310	12.9710
		4	6.1200	3.60697	.655	-4.7310	16.9710
	3	1	-2.1800	3.60697	1.000	-13.0310	8.6710
		2	-2.1200	3.60697	1.000	-12.9710	8.7310

		4	4.0000	3.60697	1.000	-6.8510	14.8510
	4	1	-6.1800	3.60697	.636	-17.0310	4.6710
		2	-6.1200	3.60697	.655	-16.9710	4.7310
		3	-4.0000	3.60697	1.000	-14.8510	6.8510
magB_slc4	1	2	.1200	3.07448	1.000	-9.1290	9.3690
		3	4.0600	3.07448	1.000	-5.1890	13.3090
		4	7.4600	3.07448	.165	-1.7890	16.7090
	2	1	-.1200	3.07448	1.000	-9.3690	9.1290
		3	3.9400	3.07448	1.000	-5.3090	13.1890
		4	7.3400	3.07448	.178	-1.9090	16.5890
	3	1	-4.0600	3.07448	1.000	-13.3090	5.1890
		2	-3.9400	3.07448	1.000	-13.1890	5.3090
		4	3.4000	3.07448	1.000	-5.8490	12.6490
	4	1	-7.4600	3.07448	.165	-16.7090	1.7890
		2	-7.3400	3.07448	.178	-16.5890	1.9090
		3	-3.4000	3.07448	1.000	-12.6490	5.8490
magB_slc5	1	2	-1.0200	3.33267	1.000	-11.0458	9.0058
		3	2.5000	3.33267	1.000	-7.5258	12.5258
		4	5.6200	3.33267	.667	-4.4058	15.6458
	2	1	1.0200	3.33267	1.000	-9.0058	11.0458
		3	3.5200	3.33267	1.000	-6.5058	13.5458
		4	6.6400	3.33267	.382	-3.3858	16.6658
	3	1	-2.5000	3.33267	1.000	-12.5258	7.5258
		2	-3.5200	3.33267	1.000	-13.5458	6.5058
		4	3.1200	3.33267	1.000	-6.9058	13.1458
	4	1	-5.6200	3.33267	.667	-15.6458	4.4058
		2	-6.6400	3.33267	.382	-16.6658	3.3858
		3	-3.1200	3.33267	1.000	-13.1458	6.9058
magB_slc6	1	2	-.3800	3.73493	1.000	-11.6159	10.8559
		3	2.8400	3.73493	1.000	-8.3959	14.0759
		4	4.8800	3.73493	1.000	-6.3559	16.1159
	2	1	.3800	3.73493	1.000	-10.8559	11.6159
		3	3.2200	3.73493	1.000	-8.0159	14.4559
		4	5.2600	3.73493	1.000	-5.9759	16.4959
	3	1	-2.8400	3.73493	1.000	-14.0759	8.3959
		2	-3.2200	3.73493	1.000	-14.4559	8.0159
		4	2.0400	3.73493	1.000	-9.1959	13.2759
	4	1	-4.8800	3.73493	1.000	-16.1159	6.3559

		2	-5.2600	3.73493	1.000	-16.4959	5.9759
		3	-2.0400	3.73493	1.000	-13.2759	9.1959
magB_slc7	1	2	-.2000	3.96679	1.000	-12.1334	11.7334
		3	1.8000	3.96679	1.000	-10.1334	13.7334
		4	.6800	3.96679	1.000	-11.2534	12.6134
	2	1	.2000	3.96679	1.000	-11.7334	12.1334
		3	2.0000	3.96679	1.000	-9.9334	13.9334
		4	.8800	3.96679	1.000	-11.0534	12.8134
	3	1	-1.8000	3.96679	1.000	-13.7334	10.1334
		2	-2.0000	3.96679	1.000	-13.9334	9.9334
		4	-1.1200	3.96679	1.000	-13.0534	10.8134
	4	1	-.6800	3.96679	1.000	-12.6134	11.2534
		2	-.8800	3.96679	1.000	-12.8134	11.0534
		3	1.1200	3.96679	1.000	-10.8134	13.0534

Table 3 Post hoc multiple comparisons for diastolic |β| of 3 month old *mdx* and WT mice showing no significance.

Group1,2,3, and 4 are WT-LC, WT-NC, *mdx*-LC, and *mdx*-NC respectively. MagB, |β|. Slc1 is base. Slc7 is apex. No significance was found among all comparison.

Speculation: Might low gravity ameliorate dystrophy?

In the Chapter 4, we raised the point that higher stress within certain muscles might explain the regional heterogeneity of dystrophy (e.g., severe at heart base but not apex; severe in calf but not forearm). If genetic therapy could not break limitations on gene size and achieve stable transfection, relocating DMD patients to low gravity environments might reduce muscle stress and ameliorate the dystrophy. Furthermore, low gravity affects normal human health due to the redistribution of circulation pressure and decrease muscle/skeleton tension (Smith, McCoy *et al*. 2012). Lower limb muscles atrophy was observed among astronauts to the greatest extent, with the *calf muscles being most affected* and most difficult to target with exercise countermeasures (Lester, Standley *et al*. 2013). Similarly, the most obvious pathological sign of

DMD patients is the pseudo-hypertrophic *calf muscle*, indicating the calf muscle are sensitive to stress, both in space and on the Earth. In fact, DMD patients on the Earth and astronauts in orbits show complimentary loss of muscle fiber types. Specifically, DMD patients lose fast fibers rather than slow fibers (Webster, Silberstein *et al*. 1988), while astronauts lose slow fibers rather than fast fiber (Riley, Bain et al. 2002). I hypothesize that dystrophin is part of stress sensing pathway and signals to reduce astronauts' slow fibers in response to the lower load. When dystrophin is missing, the presumed stress sensing pathway might over-react to the normal stress on the earth and signal to reduce fast fibers in DMD. Since it is unknown how exactly low-gravity changes circulation/muscle/skeleton [14], how dystrophin-null animals adapt low-gravity environment may shed lights on such mechanism and bring better solutions to counter atrophy in space missions. The hypothetical mechanical sensing and protective mechanism of dystrophin would be critical for extraplanetary exploration, when we would need to fine-tune human body to adapt different gravities.

Sources of funding:

American Heart Association 12PRE9310044 (Cheng), R01 AR056223 (Wickline)

[14] "*The exact cellular and biochemical events that produce these losses of mass and strength are not as well understood." NASA 2013. Effect of Prolonged Space Flight on Human Skeletal Muscle (Biopsy)*

C.V. of Ya-Jian Cheng

email: ycgggg@gmail.com

+EDUCATION

Washington University in St. Louis, MO, USA **August 2007-May 2014**
Ph.D. in Biomedical Engineering, GPA 3.86/4.00

National Taiwan University, Taipei, Taiwan **July 2005-June 2007**
M.S. in Electric Engineering, GPA 4.00/4.00

National Taiwan University, Taipei, Taiwan **July 2001-June 2005**
B.S. in Life Science, GPA 3.70/4.00, Valedictorian

+HONORS

- 2013 American Heart Association BCVS Travel Grant
- 2012 American Heart Association Predoctoral Fellowship
- 2012 Washington University Merit Fund of Engineering School
- 2012 Biomedical Engineering Society Design and Research Award
- 2012 Biomedical Engineering Society Travel Award
- 2012 2nd place award in Graduate Research Symposium of Washington University
- 2011 2nd place award in North America Taiwanese Engineering Association Symposium
- 2007 Taiwan Merit Scholar, National Science Council, Taiwan, ROC
- 2006 Outstanding Achievement Award of National Taiwan University Scholarship
- 2006 Award of Taiwan Competition on Biomedical Engineering Creative Design
- 2005 Valedictorian of Class 2005 of Life Science Department, NTU, Taiwan
- 2003 Scholarship for Outstanding Students' Education
- 2001 Silver Medal, International Biology Olympiad, Belgium
- 2001 Presidential Award of National Taiwan University

+RESEARCH

Washington University School of Medicine, St. Louis, MO **2007-2014**
Graduate Research Assistant

- Acquire myocardial structure of viable mouse hearts with ultra-high field 11.7 tesla MRI, resulting in a $52,000 American Heart Association predoctoral fellowship and a $5,000 merit fund from Washington University
- Designed an *ex vivo* Langendorff mouse heart perfusion system for MRI, resulting in 2012 Design and Research Award of the Biomedical Engineering Society

- Proved dystrophic mice heart is abnormal dominantly at heart base rather than apex, despite mutation is every cell, indicating local heterogeneity modifies cardiac myopathy
- Implement automatic imaging segmentation, signal processing and statistical analysis of ultrasound, MRI, and optic images of heart muscle
- Developed theory of higher stress deteriorates heart muscle regionally at heart base
- Led collaboration among four labs for anti-aging treatments involving drug-loaded nanoparticles

National Taiwan University, Taipei, Taiwan **July 2005–June 2007**

Graduate Research Assistant

- Designed a microbubble and ultrasound sonification/quantification scheme, resulting in 2006 2nd Place Award in Biomedical Engineering Creative Design Competition in Taiwan
- Quantitative analysis for ultrasound spectrum with MATLAB

Academia Sinica, Institute of Biomedical Science **July-August 2004**
Taipei, Taiwan

Undergraduate Research Assistant

- Construct DNA clone of cancer proteases
- Imaged euryhaline fish's gill with scanning electron microscope for salt modulation study

+RESEARCH INTRESTS

- Imaging / signal processing
- Compressed sensing in MRI
- Heart muscle form & function
- Diastolic suction mechanism
- Boneless muscle mechanics
- Coronary vasculature

+PRESENTATIONS

- Oral in American Heart Association, Dallas, TX November 2013
- Poster in ISMRM, Salt Lake City, UT April 2013
- Poster in FASEB, Boston, MA April 2013
- Poster in American Heart Association, Los Angeles, CA November 2012
- Oral in Biomedical Engineering Society, Atlanta, GA October 2012
- Poster in Washington University Graduate Research Symposium, MO April 2012
- Oral in Society for Cardiovascular Magnetic Resonance, Orlando, FL February 2012
- Poster in American Heart Association, Orlando, FL November 2011
- Oral in North America Taiwanese Engineering Association Symposium April 2011
- Oral in Acoustical Society of America, San Antonio, TX October 2009
- Oral in IEEE International Ultrasonics Symposium, Rome, Italy September 2009

+SKILLS

- High field diffusion tensor MRI
- Signal & imaging processing in MATLAB
- FFT Spectrum analysis
- Image segmentation
- Small animal surgery
- Langendorff perfused mouse heart
- Anatomy / Histology
- Biomedical Engineering
- ImageJ / Photoshop
- SPSS / Linux / LibreOffice
- SSH
- Fluent in English, Native in Taiwanese, Native in Chinese

+LEADERSHIP

Washington University Biomedical Engineering Society 2012
President

Washington University Taiwanese Graduate Student Association 2011
Vice President

+MEMBERSHIPS

Biomedical Engineering Society	2008, 2012
American Heart Association	2010-13
National Society of Professional Engineer	2011
American Association of Anatomists	2012

+PEER-REVIEWED PUBLICATIONS

- Kristin P. Bibee, **Ya-Jian Cheng**, et al. (2014). Rapamycin nanoparticles target defective autophagy in muscular dystrophy to enhance both strength and cardiac function. Federation of American Societies for Experimental Biology, accepted.
- **Cheng, Y. J.**, D. Lang, et al. (2012). Focal but reversible diastolic sheet dysfunction reflects regional calcium mishandling in dystrophic mdx mouse hearts. American journal of physiology. Heart and circulatory physiology 303(5): H559-568
- Zhang, C., **Cheng Y. J.**, et al. (2012). Label-free photoacoustic microscopy of myocardial sheet architecture." Journal of biomedical optics 17(6): 060506..
- **Ya-Jian Cheng**, et al. (2012). Focal But Reversible Diagnostic Myocardial Architecture Abnormalities Reflect Regional Calcium Mishandling in Dystrophic mdx Mouse Hearts as Defined by diffusion Tensor. 2012 Biomedical Engineering Society Conference.
- Chi Zhang, **Ya-Jian Cheng**, Da-Kang Yao, Samuel Wickline, Lihong V. Wang, (2012) Photoacoustic microscopy of myocardial sheet architecture in unfixed and unstained mammalian hearts, Society of Photographic Instrumentation Engineers BiOS conference
- **Ya-Jian Cheng,** et al. (2011) Calcium-Dependent Changes in Myocardial Sheet Mechanics Reveal Reversible Diastolic Dysfunction in Aged Duchenne Muscular Dystrophy (mdx) Mice. 2011 American Heart Association Scientific Sessions
- **Cheng Y-J**, Hughes MS, Marsh JN, Wallace KD, Wickline SA. (2009) Shannon entropy can detect myocardial anisotropy without specular echo gating in vitro. The Journal of the Acoustical Society of America. 2009;126:2214
- **Cheng YJ**, Marsh JN, Wallace KD, Zhang L, Lanza GM, Wickline SA, Hughes MS. (2009) Shannon entropy: A specular echo-insensitive imaging metric showing myocardial anisotropy. Ultrasonics Symposium (IUS), 2009 IEEE International. 2009:373-376
- Bai MY, **Cheng YJ**, Wickline SA, Xia Y. (2009) Colloidal hollow spheres of conducting polymers with smooth surface and uniform, controllable sizes. Small. 2009;5:1747-1752
- Hu KH, Lee FP, **Cheng YJ**, Huang HM. (2009) Vascular endothelial growth factor and children featuring nasal polyps. Int J Pediatr Otorhinolaryngol. 2007;71:23-28
- Hu KH, Tan CT, Lin KN, Cheng YJ, Huang HM. (2008) Effect of endoscopic sinus surgery on irradiation-induced rhinosinusitis in patients with nasopharyngeal carcinoma. Otolaryngol Head Neck Surg. 2008;139:575-579
- Huang HM, **Cheng YJ**, Liu CM, Lin KN. (2006) Mucosal healing and mucociliary transport change after endoscopic sinus surgery in children with chronic maxillary sinusitis. Int J Pediatr Otorhinolaryngol. 2006;70:1361-1367